The Pennsylvania State University
The Graduate School

THREE DIMENSIONAL FINITE DIFFERENCE TIME DOMAIN MODELING OF SCHUMANN RESONANCES ON EARTH AND OTHER PLANETS OF THE SOLAR SYSTEM

A Thesis in
Electrical Engineering
by
Heng Yang

Submitted in Partial Fulfillment
of the Requirements
for the Degree of

Doctor of Philosophy

December 2007

The thesis of Heng Yang was reviewed and approved* by the following:

Victor P. Pasko
Associate Professor of Electrical Engineering
Thesis Advisor, Chair of Committee

Kultegin Aydin
Professor of Electrical Engineering

Michael Lanagan
Associate Professor of Engineering Science and Mechanics

John D. Mathews
Professor of Electrical Engineering

Douglas Werner
Professor of Electrical Engineering

W. Kenneth Jenkins
Professor of Electrical Engineering
Head of the Department of Electrical Engineering

*Signatures are on file in the Graduate School.

Abstract

Resonance properties of the Earth-ionosphere cavity were predicted by W. O. Schumann in 1952. Since then observations of electromagnetic signals in the frequency range 1-500 Hz have become a powerful tool for variety of remote sensing applications, which in recent years included studies of thunderstorm related transient luminous events in the middle atmosphere and related lightning discharges. In this thesis, a three dimensional Finite Difference Time Domain (FDTD) model is developed to study the propagation of the extremely low frequency (ELF) waves in the Earth-ionosphere cavity and in similar cavities on other celestial bodies of the Solar System.

A comparison of the results from this FDTD model with a set of classical eigenfrequency (f_n) and quality factor (Q_n) solutions for laterally uniform spherically symmetric Earth-ionosphere cavity and with recent observations of Schumann resonance (SR) during solar proton events (SPEs) and X-ray bursts is provided. The FDTD f_n and Q_n solutions for the uniform cavity appear to be in excellent agreement (within several %) with well-known experimental results documented in the literature. The related analysis indicates that the frequency of the first SR mode decreases during SPEs and increases during X-ray bursts by a fraction of a Hz, in agreement with physical arguments presented in previously published literature and with observations. The FDTD model is extended to include the effects of the geomagnetic field on SR parameters. A higher penetration height of SR electric and magnetic components is found with the presence of the geomagnetic field.

In a realistic cavity, the conductivity distribution is not laterally uniform and spherically symmetric, but varies with local time and seasons reflecting related variations in the effects of solar radiation on the conductivity of the lower ionosphere. The global lightning activity in the three main areas (Africa, South-East Asia, and South America) also has diurnal and seasonal variation patterns, which manifest themselves in the diurnal and seasonal variations of SR parameters. In

this thesis, the FDTD model is used to account for the realistic cavity at different local time and seasons using asymmetric conductivity profiles derived from International Reference Ionosphere (IRI) model. The FDTD results are compared with observational data in the available literature. The influence of the diurnal and seasonal conductivity variation, the global lightning activity, and the positions of the observation stations on the SR parameters are discussed. Another important factor influencing the SR power is related to the shifts of the global thunderstorm regions due to the El Niño and La Niña phenomena. Due to the different spatial field distributions of SR electric and magnetic components in the Earth-ionosphere cavity, the different power variation patterns are clearly observed in the electric and magnetic components with the motion of the thunderstorm center in our FDTD results. A new method is proposed to detect the shifts of the thunderstorm regions related to the El Niño and La Niña phenomena using a combination of electric and magnetic components of Schumann resonances at a single station.

In recent years, there has been an increasing interest in the exploration of the other planets in the Solar System. On January 14, 2005, HUYGENS probe landed on Titan, and started exploration of this largest moon of Saturn. One of multiple missions of HUYGENS probe is to find if there are lightning discharges in the Titans atmosphere. It is believed that conducting properties of the Titans atmosphere are favorable for the formation of the cavity for propagation of electromagnetic waves, so the existence of SR will give a support for the existence of the electrical discharges in the lower atmosphere on Titan. SR parameters are also useful in the study of the electromagnetic properties of Titans lower ionosphere. Several papers have recently been published in the refereed literature, which discuss SR parameters on Titan. In this thesis, the 3D FDTD model is used to predict the SR frequencies and Q-factors on Titan. The FDTD results are also compared with those obtained by other analytical and numerical techniques reported in the previously published papers. Besides Titan, we also discuss SR on other planets, specifically Mars and Venus. The atmospheric conductivity profiles for these studies are derived from the previously reported ionospheric models for these planets.

Table of Contents

List of Figures

List of Tables

Acknowledgments

First and foremost, I would like to thank my advisor, Dr. Victor Pasko, for the guidance and support that he provide over the past five years. Without his insightful direction and continual encouragement, the research results presented in this dissertation would not have been possible. I owe a great debt of gratitude for his patience, inspiration and enthusiasm.

I would also like to express my gratitude to Professors Kultegin Aydin, Michael Lanagan, John Mathews, and Douglas Werner for serving on the committee for my Ph.D defense, as well as their instruction and continual friendly support during my studies at Penn State. I would like to thank Dr. Gabriella Satori, Dr. Earle Williams, and Dr. Ningyu Liu for fruitful discussions related to my research in this dissertation.

I am indebted to my friends, especially Michael Pellen, Joshua Petko, Brian Rybicki, Jeremy Riousset and Jonathan Snively, for their patience and support. I am also indebted to the many individuals in the department who have made my study in Penn State a memorable one.

Finally, I would like to thank my parents, Hongying Heng and Benke Yang, my fiancee, Yun Zhang, as well as my little sister, Li Yang, for the endless encouragement and support they have offered through the years. I could not have completed this thesis without it.

Heng Yang
University Park, PA
October 9, 2007

This research was supported by the National Science Foundation under grant ATM-0134838 to the Pennsylvania State University.

Dedication

to my mother and father,

Hongying Heng *and* Benke Yang

to

Yun

Chapter 1

Introduction

1.1 Earth-Ionosphere Cavity and Schumann Resonances

Earth is a solid sphere covered by oceans (71%) and terrestrial land (29%). The conductivity of seawater is approximately 4 S/m, and the conductivity of the soil ranges from 10^{-4} to 10^{-2} S/m [e.g., *Balanis*, 1989, pp. 62]. For electromagnetic waves in Extremely Low Frequency band (ELF: 3-3000 Hz), this terrestrial boundary has high enough conductivity to be a good conductor to reflect ELF electromagnetic waves. Near the ground, the atmospheric conductivity is a scalar quantity with a value of approximately 10^{-14} S/m, making the atmosphere in this region a very good insulator. A substantial increase in the atmospheric conductivity is found starting from a few tens of kilometers to the higher altitude with a characteristic scale 3 to 6 km due to the solar radiation. Above 90 km, the ratio of the electron gyrofrequency to the electron-neutral collision frequency is no longer negligible, and the conductivity becomes a tensor quantity. The atmospheric conductivity parallel to the magnetic field in this region is in the range of

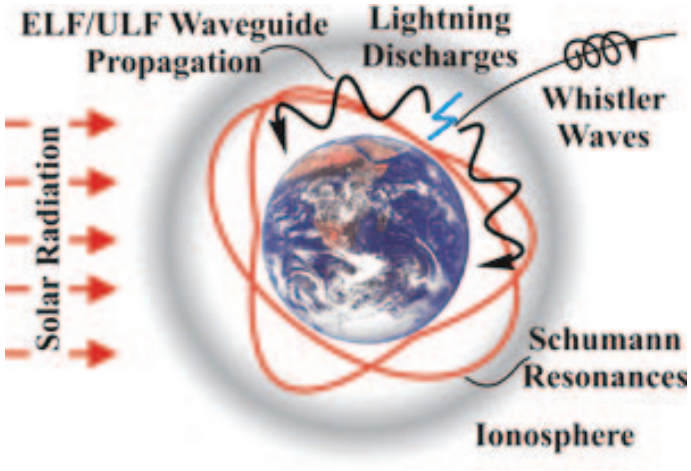

Figure 1.1. The geometry of the Earth-ionosphere cavity (The figure is taken from http://www.iihr.uiowa.edu/projects/schumann/Index.html).

10^{-4} to 10^{-2} S/m [*Sentman*, 1995, pp. 268], comparable to that of the terrestrial land surface. The combination of the highly conducting terrestrial surface boundary and the conducting ionospheric outer boundary separated by an insulating air layer creates a spherically concentric cavity, Earth-ionosphere cavity, supporting the propagation of the electromagnetic waves as shown schematically in Figure 1.1.

Lightning discharges radiate a broadband electromagnetic wave into the Earth-ionosphere cavity. Due to the conducting loss in the atmosphere, only the lowest frequency components can travel around the Earth several times without suffering serious attenuation. The phase addition and cancellation of waves along multiple paths produce a resonant line spectrum, which may be described in term of quasi-transverse electromagnetic normal modes of the Earth-ionosphere cavity. The total resonant spectrum is the incoherent superposition of the effects from the global lightning activity [*Sentman*, 1995, pp. 268].

The first mention of electromagnetic oscillations in a cavity between concentric spheres can be found in the book on electricity and magnetism by Joseph J. Thomson published in 1893 [*Thomson*, 1893]. Although Nikola Tesla was thought as the

first person who tried to consider the Earth as a radio device and planned to excite electrical oscillations over the whole planet, the existing literature, unfortunately, gives no citation to a relevant Tesla publication on this subject [*Besser*, 2007]. Tracing a paper published by *Chapman and Jones* [1964], we learn that the Irish physicist George F. FitzGerald presented a talk related to electromagnetic resonances between the ground and conducting atmosphere in 1893 during the 63rd Meeting of the British Association of the Advancement of Science in Nottingham, United Kingdom [*FitzGerald*, 1893a, b], and it seems that FitzGerald was really the first to consider the so-called Schumann resonance problem in the frame of the then only vaguely suspected Earth-ionosphere concept [*Besser*, 2007]. Between 1952 and 1957, German Scientist Winfried Otto Schumann published about 20 scientific papers on physics of electrical oscillations in the Earth-ionosphere cavity. Since he was the first to predict and discuss the resonance properties of the Earth-ionosphere cavity, these resonances are also referred to as Schumann Resonances (SR). The earliest experimental detection of SR was made by *Schumann and König* [1954] and *König* [1959]. In those experiments, the measured frequency is in the range of 8-9 Hz, and the intensity of the lowest mode is found exhibiting diurnal variations. However, the spectral representations for the frequency range under study was not derived because of the lack of a spectral analyzer [*König*, 1959]. The first spectral representation showing the existence of SR was presented by [*Balser and Wagner*, 1960] in the frequency range from 5 to 34 Hz with a clear show of the first five SR modes. More detailed information about the historic developments of Schumann resonances can be found in [*Besser*, 2007].

Only one year after Thomson and FitzGerald investigated the aforementioned problems, Joseph Larmor calculated the resonance frequencies of a uniform spherical condenser in 1894 [*Larmor*, 1893] assuming the separation distance between

two spheres is much smaller than the radius of the inner sphere. These results are exactly the same as what was derived by *Schumann* [1952] (shown in equation (1.1)). In an ideal Earth-ionosphere cavity, in which the terrestrial surface and ionosphere are all perfectly conducting, and the space between these two boundaries is insulating, the resonant frequencies are:

$$f_n = \frac{c}{2\pi R_e}\sqrt{n(n+1)} \tag{1.1}$$

where c is the speed of light, R_e is the radius of the Earth (approximately equal to 6370 km), and n is the order of the resonance modes. By equation (1.1), the first five SR frequencies in this ideal cavity are 10.5, 18.2, 25.8, 33.3, and 40.8 Hz. The equation (1.1) is only correct when the cavity height is much smaller than the inner radius of the cavity. In the Earth-ionosphere cavity, the height of the cavity (h) is around 100 km, and the radius of the Earth is 6370 km, which satisfied the condition of $h \ll R_e$. However, for the cavity whose height is comparable with the planet's radius, e.g., Titan, the effect of the height of the cavity cannot be ignored. The equation (1.1) need to be revised to account for related correction [*Schumann*, 1952]:

$$f_n = \frac{c}{2\pi R_e}\sqrt{n(n+1)\left(1-\frac{h}{R_e}\right)} \tag{1.2}$$

In the realistic cavity, the SR frequencies are found to be less than those in the ideal cavity due to the energy dissipation associate with finite atmospheric conductivity in the cavity. Figure 1.2 shows an example of the realistic measurement of SR spectrum [*Price and Melnikov*, 2004]. The first four SR frequencies are clearly observed at approximately 7.8, 14, 20, and 26 Hz, respectively.

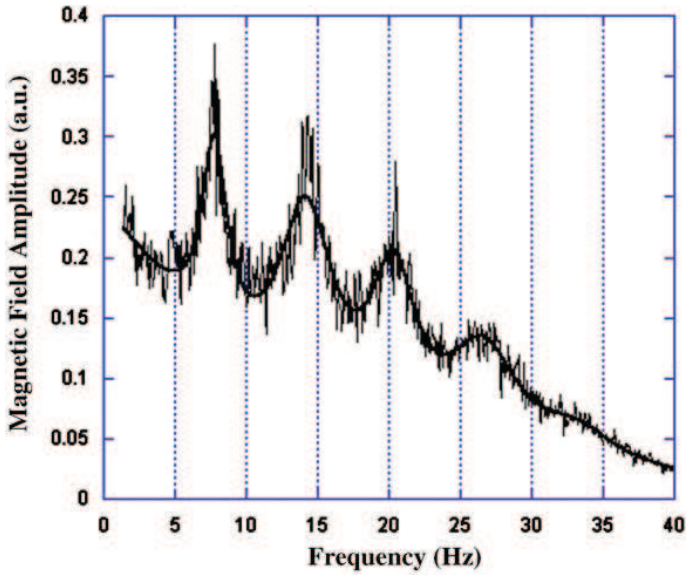

Figure 1.2. An example of the spectra of the magnetic field in north-south direction showing the first four Schumann resonance modes (figure courtesy of [*Price and Melnikov*, 2004]).

1.2 Variations in Schumann Resonance Parameters

Long-term measurements demonstrate that SR parameters (power, frequency and Q-factor) exhibit well established diurnal and seasonal variations. There have been a number of studies investigating the diurnal and seasonal variability of the SR parameters [e.g., *Balser and Wagner*, 1962; *Sentman and Fraser*, 1991; *Sátori et al.*, 1996; *Sátori*, 1996; *Price and Melnikov*, 2004; *Yang and Pasko*, 2006; *Ondrášková et al.*, 2007].

The simultaneous measurements of the horizontal magnetic component of Schumann resonance intensities in California and Australia during two separate intervals of September 2-17, 1989 and April 14-21, 1990 were made by *Sentman and Fraser* [1991]. The results show an obvious diurnal modulation in SR power related to local ionospheric height. The SR intensity is clearly found becoming stronger at

day time due to the descent of the ionosphere. The sharp amplitude increase always precedes the local surface sunrise and follows the local surface sunset by about 15-20 minutes in the sunrise/sunset intervals of about 45 minutes. The duration of the sharp, frequency-dependent amplitude variations is less than 30 minutes. The relative SR amplitude variations at ionospheric sunrise/sunset depend on the frequency and increase with increasing mode number from approximately 12% to 25% for the first three SR modes (8 Hz, 14 Hz, 20 Hz) [*Sátori et al.*, 2007].

Price and Melnikov [2004] reported the diurnal and seasonal variations of SR power, frequency and Q-factor based on a four-year measurement (1999-2003). Due to the location of the observation station with respect to the three main thunderstorm regions in the Earth-ionosphere cavity, SR fields (E_r, H_{NS}, and H_{EW}) undergo different power variation patterns. For E_r and H_{EW} components, a dominant power maxima has been found in the diurnal cycle corresponding to lightning activity in Africa around 1400 UT, two other power maxima have been observed in the H_{NS} component related to the lightning activity in South-East Asia and South America at 0800 UT and 2200 UT, respectively. Furthermore, the diurnal SR power variation caused by the variability of lightning activity is over 40%, which is much greater than that related to the ionospheric height. Therefore, it has been concluded that SR power variations is governed primarily by the variations in the global lightning activity and the source-receiver geometry, and the effect of the day-night asymmetry in the ionosphere is secondary [*Yang and Pasko*, 2006; *Pechony and Price*, 2007].

Besides the diurnal conductivity variations with the solar radiation, the SR parameters are also sensitive to some external perturbations. During the Solar Proton Events (SPE), high-energy particle precipitation is often accompanied by X-ray bursts leading to significant perturbation of the conductivity in the cavity

[*Sentman*, 1983]. Different shifts of the SR parameters were reported in many realistic measurements. The frequency changes of the first SR mode were studied by *Schlegel and Fullekrug* [1999] for 9 SPEs. They found that the long-term averaged frequency was equal to 7.8 Hz and increases by 0.04-0.14 Hz during SPEs. However, *Roldugin et al.* [2001] observed not an increase but a decrease of the first SR frequency during SPEs (about -0.4 Hz). *Roldugin et al.* [2004] also reported that the first SR frequency increases by 0.5 Hz during the X-ray bursts. *Yang and Pasko* [2005] discussed that the variation patterns of the first SR frequency associated with the ionospheric conductivity perturbation during these two events. It was concluded that the SR frequency variation with these the external perturbations depends on the altitude where the conductivity perturbation is situated. The conductivity perturbation at high altitude (>70 km) leads to increase in the first SR frequency; whereas, the first SR frequency decreases with conductivity perturbation at low altitude (<70 km) [*Sentman*, 1983; *Yang and Pasko*, 2005].

1.3 Motivation for Studies of Schumann Resonances

In recent years, there has been an increasing interest in studies of Schumann resonances. Due to their sensitivity to electromagnetic properties of lower ionosphere, SR can be employed as an indicator of the electromagnetic properties of the Earth-ionosphere cavity. Some inverse problems have been solved to extract the electromagnetic properties of the lower ionosphere from SR spectra [*Cummer*, 2000]. Moreover, the significant ionospheric perturbations associated with SPEs and X-ray bursts can be detected using the variations in SR parameters [e.g., *Sent-*

man, 1983; *Schlegel and Fullekrug*, 1999; *Roldugin et al.*, 2001, 2003, 2004; *Yang and Pasko*, 2005]. SR can also be utilized as a sensitive tool for the remote sensing of the global lightning activity. A one-site technique has been developed by *Shvets* [2001] to reveal the total worldwide lightning intensity and its distance distribution based on the decomposition of the average background SR spectra. In this thesis, we also present a new method to detect the shifts of the main thunderstorm regions related to El Niño and La Niña phenomena by measuring SR intensity variations at a single station. Also, in this thesis an inverse method based on genetic algorithms (GA) is developed to extract global lightning activity in three regions (Africa, South-East Asia, and South America) from the realistic SR measurements presented in [*Price and Melnikov*, 2004].

Sprites are large scale electrical discharges occurring at mesospheric and lower ionosphere attitudes above thunderstorms [*Sentman et al.*, 1995]. Sprites are most commonly associated with positive cloud-to-ground (+CG) lightning discharges with large charge moment changes. The charge moment is defined as the charge removed by cloud to ground lightning multiplied by altitude from which it was removed. The +CG with large charge moment change can produce quasi-electrostatic (QE) fields above thunderclouds, resulting in the electrical breakdown known as sprite phenomenon. Simultaneously, the transient SR waves produced by these large +CG lightning discharge are observed to be several times above the background SR noise [*Huang et al.*, 1999; *Sato and Fukunishi*, 2003]. *Huang et al.* [1999] developed a method to estimate the vertical charge moment change of the sprite-associated lightning using ELF data. The results from this method show that the charge moment of 200-2000 Ckm is sufficient to trigger conventional breakdown at the altitude of 70 - 90 km. Therefore, SR measurements represent a good way to monitor the global occurrence locations and rates of the sprites and

the associated lightning discharges [*Sato and Fukunishi*, 2003].

Due to the possible connections between Earth's climate and global lightning activity, SR observations can be applied to monitor the global environmental changes. *Williams* [1992] employs SR as a global tropical thermometer based on measurements of SR reflecting total world-wide lightning activity and its connection with average tropical surface temperature. As lightning activity is a temperature dependent phenomenon, SR parameters can be also employed to study the shift of the global thunderstorm activity in the warm El Niño and cold La Niña years [*Sátori and Zieger*, 1999]. In addition, the monitoring of SR might provide a convenient method for tracking upper-tropospheric water-vapour variability and hence contribute to a better understanding of the processes affecting climate change [*Price*, 2000]. Recently, there have been some reports related to the anomalous SR variations associated with a severe earthquake. *Hayakawa et al.* [2005] found anomalous Schumann resonance signals appeared from about one week to a few days before a severe earthquake (Chi-chi earthquake) on 21 September 1999 in Taiwan. A pronounced increase in the intensity of the Schumann resonance is obtained around the fourth SR mode, which is possibly related to the localized decrease in the lower ionospheric height over the earthquake epicenter. Similar increase in the intensity of the Schumann resonance is obtained around the fourth mode frequency (up to 20%) by *Nickolaenko et al.* [2006] using a numerical modeling.

In recent years, there has been also an increasing interest in exploration of other planets in the Solar System, and there have been a number of related publications [*Nickolaenko and Rabinowicz*, 1982; *Pechony and Price*, 2004; *Sentman*, 1990b] discussing the electromagnetic resonances in planetary cavities. There are two important factors to facilitate the existence of Schumann resonance on a planet.

One is that the planet surface and the ionosphere have high enough conductivity to reflect the electromagnetic waves and form a planetary resonant cavity for the propagation of the electromagnetic waves. The other is the existence of electrical discharges in this cavity, which can be considered as the source of the electromagnetic waves. On January 14, 2005, Huygens probe landed on Titan, and started the exploration of this largest moon of Saturn. One of multiple missions of Huygens probe is to detect if there are electrical discharges in the Titan's atmosphere and to investigate the electromagnetic property of Titan's lower ionosphere. It is believed that the conducting properties of the Titans atmosphere are favorable for the formation of cavity for propagation of electromagnetic waves, so the existence of SR will give a support for the existence of the electrical discharges in the lower atmosphere on Titan. Meanwhile, the SR parameters are also useful in the study of the electromagnetic properties of Titans lower ionosphere. This thesis presents a discussion and analysis of SR on Titan, Mars, and Venus.

1.4 Contributions to Knowledge

The purpose of this Ph.D dissertation research is to study the propagation of ELF waves and Schumann resonances in the Earth-ionosphere cavity and other planetary resonant cavities in the Solar System, and to better understand the connections between SR parameters and the global lightning activity as well as the atmospheric conductivity in these planetary resonant cavities.

The major scientific contributions resulting from this dissertation work are summarized below:

• Development of a new three-dimensional Finite Difference Time Domain (FDTD)

model with the inclusion of uniform and non-uniform atmospheric conductivity profiles, which allows the studies of SR parameters on the Earth and other celestial bodies in the Solar System and their associated changes with the diurnal and seasonal variations of the atmospheric conductivity and global lightning activity.

• Direct comparison of SR parameters derived from the FDTD model with realistic measurements, which indicates that the first SR frequency increases and decreases during X-ray bursts and solar proton events, respectively, due to the associated conductivity perturbations appearing at different altitudes in the Earth-ionosphere cavity during these two types of events.

• Identification of the global lighting activity and the positions of the three lightning centers (i.e., South-East Asia, Africa, and South America) with respect to the observation stations as the principal parameters determining the diurnal SR power variation patterns of the vertical electric component, and magnetic components in the North-South and East-West directions.

• Identification of the associated power variation of SR with the latitudinal migration of the thunderstorm centers due to El Niño and La Niña phenomena, which provides a new technique to detect the shifts of the thunderstorm regions related to the El Niño and La Niña phenomena using the combination of both electric and magnetic components of Schumann resonances at a single station.

• Development of a new genetic algorithm method for SR research, which allows the inverse extraction of the intensity of lighting activity in three lightning centers from experimental SR measurements, and reveals the different seasonal variations

of lightning activity in South-East Asia, Africa, and South America.

• Model investigation of the effects of the geomagnetic field on the propagation of the ELF waves in the Earth-ionosphere cavity, which indicates that the vertical electric component of SR can penetrate up to higher altitude with the presence of the geomagnetic field, and that the penetration height depends on the latitude of the observation points.

The results presented in this dissertation have been published in [*Yang and Pasko*, 2005; *Yang et al.*, 2006; *Yang and Pasko*, 2006, 2007].

Chapter 2

Model Formulation

2.1 Introduction of the Finite Difference Time Domain Method

The Finite-Difference Time-Domain (FDTD) method, as first proposed by *Yee* [1966], is a simple and elegant way to discretize the differential form of Maxwell's equations. The descriptor "Finite-Difference Time-Domain" and its corresponding "FDTD" acronym were originated by Allen Taflove in 1980 [*Taflove and Hagness*, 2000]. Since it is a time-domain method, solutions can cover a wide frequency range with a single simulation run. *Yee* [1966] used an electric field ($\vec{E}$) grid, which was offset both spatially and temporally from a magnetic field ($\vec{H}$) grid to obtain update equations that yield the present fields throughout the computational domain in terms of the past fields. The update equations are used in a leap-frog scheme to incrementally march the $\vec{E}$ and $\vec{H}$ fields forward in time. Despite the simplicity and elegance of Yee's algorithm, it did not receive much interest immediately after its publication. One could attribute the lack of attention to the high computational cost at the time that the algorithm was proposed. However,

as the shortcomings of the original FDTD implementation were alleviated and the cost of computing fell, FDTD techniques have emerged as a primary means to computationally model many scientific and engineering problems dealing with electromagnetic wave interactions with material structures.

Although several analytical mode theories about the ELF wave propagation in Earth-ionosphere cavity have been reported [e.g., *Galejs*, 1972; *Wait*, 1972; *Budden*, 1985], the FDTD technique [e.g., *Taflove and Hagness*, 2000] currently represents one of the simplest and most flexible means for solution of related problems in a medium with arbitrary inhomogeneities. Berenger was the first to use the FDTD method to model subionospheric wave propagation at frequencies below 300 kHz. His conference abstracts in this area date back to 1994 [*Berenger*, 1994]. His work had two initial goals: 1) to compare FDTD results with previous frequency-domain mode theory calculations [*Pappert and Ferguson*, 1986] and 2) to create an entirely new model having the capability of accommodating continuously varying parameters over the propagation path (see [*Simpson and Taflove*, 2007, and reference therein]). Several 2D FDTD models in spherical or cylindrical coordinate system have been developed for the solution of the ELF/VLF wave propagation problems within a distance of several thousand kilometers around the lightning source [e.g., *Pasko et al.*, 1998; *Thevenot et al.*, 1999; *Cummer*, 2000; *Berenger*, 2002; *Simpson and Taflove*, 2002; *Hu and Cummer*, 2006]. The fully global 3D FDTD model was first developed by *Otsuyama et al.* [2003]. In [*Otsuyama et al.*, 2003], the calculated radiated waveforms and wave impedances are compared at several distances (between 5 and 20 Mm) from the source to those predicted by previous analytical formulations [*Nickolaenko et al.*, 1999]. *Simpson and Taflove* [2004] have developed a global 3D FDTD model of the Earth-ionosphere waveguide below 1 kHz. Their model includes a means to reduce the eccentric-

ity of the cells in the polar regions by a novel adaptive cell-combining technique applied to adjacent grid-cells in the east-west direction. This technique permits maintenance of the time step at nearly the level allowed by the Courant stability condition for the square equatorial cells, yielding a greatly improved computational efficiency relative to conventional spherical-coordinate formulations [*Simpson and Taflove*, 2007]. The 3D FDTD model applied in this thesis is originally developed by *Yang and Pasko* [2005]. Theoretical and realistic atmospheric conductivity profiles are employed in this model to calculate SR parameters and their associated variations with exterior factors (e.g., atmospheric conductivity perturbations and global lightning activity) [*Yang and Pasko*, 2006, 2007]. The inclusion of the realistic conductivity profile derived from International Reference Ionosphere (IRI) in this model provides a more realistic description of the Earth-ionosphere cavity. *Yang et al.* [2006] used the FDTD method to solve SR problems on other celestial bodies in the solar system (e.g., Titan, Mars, and Venus).

2.2 Model Formulation of the Earth-Ionosphere Cavity

2.2.1 Modeling of Earth-Ionosphere Cavity Without the Presence of the Geomagnetic Field

The 3D FDTD model of the Earth-ionosphere cavity without the presence of the geomagnetic field has been introduced in [*Yang and Pasko*, 2005]. In this model, the atmosphere medium is isotropic, and the parameter used to account for the electromagnetic properties of the lower ionosphere is the conductivity profile (σ). A spherical simulation domain is assumed to be confined between two concentric

perfectly conducting spheres, with the radius of the inner sphere, corresponding to the Earth surface, set at a=6370 km, and with the surface of outer sphere positioned at altitude h=100 km (for other planets, the choice of this parameter is dependent on specific atmospheric conductivity distributions as will be separately discussed later in this thesis). The 3-D Maxwell equations in the spherical coordinates (r, θ, ϕ) are given by:

$$\varepsilon_0 \frac{\partial E_r}{\partial t} = \frac{1}{r \sin\theta} \left[\frac{\partial (\sin\theta H_\phi)}{\partial \theta} - \frac{\partial H_\theta}{\partial \phi} \right] - \sigma E_r$$

$$\varepsilon_0 \frac{\partial E_\theta}{\partial t} = \frac{1}{r} \left[\frac{1}{\sin\theta} \frac{\partial H_r}{\partial \phi} - \frac{\partial (r H_\phi)}{\partial r} \right] - \sigma E_\theta$$

$$\varepsilon_0 \frac{\partial E_\phi}{\partial t} = \frac{1}{r} \left[\frac{\partial (r H_\theta)}{\partial r} - \frac{\partial H_r}{\partial \theta} \right] - \sigma E_\phi$$

$$\mu_0 \frac{\partial H_r}{\partial t} = -\frac{1}{r \sin\theta} \left[\frac{\partial (\sin\theta E_\phi)}{\partial \theta} - \frac{\partial E_\theta}{\partial \phi} \right]$$

$$\mu_0 \frac{\partial H_\theta}{\partial t} = -\frac{1}{r} \left[\frac{1}{\sin\theta} \frac{\partial E_r}{\partial \phi} - \frac{\partial (r E_\phi)}{\partial r} \right]$$

$$\mu_0 \frac{\partial H_\phi}{\partial t} = -\frac{1}{r} \left[\frac{\partial (r E_\theta)}{\partial r} - \frac{\partial E_r}{\partial \theta} \right] \tag{2.1}$$

The 3-D FDTD equations are derived from the Maxwell's equations (2.1) in a classical manner [*Taflove and Hagness*, 2000]:

$$E_r^{n+1}(i+1/2,j,k) = e^{-\frac{\sigma\Delta t}{\varepsilon}} E_r^n(i+1/2,j,k) + \frac{1-e^{\frac{\sigma\Delta t}{\varepsilon}}}{\sigma} \frac{1}{r_{i+1/2}\sin\theta_j}$$

$$\left[\frac{\sin\theta_{j+1/2} H_\phi^{n+1/2}(i+1/2,j+1/2,k) - \sin\theta_{j-1/2} H_\phi^{n+1/2}(i+1/2,j-1/2,k)}{\Delta\theta} \right.$$

$$\left. - \frac{H_\theta^{n+1/2}(i,j+1/2,k+1/2) - H_\theta^{n+1/2}(i,j+1/2,k-1/2)}{\Delta\phi} \right]$$

$$E_\theta^{n+1}(i,j+1/2,k) = e^{-\frac{\sigma\Delta t}{\varepsilon}} E_\theta^n(i,j+1/2,k) + \frac{1-e^{\frac{\sigma\Delta t}{\varepsilon}}}{\sigma} \frac{1}{r_i}$$

$$\left[\frac{1}{\sin\theta_{j+1/2}} \frac{H_r^{n+1/2}(i,j+1/2,k+1/2) - H_r^{n+1/2}(i,j+1/2,k-1/2)}{\Delta\phi} \right.$$

$$\left. - \frac{r_{i+1/2} H_\phi^{n+1/2}(i+1/2,j+1/2,k) - r_{i-1/2} H_\phi^{n+1/2}(i-1/2,j+1/2,k)}{\Delta r} \right]$$

$$E_\phi^{n+1}(i,j,k+1/2) = e^{-\frac{\sigma\Delta t}{\varepsilon}} E_\phi^n(i,j,k+1/2) + \frac{1-e^{\frac{\sigma\Delta t}{\varepsilon}}}{\sigma} \frac{1}{r_i}$$

$$\left[\frac{r_{i+1/2} H_\theta^{n+1/2}(i+1/2,j,k+1/2) - r_{i-1/2} H_\theta^{n+1/2}(i-1/2,j,k+1/2)}{\Delta r} \right.$$

$$\left. - \frac{H_r^{n+1/2}(i,j+1/2,k+1/2) - H_r^{n+1/2}(i,j-1/2,k+1/2)}{\Delta\theta} \right]$$

$$H_r^{n+1/2}(i,j+1/2,k+1/2) = H_r^{n-1/2}(i,j+1/2,k+1/2) - \frac{\Delta t}{\mu_0} \frac{1}{r_i \sin\theta_{j+1/2}}$$

$$\left[\frac{\sin\theta_{j+1}E_\phi^n(i,j+1,k+1/2)-\sin\theta_j E_\phi^n(i,j,k+1/2)}{\Delta\theta}\right.$$
$$\left.-\frac{E_\theta^n(i,j+1/2,k+1)-E_\theta^n(i,j+1/2,k)}{\Delta\phi}\right]$$

$$H_\theta^{n+1/2}(i+1/2,j,k+1/2)=H_\theta^{n-1/2}(i+1/2,j,k+1/2)-\frac{\Delta t}{\mu_0}\frac{1}{r_{i+1/2}}$$
$$\left[\frac{1}{\sin\theta_j}\frac{E_r^n(i+1/2,j,k+1)-E_r^n(i+1/2,j,k)}{\Delta\phi}\right.$$
$$\left.-\frac{r_{i+1}E_\phi^n(i+1,j,k+1/2)-r_iE_\phi^n(i,j,k+1/2)}{\Delta r}\right]$$

$$H_\phi^{n+1/2}(i+1/2,j+1/2,k)=H_\phi^{n-1/2}(i+1/2,j+1/2,k)-\frac{\Delta t}{\mu_0}\frac{1}{r_{i+1/2}}$$
$$\left[\frac{r_{i+1}E_\theta^n(i+1,j+1/2,k)-r_iE_\theta^n(i,j+1/2,k)}{\Delta r}\right.$$
$$\left.-\frac{E_r^n(i+1/2,j+1,k)-E_r^n(i+1/2,j,k)}{\Delta\theta}\right] \tag{2.2}$$

where Δt is the time step, Δr, $\Delta\theta$, and $\Delta\phi$ are spatial grid discretization steps in r, θ, and ϕ directions, with corresponding grid positions marked by indexes i, j, and k, respectively.

Figure 2.1 shows the geometry of the 3D spherical FDTD cells. The electric field components are set at the edges of each cell, and the magnetic field component are all located at the centers of the cell's sides. Important discontinuities exist in the spherical coordinate system along the north-south (N-S) axis at $\theta = 0$ and $\theta = \pi$ (i.e., at the North and South poles). To overcome this discontinuity, the

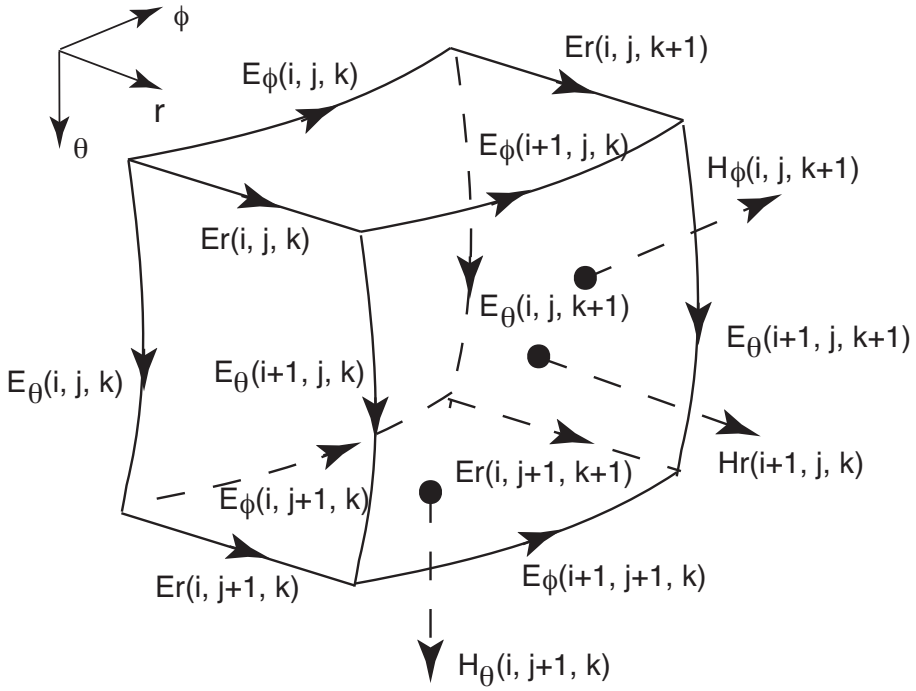

Figure 2.1. The geometry of the 3D spherical FDTD cells. The indexes, i, j, and k indicate the cell number in r, θ, and ϕ directions, respectively.

integral form of Maxwell's equations is employed to solve E_r component at two poles instead of equations (2.1).

The time step of the FDTD model is determined by the Courant condition [*Taflove and Hagness*, 2000]:

$$\Delta t \leq \Delta t_c = \frac{1}{c}\left[\frac{1}{\Delta S_r^2} + \frac{1}{\Delta S_\theta^2} + \frac{1}{\Delta S_\phi^2}\right]^{-1/2} \tag{2.3}$$

where ΔS_r, ΔS_θ, and ΔS_ϕ are the smallest size of the FDTD cells in the r, θ, and ϕ direction, respectively.

2.2.2 Modeling of Earth-Ionosphere Cavity With the Presence of the Geomagnetic Field

The geomagnetic field plays a very important role in the Earth-ionosphere cavity. The atmosphere becomes anisotropic due to the geomagnetic fields, especially above 70 km. In present modeling, a magnetic dipole model is employed to account for the geomagnetic field in the whole Earth-ionosphere cavity [*Walt*, 1994]. The north and south geomagnetic poles are located at $\theta = 180^o$ and 0^o, respectively. The distributions of the geomagnetic field in r, θ, and ϕ directions are given as:

$$\begin{aligned} B_r &= -2B_0 \left(\frac{R_E}{r}\right)^3 \cos\theta \\ B_\theta &= -B_0 \left(\frac{R_E}{r}\right)^3 \sin\theta \end{aligned} \tag{2.4}$$

where R_E is the radius of the Earth, B_0 indicates the mean value of the field on the equator at Earth's surface, which is approximately equal to 3.12×10^{-5} T, r is the distance measured from the center of the dipole, and θ stands for the angle from the observation point to the north pole. The dipole field is symmetric about its axis, so that $B_\phi = 0$ everywhere.

The continuous Maxwell's equations including the geomagnetic field in the realistic cavity are given as following [*Thevenot et al.*, 1999]:

$$\begin{aligned} \nabla \times \vec{E} &= -\mu_0 \frac{\partial \vec{H}}{\partial t} \\ \nabla \times \vec{H} &= \varepsilon_0 \frac{\partial \vec{E}}{\partial t} + \vec{J}_{tot} \\ \frac{\partial \vec{J}_e}{dt} - \frac{q_e}{m_e}\vec{J}_e \times \vec{B}_E + \nu_e \vec{J}_e &= \frac{N_e q_e^2}{m_e}\vec{E} \\ \frac{\partial \vec{J}_i}{dt} - \frac{q_i}{m_i}\vec{J}_i \times \vec{B}_E + \nu_i \vec{J}_i &= \frac{N_i q_i^2}{m_i}\vec{E} \end{aligned} \tag{2.5}$$

where $m_{i,e}$ and $q_{i,e}$ indicate the mass and charge of the ion and electron, respectively, $\vec{B}_E$ indicates the geomagnetic field, $\vec{J}_{i,e}$ are ion and electron current densities, and $\vec{J}_{tot} = \vec{J}_i + \vec{J}_e$. The current density components are all placed at the same positions as the electric field components (see Figure 2.1). The definitions of the density profiles ($N_{i,e}$), and the collision frequencies ($\nu_{i,e}$) will be given in the subsequent sections of this thesis and will depend on particular model situation considered.

The electron and ion current density equations (2.5) can be separated into three scalar equations corresponding to in r, θ, and ϕ directions, respectively. Here, we will give the detailed derivation of the electron current density, and similar procedure can be applied to the ion current density. For the electron current density, three scalar equations derived from equation (2.5) are:

$$\begin{aligned}
&\frac{\partial J_{er}}{\partial t} + \nu_e J_{er} - \frac{q_e}{m_e} B_\phi J_\theta + \frac{q_e}{m_e} B_\theta J_\phi = \frac{N_e q_e^2}{m_e} E_r \\
&\frac{\partial J_{e\theta}}{\partial t} + \nu_e J_{e\theta} - \frac{q_e}{m_e} B_r J_\phi + \frac{q_e}{m_e} B_\phi J_r = \frac{N_e q_e^2}{m_e} E_\theta \\
&\frac{\partial J_{e\phi}}{\partial t} + \nu_e J_{e\phi} - \frac{q_e}{m_e} B_\theta J_r + \frac{q_e}{m_e} B_r J_\theta = \frac{N_e q_e^2}{m_e} E_\phi
\end{aligned} \tag{2.6}$$

where J_{er}, $J_{e\theta}$, and $J_{e\phi}$ are the electron current density components in r, θ, and ϕ directions, respectively. To solve these differential equations, $\vec{J}$ is found at time step $n + 1/2$ as a function of its value at time step $n - 1/2$ as:

$$J_{er}^{n+1/2} = e^{-\nu_e \Delta t} J_{er}^{n-1/2} + \frac{1 - e^{-\nu_e \Delta t}}{\nu} \times$$

$$\left(\frac{q_e}{m_e} B_\phi \frac{J_\theta^{n-1/2} + J_\theta^{n+1/2}}{2} - \frac{q_e}{m_e} B_\theta \frac{J_\phi^{n-1/2} + J_\phi^{n+1/2}}{2} + \frac{N_e q_e^2}{m_e} E_r \right)$$

$$J_{e\theta}^{n+1/2} = e^{-\nu_e \Delta t} J_{e\theta}^{n-1/2} + \frac{1 - e^{-\nu_e \Delta t}}{\nu} \times$$

$$\left(\frac{q_e}{m_e} B_r \frac{J_\phi^{n-1/2} + J_\phi^{n+1/2}}{2} - \frac{q_e}{m_e} B_\phi \frac{J_r^{n-1/2} + J_r^{n+1/2}}{2} + \frac{N_e q_e^2}{m_e} E_\theta \right)$$

$$J_{e\phi}^{n+1/2} = e^{-\nu_e \Delta t} J_{e\phi}^{n-1/2} + \frac{1 - e^{-\nu_e \Delta t}}{\nu} \times$$

$$\left(\frac{q_e}{m_e} B_\theta \frac{J_r^{n-1/2} + J_r^{n+1/2}}{2} - \frac{q_e}{m_e} B_r \frac{J_\theta^{n-1/2} + J_\theta^{n+1/2}}{2} + \frac{N_e q_e^2}{m_e} E_\phi \right) \tag{2.7}$$

Equations (2.7) can be rewriten as following:

$$A \begin{bmatrix} J_{er}^{n+1/2} \\ J_{e\theta}^{n+1/2} \\ J_{e\phi}^{n+1/2} \end{bmatrix} = B \begin{bmatrix} J_{er}^{n-1/2} \\ J_{e\theta}^{n-1/2} \\ J_{e\phi}^{n-1/2} \end{bmatrix} + F_\nu \frac{N q_e^2}{m_e} \begin{bmatrix} E_{er}^{n} \\ E_{e\theta}^{n} \\ E_{e\phi}^{n} \end{bmatrix} \tag{2.8}$$

where:

$$A = \begin{bmatrix} 1 & F_\nu \frac{-q_e B_\phi}{2m_e} & F_\nu \frac{q_e B_\theta}{2m_e} \\ F_\nu \frac{q_e B_\phi}{2m_e} & 1 & F_\nu \frac{-q_e B_r}{2m_e} \\ F_\nu \frac{-q_e B_\theta}{2m_e} & F_\nu \frac{q_e B_r}{2m_e} & 1 \end{bmatrix}$$

and

$$B = \begin{bmatrix} e^{-\nu \Delta t} & F_\nu \frac{q_e B_\phi}{2m_e} & F_\nu \frac{-q_e B_\theta}{2m_e} \\ F_\nu \frac{-q_e B_\phi}{2m_e} & e^{-\nu \Delta t} & F_\nu \frac{q_e B_r}{2m_e} \\ F_\nu \frac{q_e B_\theta}{2m_e} & F_\nu \frac{-q_e B_r}{2m_e} & e^{-\nu \Delta t} \end{bmatrix}$$

$$F_\nu = \frac{1 - e^{-\nu \Delta t}}{\nu}$$

This yields the following set of equations for the advance of time on components

J_{er}, $J_{e\theta}$, and $J_{e\phi}$:

$$\begin{bmatrix} J_{er}^{n+1/2} \\ J_{e\theta}^{n+1/2} \\ J_{e\phi}^{n+1/2} \end{bmatrix} = (A^{-1}B) \begin{bmatrix} J_{er}^{n-1/2} \\ J_{e\theta}^{n-1/2} \\ J_{e\phi}^{n-1/2} \end{bmatrix} + F_\nu \frac{Nq_e^2}{m}(A^{-1}) \begin{bmatrix} E_{er}^{n} \\ E_{e\theta}^{n} \\ E_{e\phi}^{n} \end{bmatrix} \tag{2.9}$$

For instance, the equation for the advance of J_{er} at point $(i+1/2,j,k)$ is

$$J_{er}^{n+1/2}(i+1/2,j,k) = (A^{-1}B)_{11}J_{er}^{n-1/2}(i+1/2,j,k) + (A^{-1}B)_{12}J_{e\theta}^{n-1/2}(i+1/2,j,k)$$

$$+ (A^{-1}B)_{13}J_{e\phi}^{n-1/2}(i+1/2,j,k) + F_\nu \frac{N_e q_e^2}{m_e}(A_{11})E_{er}^{n-1/2}(i+1/2,j,k) +$$

$$F_\nu \frac{N_e q_e^2}{m_e}(A_{12})E_{e\theta}^{n-1/2}(i+1/2,j,k) + F_\nu \frac{N_e q_e^2}{m_e}(A_{13})E_{e\phi}^{n-1/2}(i+1/2,j,k) \tag{2.10}$$

With the mesh shown in Figure 2.1, we find that these three current density and electric field components are not available at the same points, so equation (2.8) can not be employed directly. For example, J_{er} and E_{er} are defined at point $(i+1/2,$ $j,$ $k)$. However, $J_{e\theta}$ and $E_{r\theta}$ are defined at point $(i,$ $j+1/2,$ $k)$, and $J_{e\phi}$ and $E_{r\phi}$ are defined at point $(i,$ $j,$ $k+1/2)$. For derivation of J_r in equation (2.10), the average values of the four closest $J_{e\theta}$ and $J_{e\phi}$ components are used as the values of these two components at point $(i+1/2,$ $j,$ $k)$, where the J_{er} component is placed

$$J_{e\theta}^{n-1/2}(i+1/2,j,k) = \Big[J_{e\theta}^{n-1/2}(i,j-1/2,k) + J_{e\theta}^{n-1/2}(i,j-1/2,k) +$$

$$J_{e\theta}^{n-1/2}(i+1,j+1/2,k) + J_{e\theta}^{n-1/2}(i+1,j+1/2,k)\Big]/4 \tag{2.11}$$

$$J_{e\phi}^{n-1/2}(i+1/2,j,k) = \Big[J_{e\phi}^{n-1/2}(i,j,k-1/2) + J_{e\phi}^{n-1/2}(i,j,k+1/2) +$$

$$J_{e\phi}^{n-1/2}(i+1,j,k-1/2)+J_{e\phi}^{n-1/2}(i+1,j,k+1/2)\Big]/4 \tag{2.12}$$

Similar averaging procedures also are used for the $J_{e\theta}$ and $J_{e\phi}$ parts of equation (2.8).

Due to the employment of the electron density and collision frequency profiles in this model, the numerical stability criterion differs from that in the modeling without the presence of the geomagnetic field. According to [*Thevenot et al.*, 1999], the time step is determined by

$$\Delta t \leq \Delta t_c = \frac{1}{c}\left[\frac{1}{\Delta S_r^2}+\frac{1}{\Delta S_\theta^2}+\frac{1}{\Delta S_\phi^2}+\frac{\mu_0\chi}{4}\right]^{-1/2} \tag{2.13}$$

where $\chi = \frac{N_{max}q_e^2}{m_e}$, and N_{max} is the largest value of the electron density used in the simulation. Due to the large number density of the electrons at high altitude, χ is the significant parameter determining the time step.

The typical number of FDTD cells in r, θ and ϕ directions are 20, 20 and 40, respectively. The cavity is excited by a vertical lightning current with a 5 km length, which has a linear rise time of 500 μs and exponential fall with time scale 5 ms. The reported results for frequencies <40 Hz are not sensitive to the specifics of the chosen lightning current waveform.

The sources and receivers are located at different positions depending on the specifics of the problem to be solved. In the simulations related to eigenfrequencies of Earth-ionosphere cavity and SR on other planets (Chapters 3 and 6), the lightning source is positioned near the planet surface at $0°N$, $0°E$ and results are presented for a vertical electric field component E_r detected at the ground surface by a set of receivers at $18°N$ $0°E$, $36°N$ $0°E$, $54°N$ $0°E$, $72°N$ $0°E$, and $90°N$ $0°E$. In the studies related to the diurnal and seasonal variations of SR parame-

ters (Chapter 4, 5 and 7), the sources are located at the locations corresponding to three main lightning regions at Africa, South-East Asia and South America, respectively [*Sentman*, 1995]. The simulated receivers are positioned near the locations of the SR field stations in Israel [*Price and Melnikov*, 2004] and Hungary [*Sátori et al.*, 1996] to collect the vertical electric field component E_r and magnetic field components in East-West (H_{EW}) and North-South (H_{NS}) directions.

We report results on first several SR eigenfrequencies f_n and associated Q-factors Q_n obtained from the modeled E_r power spectrum (Q_n=$f_n/\Delta f_n$, where Δf_n is the full width at half maximum power of the nth mode) in Chapters 3 and 6. In Chapters 4, 5 and 7, the eigenfrequencies f_n are derived from three components (E_r, H_θ, and E_ϕ). The SR eigenfrequencies and Q factors of the cavity are evaluated using Prony's method by fitting the time domain data with complex polynomials, $\sum_{i=1}^{n} A_i \exp(j\omega_i t)$ [*Hildebrand*, 1956; *Füllekrug*, 1995], where A_i are the complex amplitudes of the resonances, and ω_i indicates the complex propagation parameters. The SR eigenfrequencies and Q factors of the cavity can be defined as $\frac{Re(\omega_i)}{2\pi}$ and $\frac{Re(\omega_i)}{2Im(\omega_i)}$, respectively.

2.3 Electromagnetic Properties of the Cavity

2.3.1 Spherically Symmetric Uniform Conductivity Profiles

The conductivity profile is the most important parameter employed in our FDTD simulations, since SR frequencies and Q-factors are mainly determined by the conductivity distribution in the cavity. In the discussion related to eigenfrquencies in the cavity in Chapter 3, the cavity is assumed to be spherically symmetric

and characterized by four different altitude profiles of conductivity $\sigma(z)$. The first profile corresponds to an ideal, free space cavity with $\sigma(z)$=0, which has an analytical solution for the resonance frequencies given by equation (1.1). The second profile used in Chapter 3 is a single-exponential profile with a perturbation [*Sentman*, 1983]:

$$\sigma(z) = \sigma_0 \exp\left[\frac{z}{\xi_0} + 2.303\beta \exp - \left(\frac{z - z_0}{a}\right)^2\right] S/m \tag{2.14}$$

where σ_0=10^{-16} S/m, ξ_0=3.1 km, a and z_0 indicate the center altitude and width of the perturbation, respectively, and the parameter β describes the amplitude of the perturbation in powers of ten about its unperturbed value. To account for the perturbation produced by high energy particle precipitation and X-ray bursts, we insert perturbation at 40 and 70 km, respectively, whose amplitudes are 1000 times that of the unperturbed value (see Chapter 3). The third profile is a two-exponential profile [*Greifinger and Greifinger*, 1978; *Sentman*, 1990a, 1996a]. In the development of SR theory, the two-exponential profile plays a very important role. This profile is based on a division of atmosphere into lower (from ground and up to ~60-70 km) and upper (above ~60-70 km) layers with conductivity profiles:

$$\sigma(z) = \begin{cases} \sigma(h_1) \exp\left[(z - h_1)/\xi_1\right] \\ \sigma(h_2) \exp\left[(z - h_2)/\xi_2\right] \end{cases} \tag{2.15}$$

where h_1=50 km, ξ_1=5 km, h_2=93.5 km, ξ_2=5 km, $\sigma(h_1)$=$2\pi f_0 \varepsilon_0$=4.44×10^{-10} S/m, and $\sigma(h_2)$=$1/8\mu_0\pi f_0 \xi_1^2$=1.58×10^{-4} S/m assuming f_0= 8 Hz. The fourth conductivity profile corresponds to the so-call "knee" model [*Mushtak and Williams*,

2002]. It can be written as:

$$\sigma(z) = \begin{cases} \sigma_{kn} \exp[(z - h_{kn})/\xi_b] & z < h_{kn} \\ \sigma_{kn} \exp[(z - h_{kn})/\xi_a] & z > h_{kn} \end{cases} \tag{2.16}$$

where h_{kn}=55 km, ξ_a=2.9 km, ξ_b=8.3 km, and $\sigma_{\mathrm{kn}}=2\pi f_{\mathrm{kn}}\varepsilon_0=5.56\times10^{-10}$ S/m assuming f_{kn}=10 Hz. The specific choice of parameters for profiles 2-4 is largely motivated by the availability of solutions to related problems [*Sentman*, 1983; *Mushtak and Williams*, 2002], against which the FDTD results presented in Chapter 3 are compared.

Since the vertical conductivity profile on some planets, e.g., Venus, can not be approximated by a "knee" model profile, in the discussion of Schumann resonances on other planets (Chapter 6), a "double-knee" model developed by [*Pechony and Price*, 2004] is employed. The "double-knee" profile is formulated as:

$$\sigma(z) = \begin{cases} \sigma_1 \exp[(z - h_1)/\xi_1] & z < h_1 \\ \sigma_2 \exp[(z - h_2)/\xi_2] & z > h_2 \end{cases} \tag{2.17}$$

where σ_1, σ_2 are conductivities at two "knee" altitudes h_1 and h_2, and ξ_1 and ξ_2 are the scale heights of the conductivity below first and above second knee, respectively. The conductivity between h_1 and h_2 is given by:

$$\sigma(z) = \exp\left[\frac{z[ln(\sigma_1) - ln(\sigma_2)] + (h_1 ln(\sigma_2) - h_2 ln(\sigma_1)}{h_1 - h_2}\right] \qquad h_1 < z < h_2. \tag{2.18}$$

The choice of the specific parameters (σ_1, σ_2, ξ_1, ξ_2, h_1, and h_2) for the resonant cavities on different planets is discussed in Chapter 6.

2.3.2 Non-Uniform Conductivity Profiles

In Section 2.3.1, we have introduced four spherically symmetric uniform conductivity profiles used in our simulations. Although, these conductivity profiles can lead to SR frequencies which are very close to those measured experimentally, more differences are found between these profiles and the realistic ones. In the realistic cavity, the conductivity profile in the cavity is strongly modulated depending on the solar radiation. Therefore, an obvious day-night asymmetry appears in the Earth-ionosphere cavity, which can not be described by a spherically symmetric uniform conductivity profiles. In [*Pechony and Price*, 2004], a simplified method, partial uniform knee model (PUK), is developed to treat the day-night asymmetry. In PUK model, the Earth-ionosphere cavity is divided into two parts. One corresponds to the day time, and the second one is related to night time. At each side of the cavity, a "knee" model with different parameters is employed. Although, PUK model introduces the day-night asymmetry into the cavity, the conductivity profile is still uniform at the day or night sides. In Chapter 4 of this thesis, a more precise model of the realistic profile is employed by using the International Reference Ionosphere (IRI) model [*Bilitza*, 2001]. At altitudes <60 km in the Earth's atmosphere, the total conductivity is dominated by the ion conductivity, σ_i. In this thesis, the ion conductivity profile is taken from [*Hale*, 1984; *Huang et al.*, 1999]. Above 60 km, the electron conductivity σ_e is dominant over the ion conductivity σ_i, and can be determined by

$$\sigma_e = N_e q_e \mu_e \tag{2.19}$$

where q_e is the charge of the electron, μ_e is the mobility of the electron given by $\mu_e = 1.36 N_0/N \ (m^2/Vs)$, $N_0 = 2.688 \times 10^{25} \ m^{-3}$, and N is altitude dependent number density of air molecules [*Pasko et al.*, 1997]. The electron density in the

cavity, N_e, is derived from the IRI model at a specific time, corresponding to different times during the diurnal cycle and to different seasons, as specific in Chapter 4, 5 and 7. The total conductivity σ is given by $\sigma = \sigma_i + \sigma_e$.

2.3.3 Electron Density and Collision Frequency Profiles

When the ionosphere is treated as cold plasma, the parameters applied to describe the electromagnetic properties of the ionosphere are the densities (N_e and N_i) and collision frequencies (ν_e and ν_i) of the electrons and ions with the neutral gas. Besides the electron density derived from IRI (discussed in Section 2.3.2), in this thesis we also employ vertical electron density model defined by:

$$N_e(z) = 1.43 \times 10^{13} \exp(-0.15h') \exp(\beta - 0.15)(z - h')(m^{-3}) \tag{2.20}$$

where β and h' are 0.5 and 87, respectively [*Thevenot et al.*, 1999]. The model density specified by (2.20) is assumed to maintain (at z >100 km) a constant value corresponding to 100 km altitude. The electron collision frequency is determined by $\nu_e = \frac{q_e}{m_e \mu_e}$, where μ_e is the mobility of the electrons, which is defined in Section 2.3.2. The density (N_i) and collision frequency (ν_i) of ions are taken from [*Cummer*, 2000]. The additional detailed information is presented in Chapter 8.

Chapter 3

The Variations of Schumann Resonance Parameters Associated With Solar Proton Events and X-Ray Bursts

3.1 Introduction

The frequencies of Schumann resonances have been discussed since the first day of the discovery of SR. For an ideal cavity, the SR frequency can be easily calculated using equation (1.1) or (1.2). However, since the atmosphere becomes conducting due to the free electrons and ions produced by the solar radiation and cosmic rays, the experimentally measured SR frequencies are actually lower than the ideal ones. A number of different theoretical approaches have been used to describe the electromagnetic properties of the ionosphere and the propagation of the Extremely Low Frequency (ELF) signals in the Earth-ionosphere cavity [*Wait*, 1972; *Galejs*,

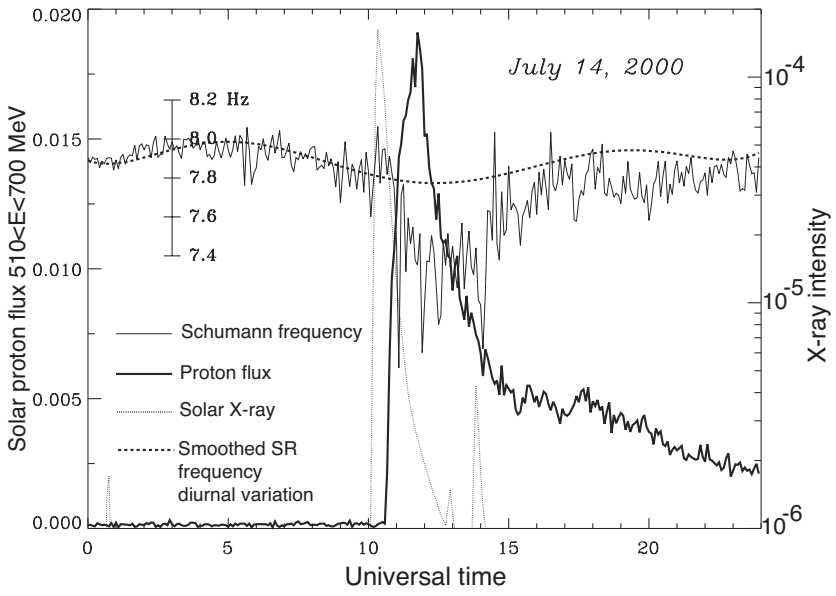

Figure 3.1. An example of the experimental measurements of the SR frequency variations during SPEs and X-ray bursts (figure courtesy of [*Roldugin et al.*, 2003]). The figure illustrates changes of the first SR frequency at Lovozero station (the thin line), energetic proton flux (the bold line) and solar X-ray intensity (the dotted line) detected by GOES 10 satellite during the solar proton event of 14 July 2000. The bold dashed line is the smoothed diurnal variation of SR frequency for adjacent quiet days.

1972; *Nickolaenko and Hayakawa*, 2002]. The two-exponential conductivity profile [*Sentman*, 1996a] and "knee" model [*Mushtak and Williams*, 2002] have played an important role in the development of analytical theory of Schumann resonances. The SR frequencies derived from these two profiles have good agreement with the realistic measurement results. The resonant frequency of a cavity is mainly determined by the size of the cavity and the electromagnetic properties of the cavity. For the Earth-ionosphere cavity with a fixed size, the ionospheric conductivity profile is the most important factor to influence SR frequencies. Any perturbation of the ionospheric conductivity leads to the corresponding SR frequency variations. *Schlegel and Fullekrug* [1999] found that the additional ionization of the ionosphere associated with the high-energy particle precipitation during the nine strongest solar proton events of the past solar cycle 22 led to an increase of the res-

onance frequency and a decrease of the damping of the first Schumann resonance. The authors related this increase with the proton precipitation and not with X-ray bursts. Other measurements by *Roldugin et al.* [2001, 2003] at Russian observatories Lovozero (the Kola Peninsula) and Lekhta (Karelija) show that SPEs lead to the decrease of frequencies of the first and second SR modes of similar to 0.4 Hz and the increase of the first-mode bandwidth from 0.8 to 1.5 Hz. *Roldugin et al.* [2004] studied variations of the Schumann resonance frequency in the Kola and Kamchatka Peninsulas during seven days of March-April, 2001, when the intensive solar X-ray bursts occurred. All X-ray bursts were accompanied by ∼0.2 Hz increase in the first mode frequency, at least in one of the magnetic components. For the second mode the increase (in average by ∼0.3 Hz) was registered in most events. Figure 3.1 illustrates the measurements from [*Roldugin et al.*, 2001] which were conducted on July 14, 2000. SR frequency is observed increasing by 0.1 Hz between 1000 and 1100 UT with the X-ray burst, and the SPE following the X-ray burst from 1100 to 2000 UT leads to a 0.4 Hz decrease of the first SR frequency.

In this Chapter, the number of FDTD cells in r, θ and ϕ directions are 20, 20 and 40, respectively. The two-exponential conductivity profile [*Sentman*, 1996a] and "knee" model [*Mushtak and Williams*, 2002] are applied with our FDTD model, and the FDTD results are compared with the results reported by previous analytical studies. A single-exponential conductivity profile with perturbations is employed to model the SR frequency variations with the conductivity perturbations due to SPEs and X-ray bursts.

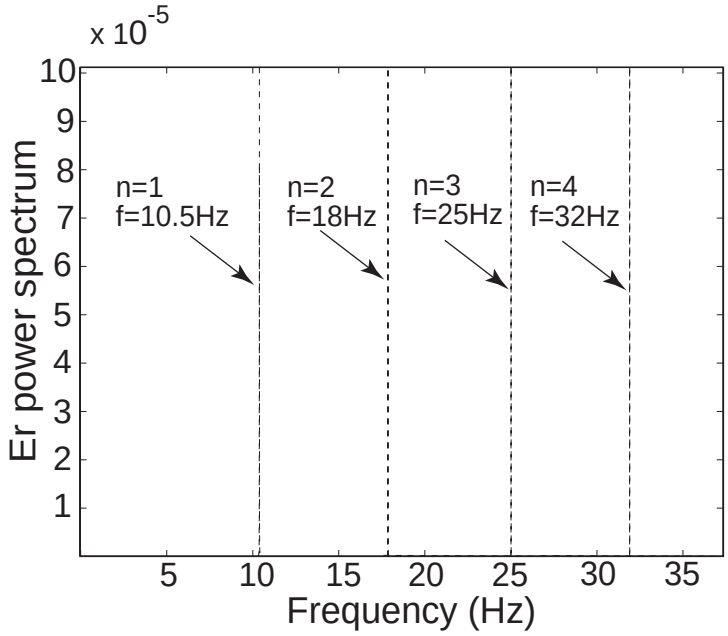

Figure 3.2. The power spectrum of the first four Schumann resonance modes in an ideal cavity derived from FDTD model.

3.2 Schumann Resonances in a Cavity With Spherically Uniform Conductivity Profiles

The first conductivity profile we consider corresponds to zero conductivity $\sigma = 0$ anywhere in the cavity, which means that the cavity is a lossless resonant system. Figure 3.2 illustrates the E_r power spectra obtained with FDTD model for an ideal cavity at $18°N$ $0°E$, about 2000 km from the source. The first four modes are clearly observed at 10.5, 18, 25, 32 Hz, respectively. The errors are within 3% of the respective values 10.52, 18.2, 25.76 and 33.26 Hz obtained from equation (1.1). Comparing with the realistic measurements shown in Figure 1.2, since there is no energy dissipation in this model resonant system, the half-power bandwidth of each mode is zero in Figure 3.2, and the corresponding Q-factors of each mode are infinity. Figure 3.3 illustrates the single-exponential profile and "knee" profile,

which are employed in our simulations. The specific choice of parameters for these profiles has been discussed in Section 2.3.1. Figures 3.4 and 3.5 show the time domain data and power spectrum of E_r component detected at the point about 2000 km from the source in the model cavity (solid lines), which were obtained with those two profiles, respectively. The dashed lines in Figures 3.4 and 3.5 indicate the approximation results using Prony's method discussed in Section 2.2. In the low Q-factor system like Earth-ionosphere cavity, the half power bandwidth of each mode is big enough to lead to interference of the adjacent modes and to deviation of the peak SR frequencies from the SR eigenfrequencies. The very close approximation of SR data using Prony's method shows that this method is a good tool to extract the SR eigenfrequency from FDTD results. The f_n and Q_n values shown in Figure 3.4 for single-exponential profile and in Figure 3.5 for the "knee" profile, are also included in Table 3.1 along with the reference theoretical data for the same profile from [*Ishaq and Jones*, 1977], which have been discussed recently in the context of different analytical SR models by *Mushtak and Williams* [2002]. The FDTD and *Ishaq and Jones* [1977] results agree within 3% in terms of both f_n and Q_n values for the first five modes considered. The quasi-DC component in Figures 3.4 and 3.5 is due to the static charges deposited by the model lightning current in the vicinity of the conducting Earth sphere. The discussion of the DC component is beyond the scope of the present work and we only note here that in addition to other factors (i.e., distance to the source, atmospheric conductivity, etc) its representation in the frequency domain is generally a function of the total sampling time.

Figure 3.6(a) shows the global averages of the E_r and E_θ components between ground and 100 km for the unperturbed single-exponential conductivity profile. For the E_r component, the field magnitude is constant from the ground to 50 km, and

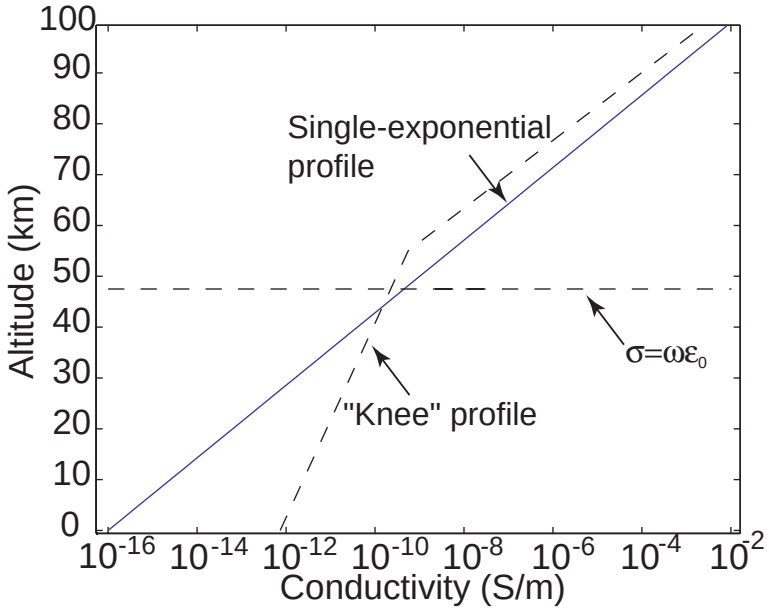

Figure 3.3. The single-exponential profile [*Sentman*, 1983] and "knee" profile [*Mushtak and Williams*, 2002]. The horizontal dashed line indicates the conducting boundary for the frequency, ω, defined by a condition $\sigma = \omega\varepsilon_0$.

Mode number (n)	Reference model [Ishaq and Jones,1977]		FDTD with "Knee" profile		Two-exponential model (Table 4 [Mushtak and Williams, 2002])		FDTD with two-exponential profile		FDTD with single-exponential profile	
	f_n	Q_n	f_n	Q_n	f_n	Q_n	f_n	Q_n	f_n	Q_n
1	7.7	4.1	7.7	4.1	7.7	4.2	7.6	4.2	7.54	6.1
2	14.0	4.9	13.9	4.9	13.9	4.3	13.6	4.1	13.4	6.2
3	20.2	5.4	20.0	5.5	20.2	4.3	19.7	4.2	19.2	6.3
4	26.5	5.9	25.9	6.0	26.6	4.4	25.8	4.4	24.8	6.4
5	32.8	6.3	32.1	6.4	33.1	4.4	32.0	4.6	30.4	6.3

Table 3.1. Comparison of FDTD results and previous modeling results obtained with spherically symmetric uniform conductivity profile.

decreases exponentially above 50 km. The E_θ component increases from zero at the ground and reached maximum at 50 km. Above 50 km, E_θ component decreases with the altitude, but the decrease rate is much smaller than that of E_r component. Therefore, it is found that the electrical field concentrate in vertical direction below about 70 km, but in parallel direction above 70 km. These results can be

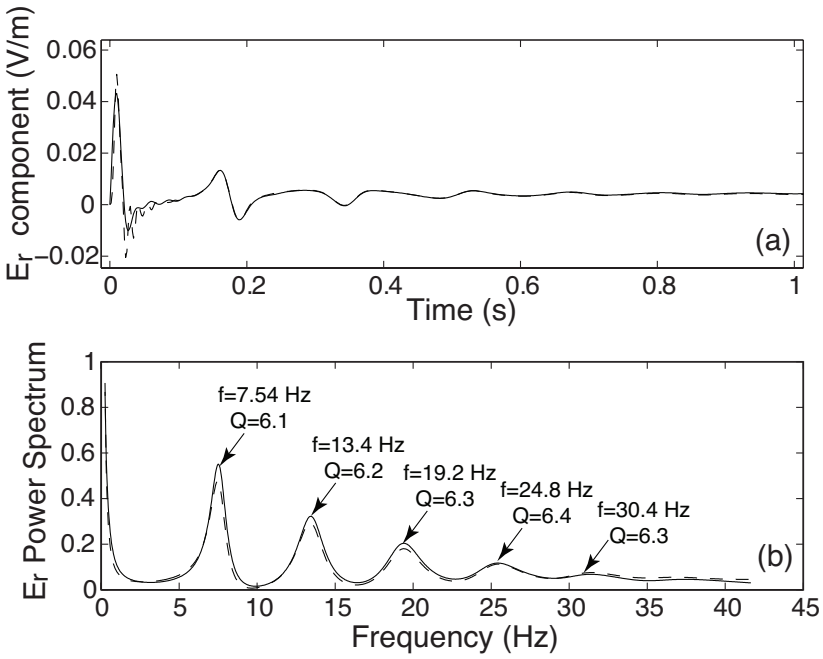

Figure 3.4. The FDTD time domain data (a) and power spectrum (b) of the E_r component derived from the cavity with single-exponential profile shown in figure 3.3.

interpreted following ideas presented by *Sentman* [1983] based on introduction of a reference boundary defined by a condition $\omega = \sigma/\varepsilon_0$ (shown in Figure 3.3 assuming ω=$2\pi\times 8$ Hz) dividing the atmosphere into two altitude regions dominated by displacement (below it) and conduction (above it) currents. Below this boundary the electric field is predominantly vertical and its behavior is similar to that in loss-less free space resonator, while above it the vertical component of the field drops exponentially due to large conductivity, with the field becoming virtually parallel to the Earth's surface above 80 km [*Sentman*, 1983]. The total power dissipation in the cavity is calculated following $P(r) = \sigma|E_r(r)|^2 + \sigma|E_\theta(r)|^2$, where r is the altitude. Two peaks of the power dissipation related to the E_r and E_θ components are found at 50 km and 85 km, respectively (shown in Figure 3.6(b)).

According to [*Nickolaenko and Hayakawa*, 2002], the spatial distributions of the E_r and H_ϕ components around the source follow the Legendre ($P_n(\cos\theta)$) and

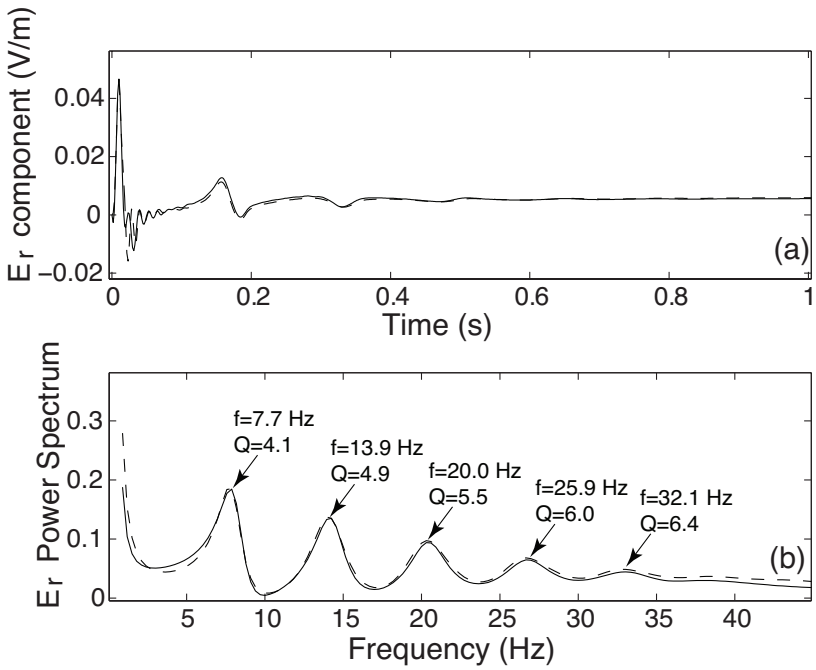

Figure 3.5. The FDTD time domain data (a) and power spectrum (b) of the E_r component derived from the cavity with "knee" profile shown in figure 3.3.

associated Legendre ($P_n^1(\cos\theta)$) polynomials and are given as:

$$E_r(\omega) = \frac{i\nu(\nu+1)}{\omega}\frac{M_C(\omega)}{4\pi\varepsilon h a^2}\sum_{n=0}^{\infty}\frac{(2n+1)P_n(\cos\theta)}{(n-\nu)(n+1+\nu)}$$

$$H_\phi(\omega) = \frac{M_C(\omega)}{4\pi\varepsilon h a c^2}\sum_{n=0}^{\infty}\frac{(2n+1)P_n^1(\cos\theta)}{(n-\nu)(n+1+\nu)} \tag{3.1}$$

where θ is the angular distance from the source to the receivers, ν is the dimensionless complex propagation constant of the radio wave, and M_C is the current moment of the source. The spatial field distributions of the first three SR mode E_r and H_ϕ components, which are derived from FDTD model, are shown in Figure 3.7. In FDTD simulations, "knee" model conductivity profile is employed and the modeling lightning discharge is located at the position where $\theta = 0$. The value of each mode shown in Figure 3.7 is the maximum appearing in the spectrum of

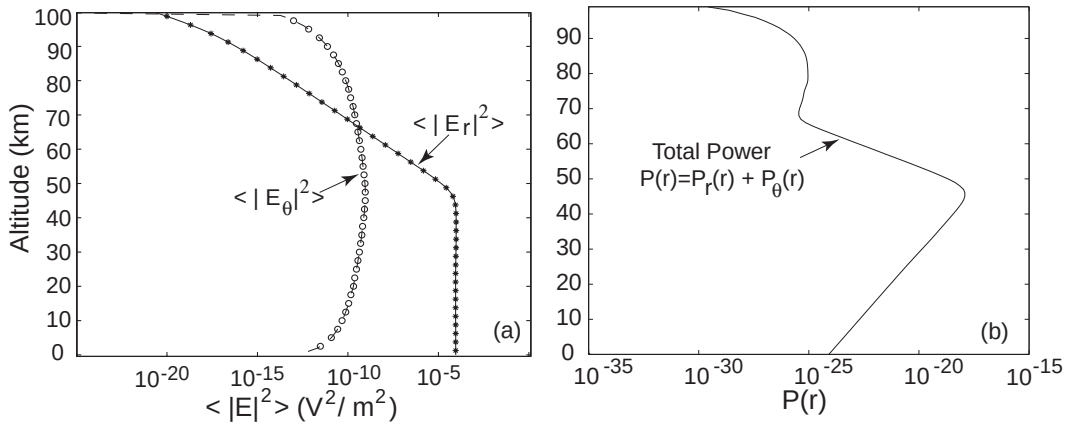

Figure 3.6. (a) The global averages of the E_r and E_θ components between ground and 100 km for the unperturbed single-exponential conductivity profile; (b) The total power dissipation in the cavity.

FDTD results, which is also referred as the peak power of SR modes. The electric and magnetic fields obviously exhibit the Legendre and associated Legendre polynomial distributions consistent with analytical solutions given by equations (3.1). Different penetration heights of E_r and H_ϕ components are clearly observed in Figure 3.7. The E_r component extends with no significant variation up to 50 km, in agreement with the results shown in Figure 3.6(a). However, H_ϕ component can penetrate up to around 90 km.

Results of FDTD modeling using a two-exponential conductivity profile with parameters introduced in Chapter 2 (providing a good agreement with experimental observations of f_n values in a real cavity [*Mushtak and Williams*, 2002]) are shown in Table 3.1 along with the corresponding f_n and Q_n values from Table 4 of [*Mushtak and Williams*, 2002] calculated using a two-exponential model. The results of FDTD model agree with the two-exponential analytical model very well (within 3%) in terms of both f_n and Q_n values. The two-exponential conductivity model leads to a very flat frequency dependence of Q factor, and generally fails to properly reproduce the Q values observed experimentally and obtained for the

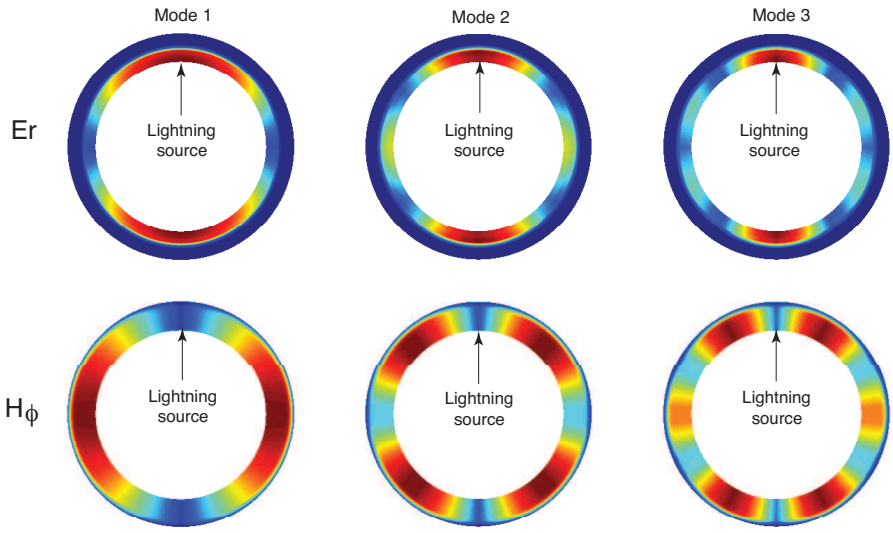

Figure 3.7. The spatial field distributions of E_r and H_ϕ components in Earth-ionosphere cavity with "knee" model derived from FDTD model. The source is located just above the inner surface of the cavity. For illustration purposes, the height and inner radius of the Earth-ionosphere cavity are not shown to scale.

"knee" model (see Table 3.1 and discussion in [*Mushtak and Williams*, 2002]).

Mushtak and Williams [2002] have recently discussed different laterally uniform conductivity models of the Earth-ionosphere cavity and noted that the single-exponential model and the two-exponential model (using the same scale height for both conductivity segments) discussed earlier are not capable of reproducing realistic variation of Q_n values with frequency. This aspect was attributed by *Mushtak and Williams* [2002] to the existence of two distinct altitude layers of energy dissipation within the lower ionosphere and a physical change between the ion-dominated and electron-dominated conductivity as a function of altitude, which has a "knee"-like shape when conductivity is plotted as a function of altitude on a logarithmic scale. *Mushtak and Williams* [2002] argued that the observed increase in Q_n values with frequency can be traced in the case of "knee"-like conductivity to an upward migration of the lower dissipation layer through the

"knee" region leading to decrease in scale height of conductivity and increase in Q_n values. The FDTD results presented in Table 3.1 support ideas of *Mushtak and Williams* [2002] indicating that the "knee" model is indeed capable of simultaneous reproduction of the realistic f_n values and Q_n factors as a function of frequency, and that these parameters can not be reproduced with single scale height models (i.e., single- or two-exponential profiles discussed above). The f_n and Q_n values calculated with FDTD model for the unperturbed single-exponential profile are included in Table 3.1. These values are in good agreement with results of [*Sentman*, 1983]. As expected, the Q-factors remained flat with the frequency. We have performed series of additional numerical experiments in which we varied the scale height of the single-exponential profile. The Q factors increased with the reduction of the scale height, but remained flat as a function of frequency, reaching very high values as system approached the ideal cavity regime.

3.3 Schumann Resonance Frequency Variations During the Solar Proton Events and X-Ray Bursts

In Section 3.2, we discussed the SR problems in a cavity with the uniform conductivity profiles. A good agreement between our FDTD results and the previous studies (shown in Table 3.1) illustrates that our FDTD model provides accurate solutions for SR problems in the Earth-ionosphere cavity.

The SR frequencies are known to undergo daily and seasonal variations of approximately ± 0.5 Hz [*Sátori*, 1996; *Price and Melnikov*, 2004]. Besides these periodic and repeatable variations the SR frequencies can also vary due to rela-

tively transient ionization events in the lower ionosphere. The most pronounced examples of these include Solar Proton Events (SPEs), which can produce ionization in polar cap regions down to 30-40 km altitudes [e.g., *Roldugin et al.*, 2003, and reference therein], and solar X-ray bursts, typically producing an additional ionization at altitudes above 60-70 km, which lasts less than 1 hour, but covers an entire Earth's hemisphere [e.g., *Roldugin et al.*, 2004, and reference therein]. To account for an external conductivity perturbation (e.g., associated with SPEs and X-ray bursts), a single-exponential profile with perturbations at different altitudes (equation (2.17)) are employed in the whole cavity, where $\beta = 3$, $a = 6$ (shown in Figure 3.8 by a solid line). The centers of the perturbation region (z_0) are positioned between 30 km and 80 km altitude with an interval of 5 km (representative profiles are shown in Figure 3.8 by dashed lines). In one specific FDTD simulation, the conductivity perturbation is positioned at a specific altitude (z_0) to calculate the corresponding SR frequency and Q-factor. Open circles in Figure 3.9(a) and 3.9(b) report results on variation of the first mode (n=1) eigenfrequency f_1 and corresponding Q-factor Q_1 as a function of altitude z_0 of the perturbation of the single-exponential conductivity profile. Results obtained by *Sentman* [1983] using mode theory for the same profiles are also shown in Figure 3.9(a) and 3.9(b) by solid lines. The FDTD results corresponding to unperturbed single-exponential profile are shown in both figures by vertical dashed lines (these can be compared to values f_1=7.61 Hz and Q_1=6.11 reported in [*Sentman*, 1983]). The FDTD results appear to be in good agreement with results of *Sentman* [1983]. Figure 3.9(a), in particular, indicates that z_0 values below ∼60 km lead to a depressed eigenfrequency, while those above ∼60 km lead to increase in the frequency. *Sentman* [1983] states: "At low altitudes, the atmosphere is a poor conductor, so increasing the conductivity there increases the dissipation with the consequence of lowering

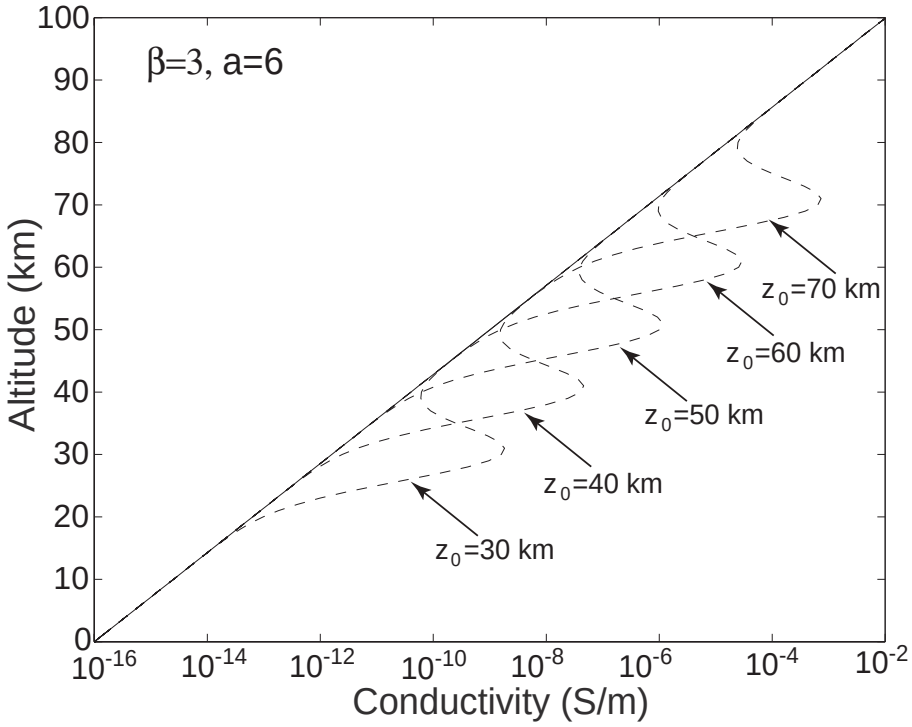

Figure 3.8. The single-exponential conductivity profile with exponential perturbations at different altitudes.

the eigenfrequency of the mode. At high altitudes the atmosphere is already a very good, but not perfect, conductor, so increasing the conductivity there decreases the dissipation by making the ionosphere a more perfect reflecting surface, thereby raising the eigenfrequency". These frequency variation aspects will be further discussed below in this section with relation to recent experiments. In Figure 3.9, the FDTD results are derived from a cavity with the conductivity perturbation in the whole cavity. However, the situations are different during SPEs and X-ray bursts. The ionization in polar cap regions produced by SPEs typically has a spatial extent around polar regions with a 1000 km radius. The additional ionization associated with X-ray bursts usually covers half Earth. As shown in Figure 3.10, to account for the perturbation related to SPEs, the conductivity perturbation is centered at the altitude of $z_0 = 40$ km in the region with a approximate 1000

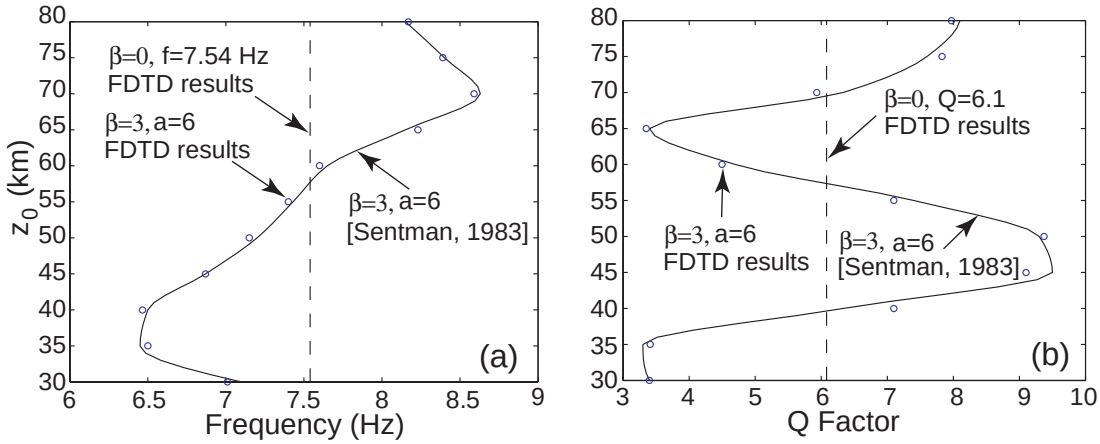

Figure 3.9. The frequency (a) and Q value (b) shifts in a cavity with the conductivity perturbation at different altitude obtained using FDTD model (circles) and from previously reported modeling studies (solid lines) [*Sentman*, 1983]. The vertical dashed lines indicate the frequency and Q-factor derived from a cavity with the unperturbed single-exponential conductivity profile.

km radius around both poles in FDTD simulations. For X-ray bursts, half cavity is covered by the conductivity perturbation at z_0 = 70 km. Figure 3.10 gives a clear picture to show how these perturbations are added in the simulation. The shadow areas stand for the disturbed areas. S is the total area of the Earth's surface, and S_p is the area of the disturbed region. For a regular SPE and X-ray burst, S_p/S is equal to 0.13 and 0.5 [*Yang and Pasko*, 2005], respectively. The corresponding FDTD results are shown by open circles connected by a solid line in Figure 3.11, and the disturbed regions extend from two poles to the equator in this case. The S_p/S=0 (f_1=7.54 Hz) and S_p/S=1 (f_1=6.47 Hz) points can be traced back to Figure 3.9 and correspond to results obtained for uniform cavities with unperturbed and perturbed (z_0=40 km) profiles, respectively. The area S_p of the perturbation corresponding to z_0=70 km is assumed to have similar geometry to the z_0=40 km case, but to grow from the north pole only, with the S_p/S=1, in this case, corresponding to the perturbed area reaching the south pole, and S_p/S=0.5 to a perturbation extending from the north pole to the equatorial plane

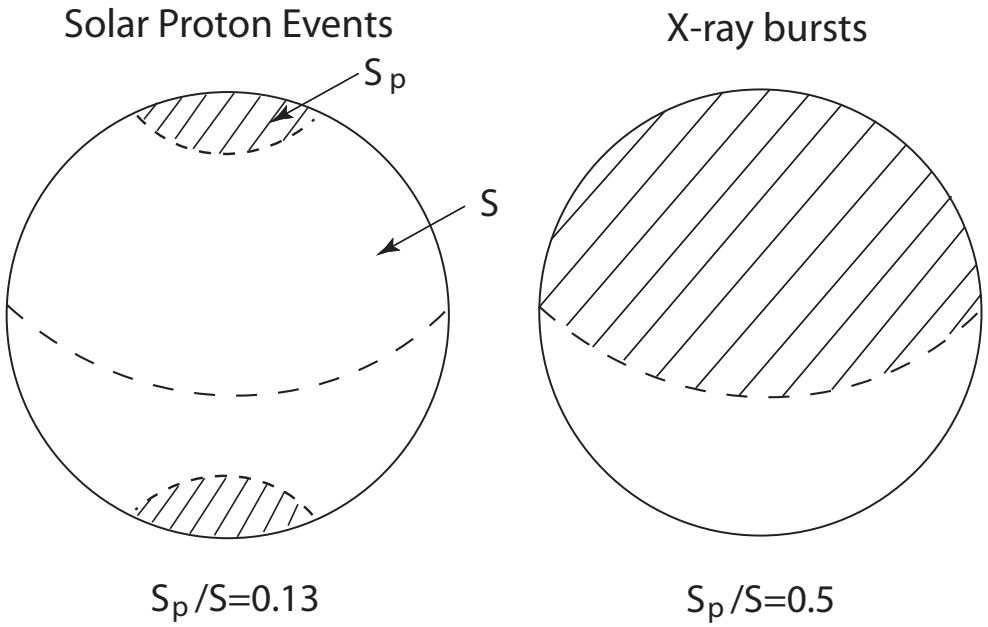

Figure 3.10. The relative disturbed areas during SPEs and X-ray bursts.

and effectively covering half of the Earth surface. The corresponding results are shown by stars connected by a solid line in Figure 3.11. A dash-dot line in Figure 3.11 illustrates a linear approximation, which is commonly employed in the existing literature in order to estimate changes in observed SR frequency f_{obs} using uniform models [e.g., *Schlegel and Fullekrug*, 1999; *Roldugin et al.*, 2001, 2003]: $f_{obs} = f_u(S - S_p)/S + f_p S_p/S$, where f_u and f_p correspond to uniform spherically symmetric cavity solutions with unperturbed and perturbed conductivity profiles, respectively. Results in Figure 3.11 indicate that a factor of 2-3 errors in Δf values are possible due to this approximation for small S_p/S around 0.1 (typically S_p/S=0.13 is used to approximate an area affected by SPEs [*Roldugin et al.*, 2001, 2003]). *Schlegel and Fullekrug* [1999] studied daily averaged values of the first mode SR frequency during nine SPEs and found the frequency increases by 0.04-0.14 Hz, in good correlation with observed integral solar proton fluxes with energies >1 MeV. *Roldugin et al.* [2001, 2003] considered most energetic components

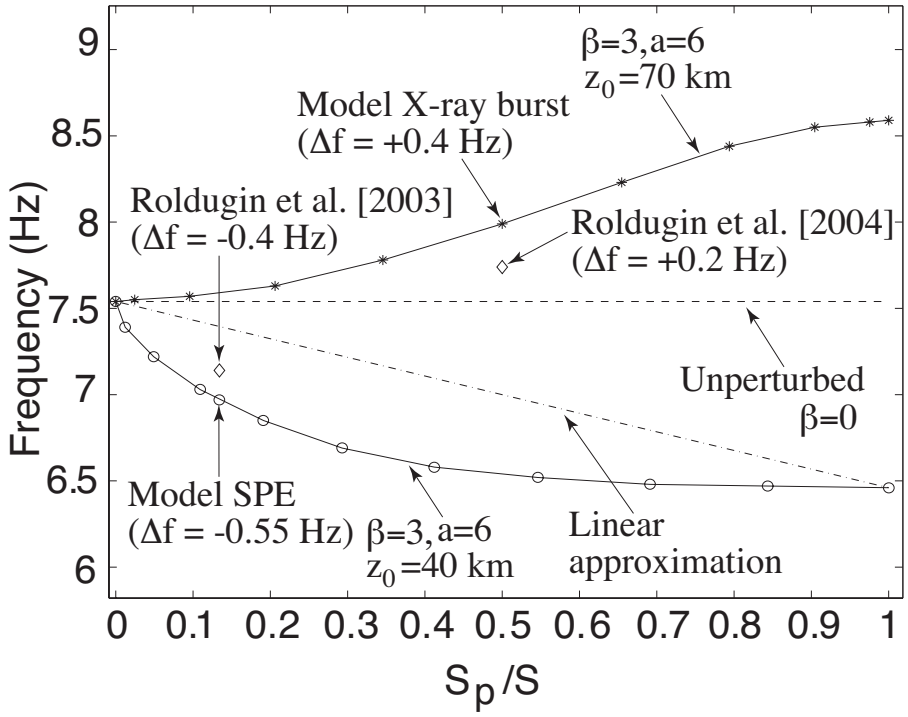

Figure 3.11. The SR frequency variations with the size of the disturbed area during SPEs (circles) and X-ray bursts (stars) obtained using FDTD model.

of SPEs (protons with energies >100 MeV) lasting only several hours and reported the time resolved (the resonance frequency was determined for each of 5 min intervals) decreases of the first mode frequency by ∼0.15-0.4 Hz. Given the fact that solar X-ray bursts typically precede proton precipitation events on the same day and that these two types of phenomena are expected to produce opposite effects on eigenfrequencies (see below), the contradiction between the above two results is likely related to differences in time scales chosen for the analysis [*Roldugin et al.*, 2001, 2003]. In accordance with the arguments of [*Sentman*, 1983] the high energy protons producing conductivity enhancement at altitudes 30-40 km (qualitatively corresponding to profile z_0=40 km in Figure 3.8) are expected to lead to the SR frequency decreases due to the increased dissipation at lower altitudes. Figure 3.11 includes the Δf=-0.4 Hz experimental result at S_p/S=0.13 reported by [*Roldugin*

et al., 2003]. The close agreement between the model and observations for this case is more or less coincidental, given the model nature of the conductivity profiles used, however, the modeling correctly reflects the general trend of reduction of the eigenfrequency due to the ionization at lower altitudes in accordance with the physical arguments discussed above.

Roldugin et al. [2004] reported the first resonance frequency increases by 0.2 Hz (shown in Figure 3.11 at S_p/S=0.5) during some very intense solar X-ray bursts. In accordance with arguments of [*Sentman*, 1983], a conductivity enhancement at altitudes above 60-70 km in association with solar X-ray bursts is expected to lead to an increased eigenfrequency by making the upper boundary in the cavity a better conductor. Results presented in Figure 3.11 for z_0=70 km qualitatively support this argument in agreement with observations of [*Roldugin et al.*, 2004].

3.4 Summary

In this Chapter, we have discussed the validity of our new 3D FDTD model of the Earth-ionosphere cavity. Several classic conductivity models (e.g., two scale-height profile and "knee" model) are applied with our FDTD model. The accurate reproduction of the SR frequencies and Q-factors with these conductivity profiles verifies that the 3D FDTD model provides accurate solutions for the ELF problems in the Earth-ionosphere cavity. Another important problem we have investigated in this Chapter is related to the SR frequency variations associated with different conductivity perturbations in the cavity. The key results can be summarized as follows:

- The conductivity perturbation appearing at the altitude of 30-40 km in the

atmosphere associated with solar proton events (SPEs) increases the total energy dissipation in the cavity and leads to the decrease of SR frequencies.

• The conductivity perturbation appearing at the altitude of 60-70 km in the atmosphere associated with X-ray bursts decreases the total energy dissipation in the cavity and leads to the increase of SR frequencies.

• The FDTD model results are in good agreement with the experimental data reported in [*Roldugin et al.*, 2001, 2003, 2004]. The area of the disturbed region influences the magnitude of the first Schumann resonance frequency shift Δf. The magnitude of the frequency shift increases with the area of the disturbed region, however, the variation is not linear, indicating that the related assumption used in the existing SR literature [e.g., *Roldugin et al.*, 2003, and references therein] is not accurate and may lead to a factor of 2-3 errors in Δf value.

Chapter 4

The Diurnal and Seasonal Variations of Schumann Resonance Parameters

4.1 Introduction

Besides relative transient SR frequency variations associated with disturbed ionosphere during X-ray bursts and SPEs, SR parameters (power, frequency, and Q-factor) have been found to undergo diurnal and seasonal variations. The peak frequencies in both the electric and magnetic Schumann resonance spectra are observed to undergo a diurnal variation of approximately ∼0.5 Hz about their average values of 7.8, 14, 20, ... Hz. *Balser and Wagner* [1962] were the first to measure the diurnal variation of the resonance frequencies. They used 12-minute digitized samples of the vertical electric field taken every 2 hours on 12 days during February 1961 to obtain an estimate of the spectral intensity in the frequency range of the first four modes.

In [*Sentman and Fraser*, 1991], observations are presented of the horizontal magnetic component of Schumann resonance intensities as simultaneously mea-

sured at locations in California and Western Australia during two separate intervals of September 2-17, 1989 and April 14-21, 1990. For both intervals, diurnal variations of the average magnetic power over the lowest three modes of the Schumann resonances showed substantially different temporal profiles at the California and Western Australia stations. It is believed that the SR power variations depends not only on the global lightning activity, but also on the local ionosphere height. When corrected for the local D region height, the detailed diurnal intensity profiles over the analysis intervals display a greatly improved similarity, providing a good method for monitoring the global totality of lightning activity in the Earth-ionosphere cavity. In [*Price and Melnikov*, 2004], the long-term (4 years) diurnal and seasonal variations of different electromagnetic components (E_r, H_{NS}, and H_{EW}) are presented based on measurements at a field site in the Negev desert, Israel. The power variations of the various modes and components show three dominant maxima in the diurnal cycle related to lightning activity in South-East Asia (0800 UT), Africa (1400 UT) and South America (2000 UT).

4.2 SR Parameter Variations Related to Global Lightning Activity

Cloud-to-ground lightning discharges are the principal excitation source of Schumann resonances. The global average lightning discharge rates of 100 s^{-1}, with peak currents on the order of 20,000 to 30,000 A for strokes of average lengths of 3 to 5 km [*Uman*, 1987], are sufficient to excite the Earth-ionosphere cavity to the observed Schumann resonance intensity. The global thunderstorm activity is spatially concentrated over three broad continental tropical regions, (1) the

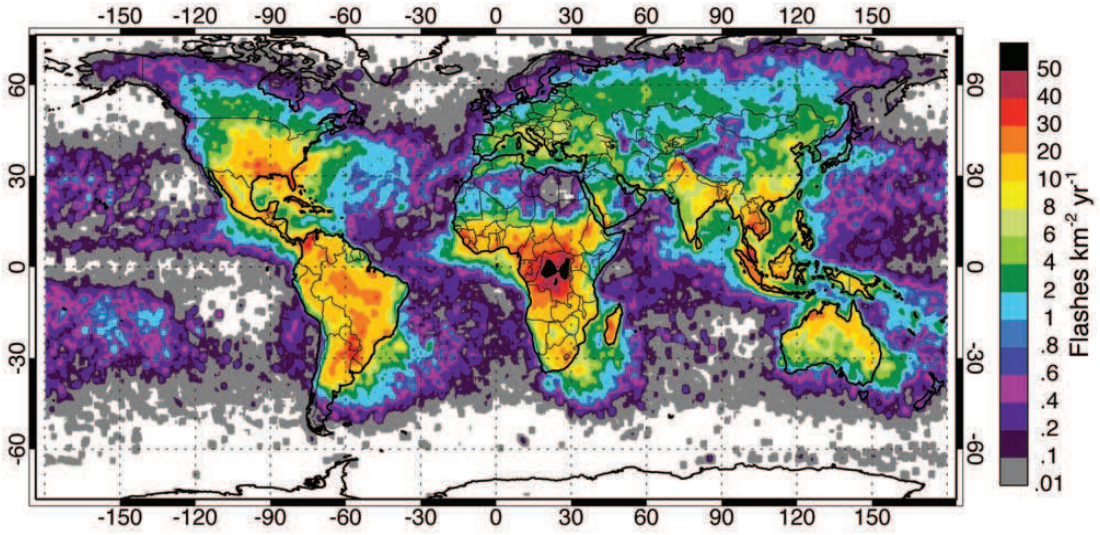

Figure 4.1. Map of the global lightning activity in the Earth-ionosphere cavity detected by Optical Transient Detector (OTD) (figure courtesy of [*Christian et al.*, 2003]).

Malaysian Archipelago and Maritime continent extending from Southeast Asia across the Philippines, Indonesia, and Borneo into Northern Australia; (2) sub-Saharan Africa; and (3) the Americas, principally the Amazon basin in South America, but with substantial contributions from the Central America. Thunderstorm activity tends to maximize in the late afternoon in each of these three regions, at approximately 0800, 1400, and 2200 UT, respectively. Also, the principal peak in the diurnal modulation of Schumann resonances is at approximately 2200 UT, suggesting that the America is the globally dominant lightning region. Lightning over the oceans and in the region outside these three main lightning regions, while occasionally intense locally, is relatively insignificant on a global scale compared to the three major continental thunderstorm centers, suggesting that these related contributions to the excitation of Schumann resonances are relatively minor [*Sentman*, 1995, pp. 268].

Figure 4.1 shows the map illustrating the distribution of the global lightning activity detected by the Optical Transient Detector (OTD), and three main light-

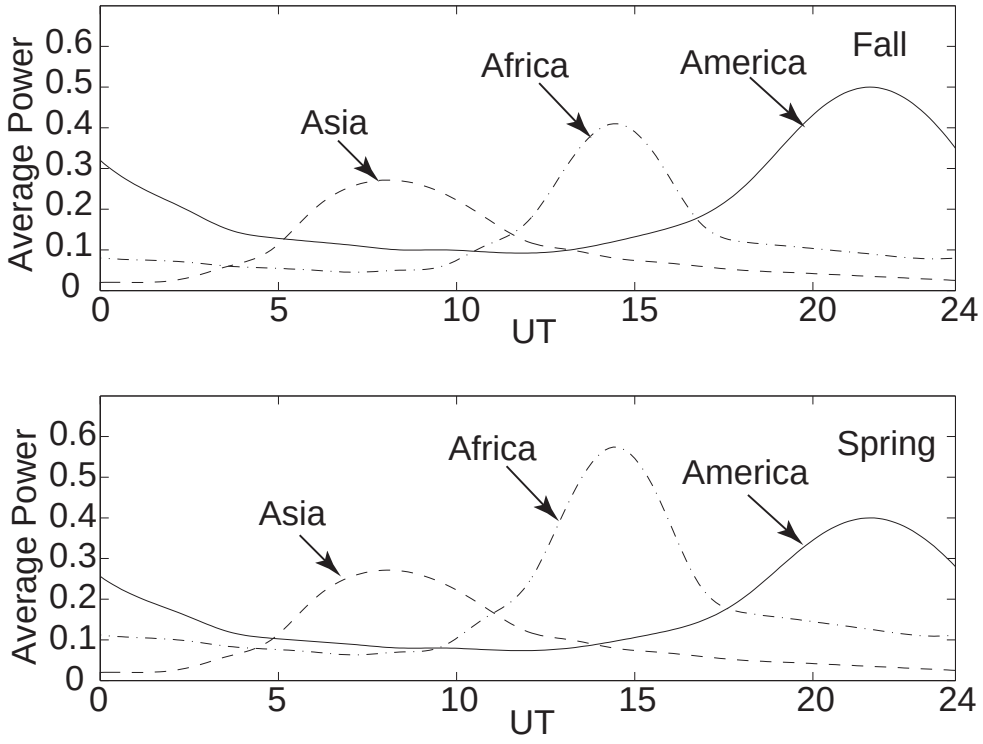

Figure 4.2. The diurnal power variations of the global lightning activity in Southeast Asia, Africa, and America during Fall and Spring seasons reported by *Sentman and Fraser* [1991].

ning centers are clearly shown in this map. The OTD is a space-based optical sensor on an orbit inclined by 70^o with respect to the equator specifically designed to detect and locate lightning discharges as it orbits the Earth. The satellite orbits the Earth once every 100 min and has a 100^o field of view (equivalent to 1300×1300 km^2 area on the ground) [*Christian et al.*, 2003]. The OTD detects lightning flashes during both daytime and nighttime conditions with a detection efficiency ranging from 40% to 65%, depending upon external conditions. Further information can be found at the official OTD Web site, http://thunder.nsstc.nasa.gov/otd/. OTD data are available at no charge at http://ghrc.msfc.nasa.gov/. *Pechony and Price* [2007] processed the 5-year OTD data using a diurnal monthly mean (DMM) technique with hourly time resolution. Since OTD data only provide the density of

lightning flashes, and no information about the type (cloud-to-ground or intra-cloud) and magnitude of lighting, it can not be directly applied to the sources of SR calculations. Figure 4.2 shows the diurnal variation of the relative power of the global lightning activity in the three major lightning regions [*Sentman and Fraser*, 1991], which is used in our FDTD modeling. The total lightning activity in South-East Asia, Africa, and South America reaches maximum at approximately 0800, 1400, and 2200 UT, respectively. Moreover, the maximum magnitude of the lightning activity varies with seasons. In Fall, the lightning activity in the South America is stronger than that in Africa. In Spring, the lightning activity increases by 40% in Africa, and reduces by 20% in South America. The lightning activity in South-East Asia remains approximately the same during these two seasons.

4.2.1 SR Power Variations With Global Lightning Activity

In our simulations, the typical number of FDTD cells in r, θ and ϕ directions are 20, 20 and 40, respectively. The power and frequency of the first SR mode are calculated every 1.2 hour from 0000 UT to 2400 UT. Three simulations are performed at each specific time point. In each simulation, it is assumed that the lightning discharges are uniformly distributed in a rectangular region centered at 27^oE 9^oN, 99^oE 18^oN, and 63^oW 9^oN in Spring months, and at 27^oE 0^oN, 99^oE 0^oN, and 63^oW 0^oN in Fall months, corresponding to the three main lightning regions at Africa, South-East Asia and South America, respectively, and the size of this source region is 3 cells $\times$ 3 cells (i.e., about 3000 km $\times$ 3000 km) [*Yang and Pasko*, 2006]. The magnitude of each source at three major lightning regions was modulated as a function of time to reflect the lightning activity variation shown in Figure 4.1. Since the Earth-ionosphere cavity can be considered as a

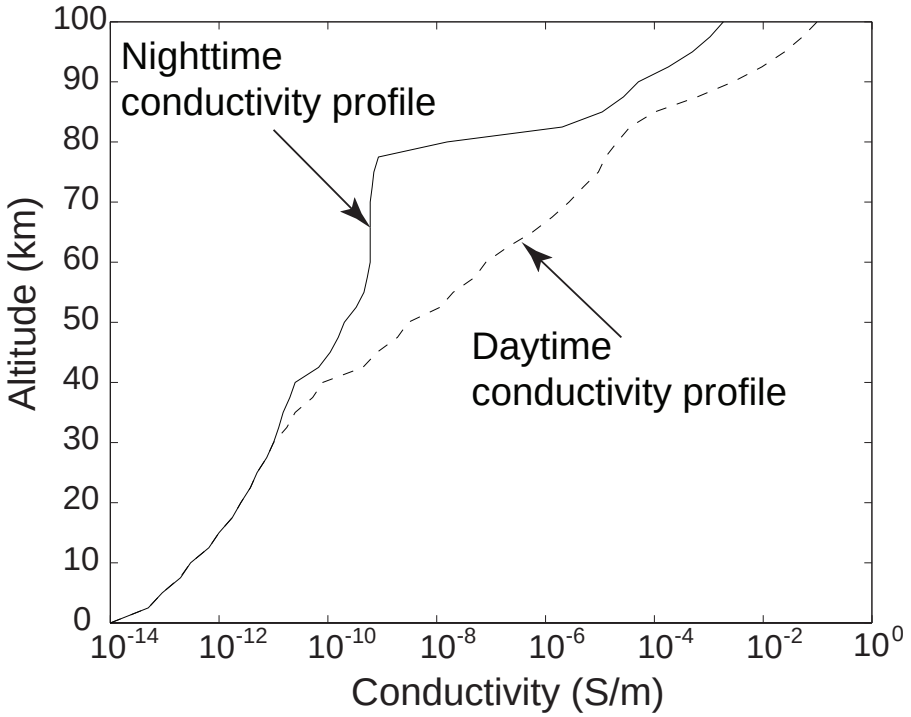

Figure 4.3. The representative conductivity profiles collected at 0000 UT, on September 15, 2000, at 0^oE 0^oN and 180^oE 0^oN, corresponding to the conductivity profiles at nighttime and daytime in Earth-ionosphere cavity, respectively, obtained from IRI model [*Bilitza*, 2001] (above 60 km) and from [*Hale*, 1984; *Huang et al.*, 1999] (below 60 km).

linear system, we can deal with these three sources separately. The total signal used in the final analysis can be expressed by the sum of the waves from these three sources. The modeling receivers are located at $\theta = 63^o$ and $\phi = 36^o$ just above the ground corresponding to the location of the SR field station (35.45^oE, 30.35^oN) near the town of Mitzpe Ramon, in the Negev desert, Israel [*Price and Melnikov*, 2004] and $\theta = 45^o$ and $\phi = 18^o$ just above the ground corresponding to the realistic location of the SR field station (47.6^oN, 16.7^oE) at Nagycenk, [*Sátori and Zieger*, 1999]. The vertical electric field component (E_r) and magnetic components in East-West (H_{EW}) and North-South (H_{NS}) direction are calculated and compared with measurements reported by *Price and Melnikov* [2004]. In each

simulation, the corresponding conductivity profile is derived from International Reference Ionosphere (IRI) model as discussed in Section 2.3.2 at each specific time. Figure 4.3 illustrates two representative night and day time total conductivity profiles collected at 0000 UT, on September 15, 2000, at 0^oE 0^oN and 180^oE 0^oN, respectively.

Figures 4.4 and 4.5 report FDTD results on the power variations of E_r, H_{EW}, and H_{NS} components of the first three SR mode as a function of universal time, as well as the frequency-time spectrogram of these three components corresponding to Fall and Spring seasons, respectively. The variation patterns of the E_r and H_{EW} components have similar shape. The power increases around 0500 UT, and a stronger power peak is found at 1400 UT in both cases. In addition, the peak in Spring at 1400 UT is stronger than that in Fall. For the H_{NS} component, a different variation pattern is observed. The power reaches its peaks around 0800 UT and 2200 UT. The power magnitude at 2200 UT in Spring is weaker than that in Fall, and remains approximately same at 0800 UT. All of these features are in good agreement with the experimental measurements reported by *Price and Melnikov* [2004], as further discussed below.

Price and Melnikov [2004] have recently reported the diurnal and seasonal variations of the frequency and power of the first SR mode. A good agreement is found between our FDTD results and the realistic measurements of the first SR power variation. As shown in Figures 4.4 and 4.5, the power variations of the E_r and H_{EW} have same patterns, which have two peaks at 0500 UT and 1400 UT, respectively. The peak at 0500 UT can be explained by day-night terminator effect. Because the receiver is located at 36.0^oE, 27.0^oN, the sunrise time at that location is approximately at 0400 UT. During sunrise, the ionospheric boundary moves downward due to the solar radiation. Therefore, a corresponding increase

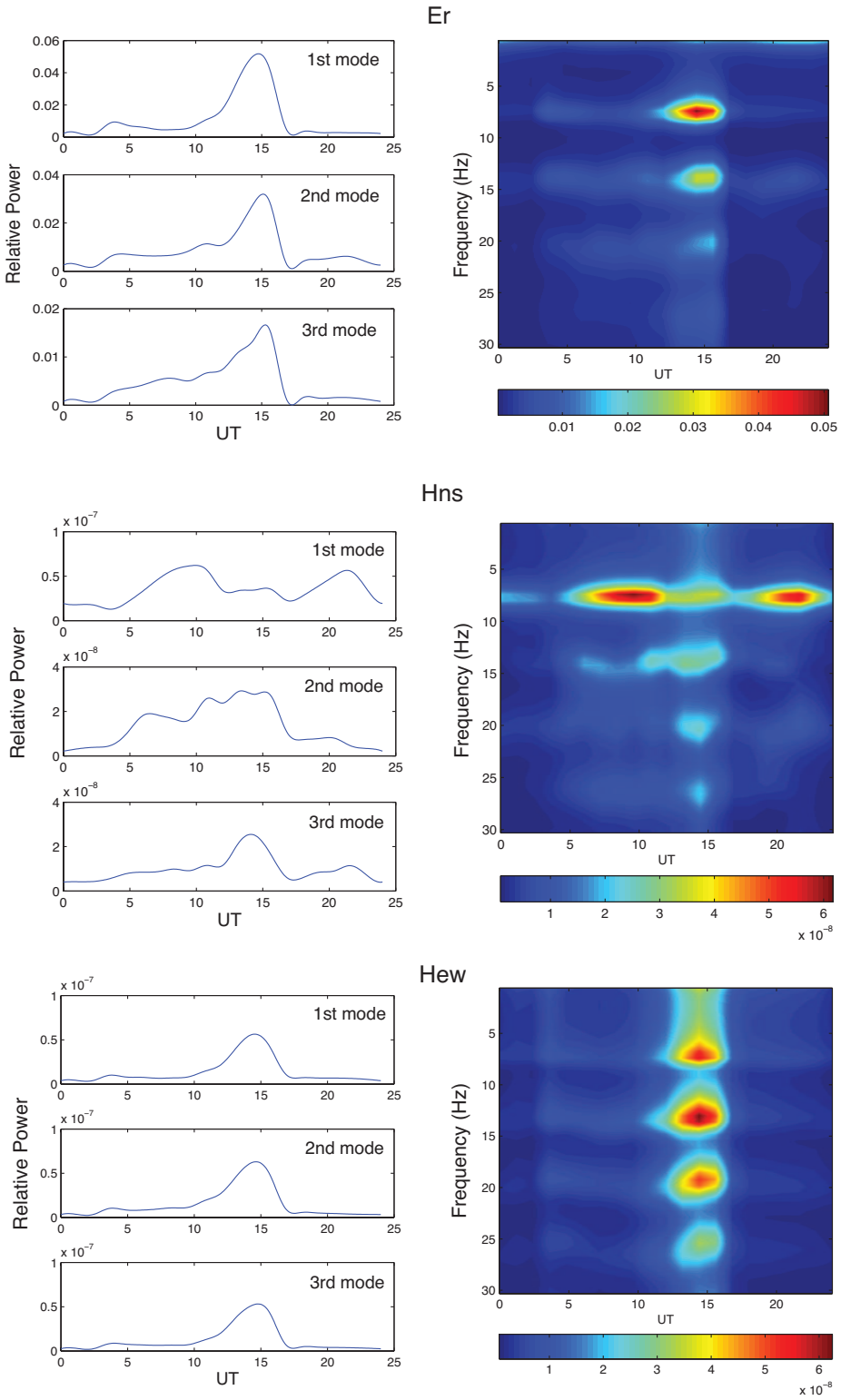

Figure 4.4. The diurnal power variations (left) and the frequency-time spectrogram (right) of the first three SR mode E_r, H_{EW}, and H_{NS} components corresponding to Fall season derived from FDTD model.

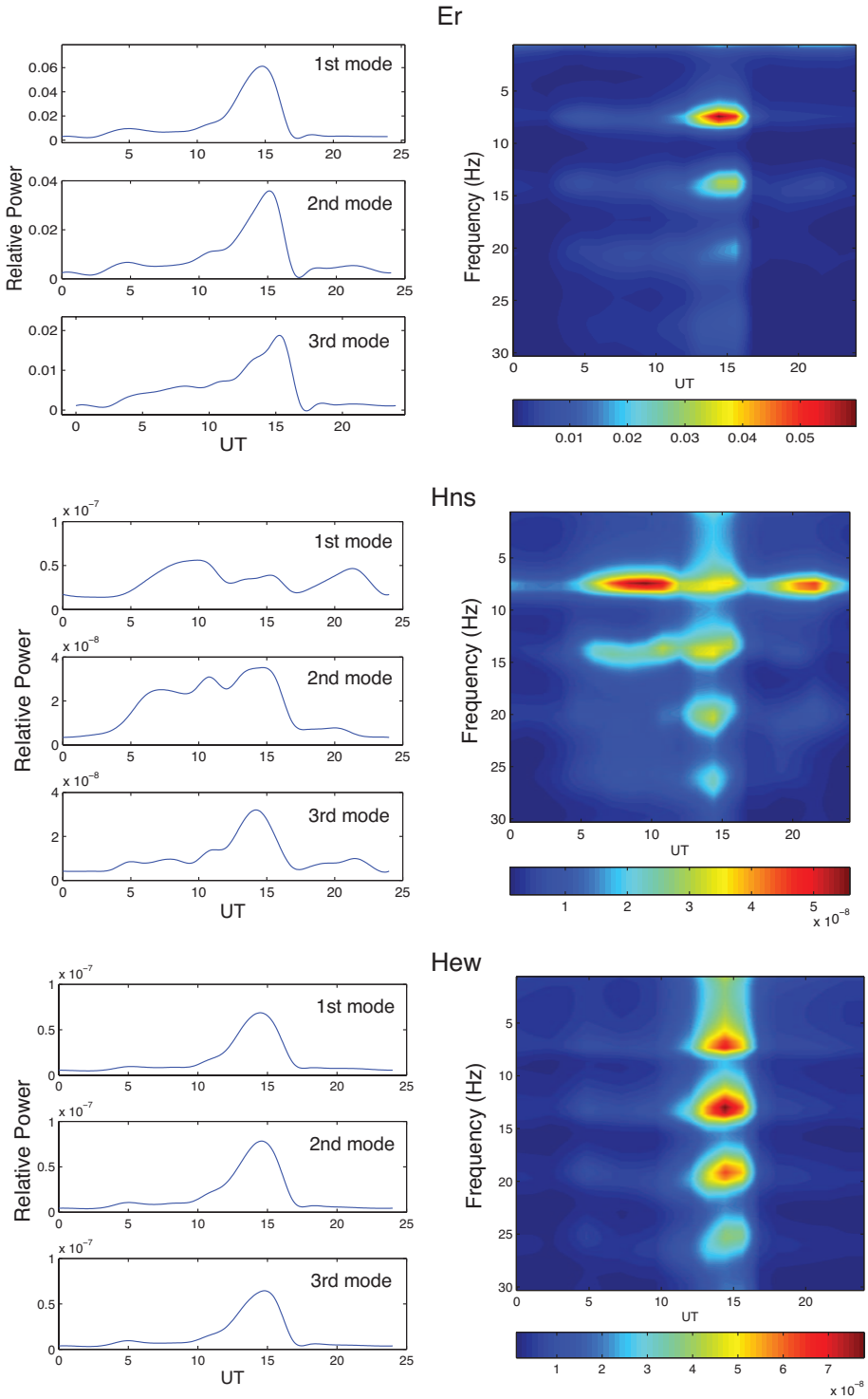

Figure 4.5. The diurnal power variations (left) and the frequency-time spectrogram (right) of the first three SR mode E_r, H_{EW}, and H_{NS} components corresponding to Spring season derived from FDTD model.

in the SR power starting from 0400 UT is observed in Figure 4.4 and reaches its peak at 0500 UT. The second peak in the E_r and H_{EW} components at 1400 UT is much stronger than that at 0500 UT, because the lightning activity in the Africa reaches its maximum around 1400 UT. The power variation in the H_{NS} component undergoes different variation pattern in comparison with other two components (Figures 4.4 and 4.5). Two peaks associated with the lightning activity from South-East Asia and South America are found around 0900 and 2200 UT. The seasonal power variation is also obviously observed in Figure 4.4 and 4.5. It is believed that this seasonal variation is related to the seasonal variation of global lighting activity. In Spring, the lightning activity in Africa is stronger than that in September (see Figure 4.2). Therefore, the corresponding SR power increases in the E_r and H_{EW} components around 1500 UT in Spring are observed. Since the magnitude of the lightning activity in South-East Asia employed in this section remains approximately the same in Spring and Fall, there is no obvious difference in the SR power at 0900 UT in the H_{NS} component for both seasons. The SR power peak at 2200 UT is stronger in Fall due to the stronger lightning activity in America during Fall. In [*Price and Melnikov*, 2004], the magnitude of SR power at 1400 UT in Fall is a little stronger than that in Spring in the E_r component, and remains approximately same in Fall and Spring in H_{EW} components. The two peaks in the H_{NS} component around 0800 and 2000 UT in Fall are stronger than these in Spring.

The differences observed between experimental data and FDTD results may be related to fine details of global lightning activity as a function of time employed in FDTD model. The FDTD results are derived from two profiles of global lightning activity (see Figure 4.2) based on 24-hour averages during April 14-21, 1990 and September 2-17, 1989, respectively [*Sentman and Fraser*, 1991], while the realistic

data [*Price and Melnikov*, 2004] is based on a 4-year measurement (1999-2003). We can imply from the data presented in [*Price and Melnikov*, 2004] that the average magnitude of the lightning activity in Africa from 1999 to 2003 remained approximately the same in Spring and Fall, and in South-East Asia and South America, the magnitude of global lightning in Fall was stronger than that in Spring.

In addition, the relative positions of the three main lightning regions with respect to the receiver also have effects on the power variation in E_r, H_{NS}, and H_{EW} components. The source accounting for the lightning activity in Africa is located at 27^oE, and is very close to the receiver located at 36^oE. Therefore, the H field from Africa collected by the receiver is dominated by the east-west component. Meanwhile, the H fields excited by the lightning at South-East Asia and South America have preferentially the north-south component due to the relative positions of the source with respect to the receiver. Therefore, two peaks are observed at 0800 and 2200 UT in the H_{NS} component corresponding to the lightning activity peaks in these two regions and a peak associated with the lightning activity in Africa is clearly found at 1500 UT in the H_{EW} component. For the first SR mode, a null of E_r component appears at the distance of approximately 10000 km from the source. The sources at South-East Asia and South America are approximately 9000 km and 11000 km away from the receiver. Due to the null proximity, these two sources contribute much less to the E_r component at the receiver than that at Africa, which is only 3000 km from the receiver. Therefore, only the peak around 1500 UT in E_r component is obviously observed.

Melnikov et al. [2004] reported a terminator effect on Schumann resonances. Here, we employ our FDTD model to describe this effect. Twenty simulations have been performed to calculate the variation of the distribution of the magnitude of the E_r component of the first SR mode in the cavity due to the day-night

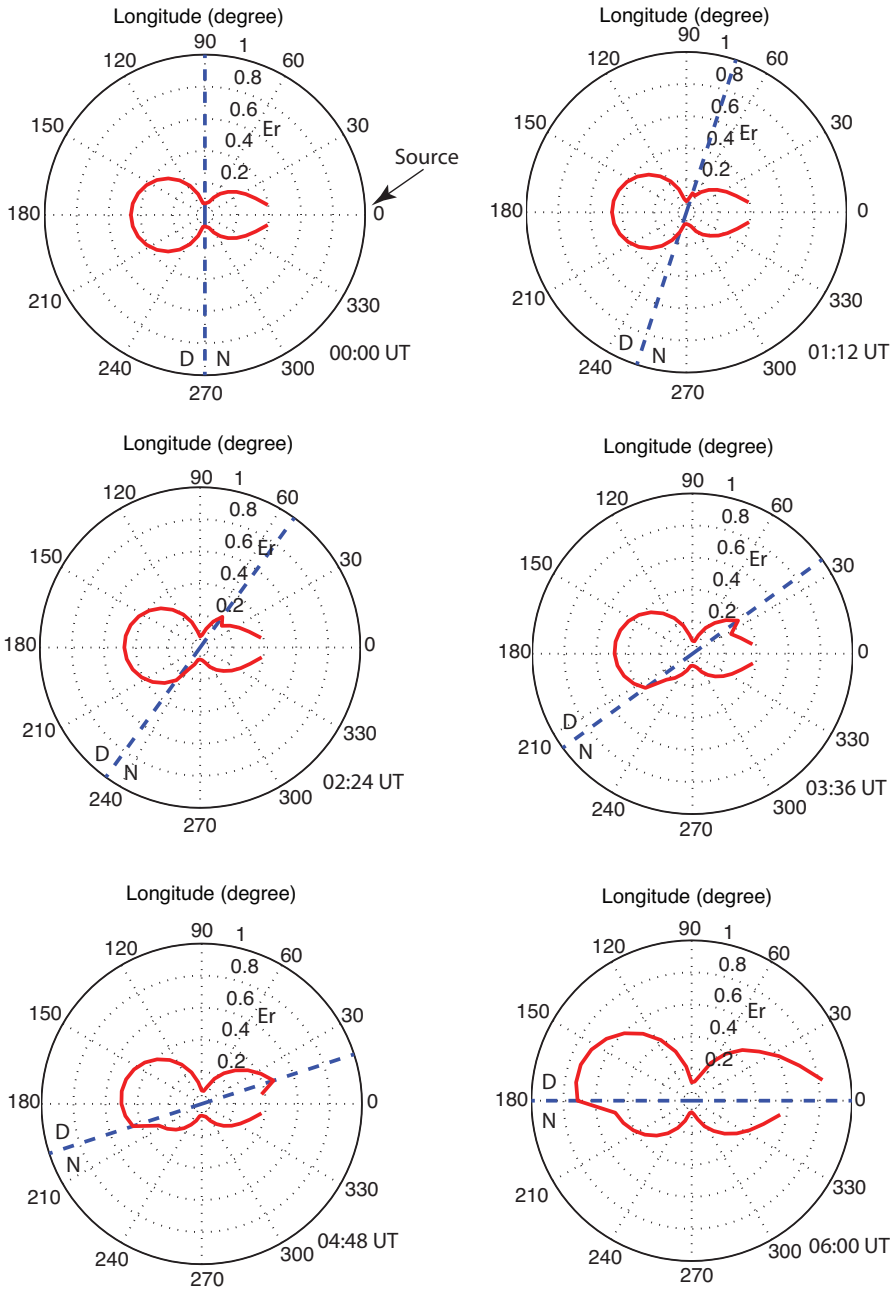

Figure 4.6. The magnitude of the E_r component of the electric field on the surface of the Earth at equator as a function of Longitude. The letters "D" and "N" mark the day and night regions in the Earth-ionosphere cavity, respectively. The six panels correspond to different instants of time during the diurnal cycle between 0000 UT and 0600 UT.

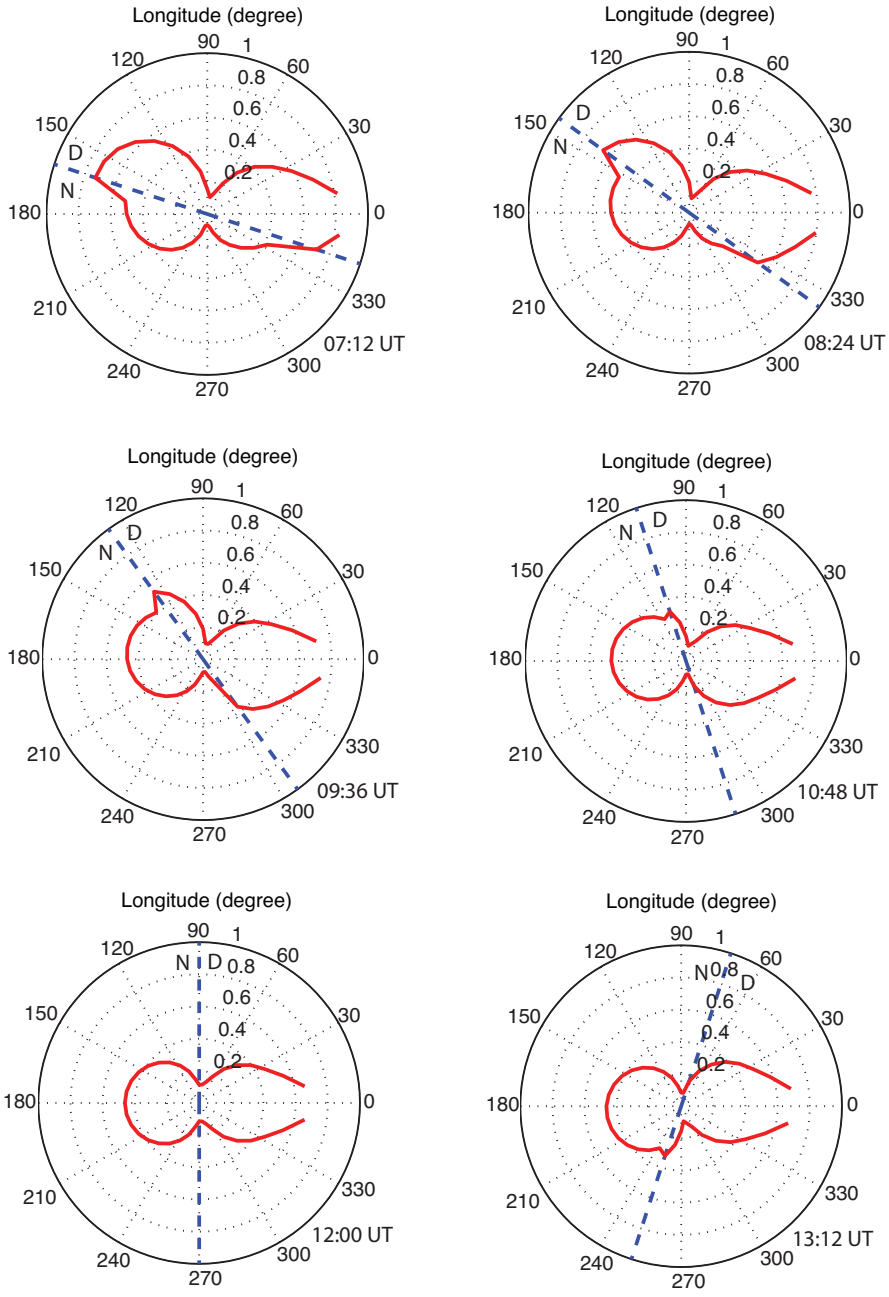

Figure 4.7. The same as Figure 4.6, only for time period 0712 UT to 1312 UT.

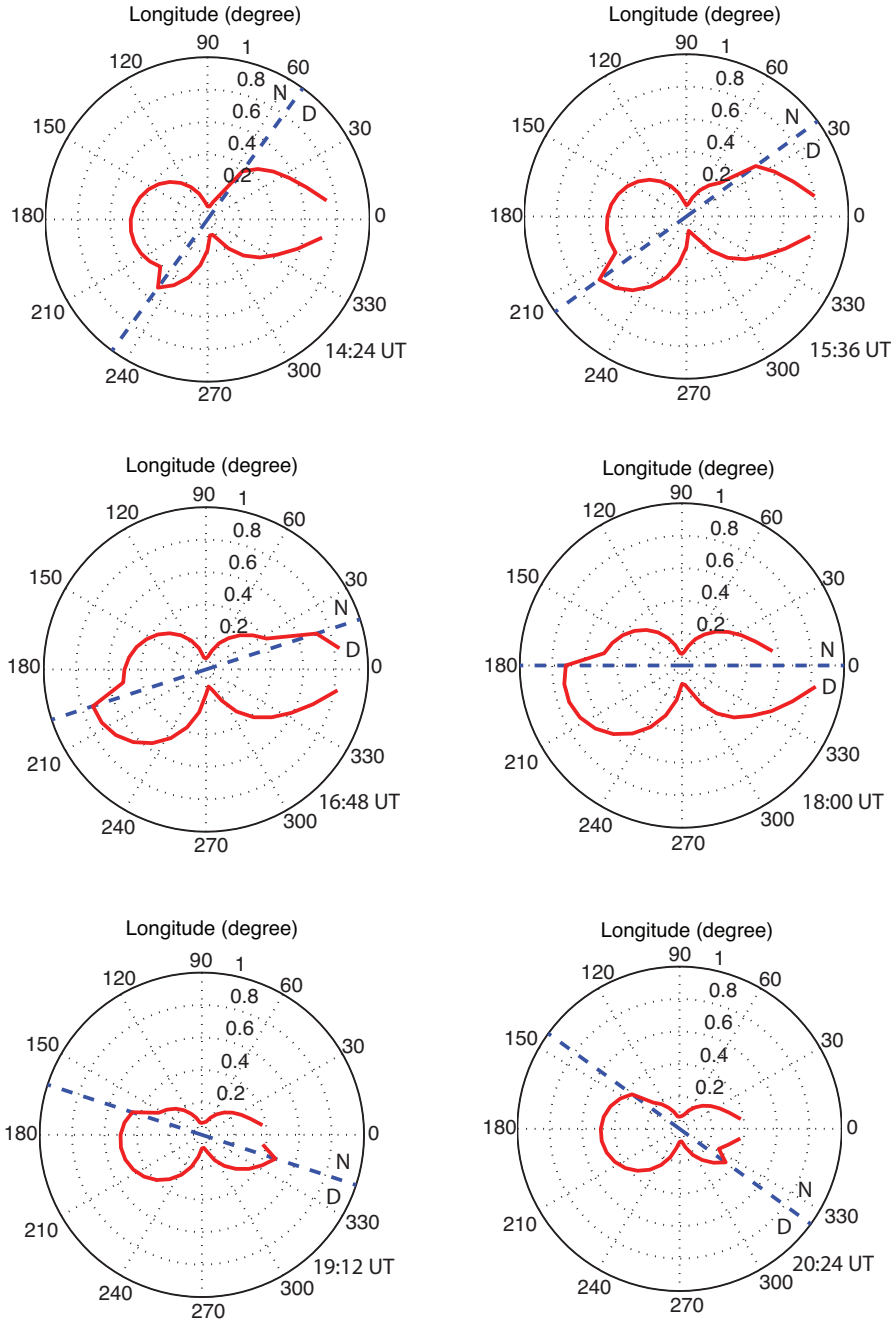

Figure 4.8. The same as Figure 4.6, only for time period 1424 UT to 2024 UT.

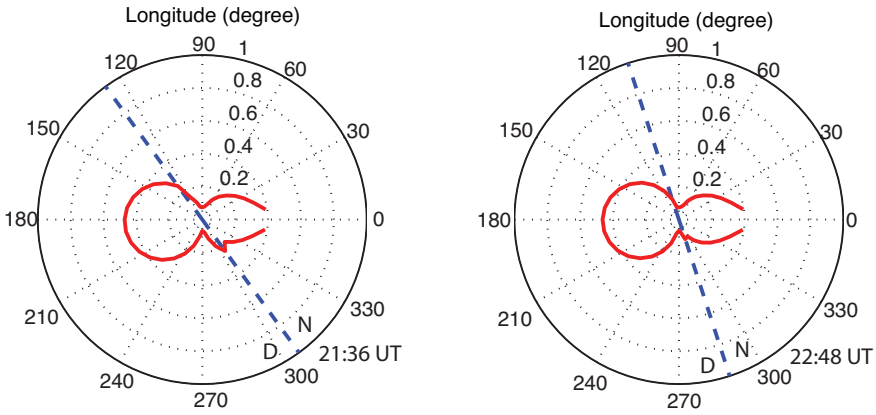

Figure 4.9. The same as Figure 4.6, only for time period 2036 UT to 2248 UT.

terminator position during a diurnal cycle. The conductivity profiles used in these simulations are the same as we used to obtain the results in Fall reported in Figure 4.4. For illustrative purposes, only one source with the same magnitude is used, which is located at 0^oE 0^oN, and 40 receivers are positioned on the Earth surface at equal intervals along the Equator. Figures 4.6-4.9 show the variation of the E_r distribution of the first SR mode during the 0000 UT to 2400 UT time interval. The dashed line depicts the position of the day-night terminator at different instants of time. The letters "D" and "N" in the figures mark the day and night regions, respectively. From these twenty plots, it can be seen that the magnitude of the first SR mode is generally stronger during day-time in comparison with night-time at a fixed position. For example, at longitude 30^o, the magnitude of the E_r component increases during sunrise, and decreases during sunset, which agrees with what has been previously reported by *Melnikov et al.* [2004]. This variation can be associated with the variation of the ionospheric height. The magnitude of the E_r component during day-time is approximately 60% stronger than that during night-time. We also find that the SR magnitude is stronger when the source is near the day-night terminator (see plots corresponding to 0600 UT and 1800 UT) than at other times.

However, in our FDTD model, we find that the power variations of the first SR mode during the sunrise and sunset are much smaller than those associated with the peaks of the global lightning activity (see Figure 4.4). This difference can be explained by the different sources used in these two simulations. In Figure 4.6-4.9, only one source with constant magnitude is employed. In Figure 4.4, many sources with different magnitude are used to account for the diurnal variations of the lightning activity at three lightning centers (as described in Section 4.2), and the results are in good agreement with the realistic measurements [*Price and Melnikov*, 2004]. Therefore, we believe that the global lightning activity plays a more important role in the variations of the SR power.

The effect of the local time in the SR power is well known. According to [*Sentman and Fraser*, 1991; *Melnikov et al.*, 2004], it can be explained by the variation of the altitude of the ionospheric boundary over an observation point due to solar radiation. Meanwhile, the sources of SR, global lightning activity, tending to maximize at specific universal time in three main lightning regions in a diurnal cycle lead to a corresponding intensification of SR power. Therefore, it is believed that the universal time also plays an important role in the variations of SR power. In addition as discussed above, the SR power variations are also influenced by the relative position of the observation point with respect to the main lightning centers, due to the field distribution of SR around the source and the wave orientation.

4.2.2 SR Frequency Variations With Global Lightning Activity

The frequency variations of the three components obtained from the FDTD model during a diurnal cycle are shown in Figures 4.10. The first mode SR frequency in the E_r component has a maximum at 1000 UT and 2200 UT ranging from 7.6 to 7.8 Hz. In the H_{EW} component, the frequency ranges from 7.6 to 7.8 Hz, and two peaks appear around 0300 UT and 1600 UT, both in Fall and Spring. Three peaks can be found in the H_{NS} component around 0800, 1200, and 1600 UT. By comparing with the realistic measurements [*Price and Melnikov*, 2004] shown in Figure 4.11, some similar features are found. For the E_r component, a frequency peak appearing around 1000 UT is close to the FDTD result, which also appears at this time. In addition, the peak around 0300 UT in the H_{NS} also matches the features appearing in the FDTD results. However, we emphasize that the agreement is not as good as in the case of the power variation.

The variation of SR frequencies can be explained by mode splitting theory presented by *Sentman* [1987] due to the asymmetry in the Earth-ionosphere cavity at the day and night sides. The magnitude of the line splitting is in the range of 1.4-1.8 Hz for the cases studied in [*Sentman,* 1987]. Due to the strong damping in the Earth-ionosphere cavity, the magnitude of the mode splitting is less than or comparable to the inherent width of the lines themselves [*Sentman*, 1987], which complicates the determination of the eigenfrequencies of the cavity.

Comparing our FDTD results and data reported by *Price and Melnikov* [2004], some different features are observed in these two frequency variation patterns (see Figures 4.10 and 4.11). One of the reasons for this difference may be related to the fact that the frequency variations are averaged over 3 months in [*Price and*

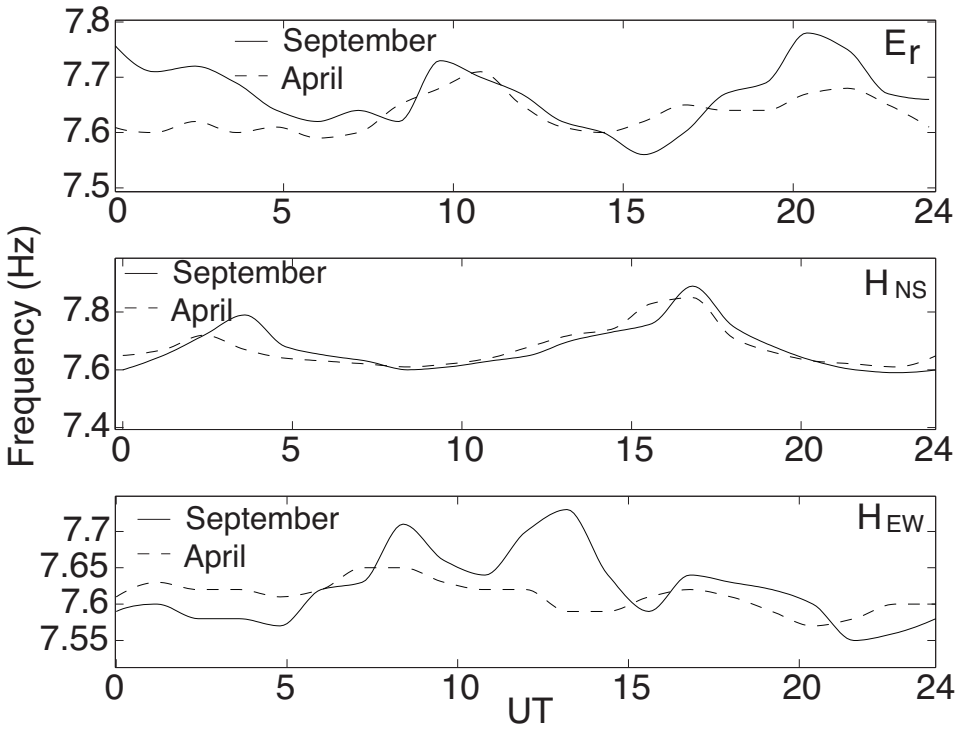

Figure 4.10. The diurnal frequency variations of the E_r, H_{EW}, and H_{NS} components at Fall and Spring obtained using FDTD results.

Melnikov, 2004], while the FDTD results are derived from a model with conductivity profiles corresponding to September 15, 2000 and April 15, 2000. Therefore, the difference between these two results can be expected. Another possible reason for this difference is the different methods employed to find the eigenfrequencies. In [*Price and Melnikov*, 2004], a Lorentzian function fitting method was used to derive the eigenfrequencies of the cavity, assuming that there is only one frequency component in each resonance mode. The Lorentzian fitting method is generally suitable for the application in uniform cavity without mode splitting, and an example is presented in our previous work [*Yang and Pasko*, 2005]. In [*Sentman*, 1987], the maximum magnitude of the first mode splitting is found to be in the range 1.4-1.8 Hz in realistic measurements. If only one frequency component is

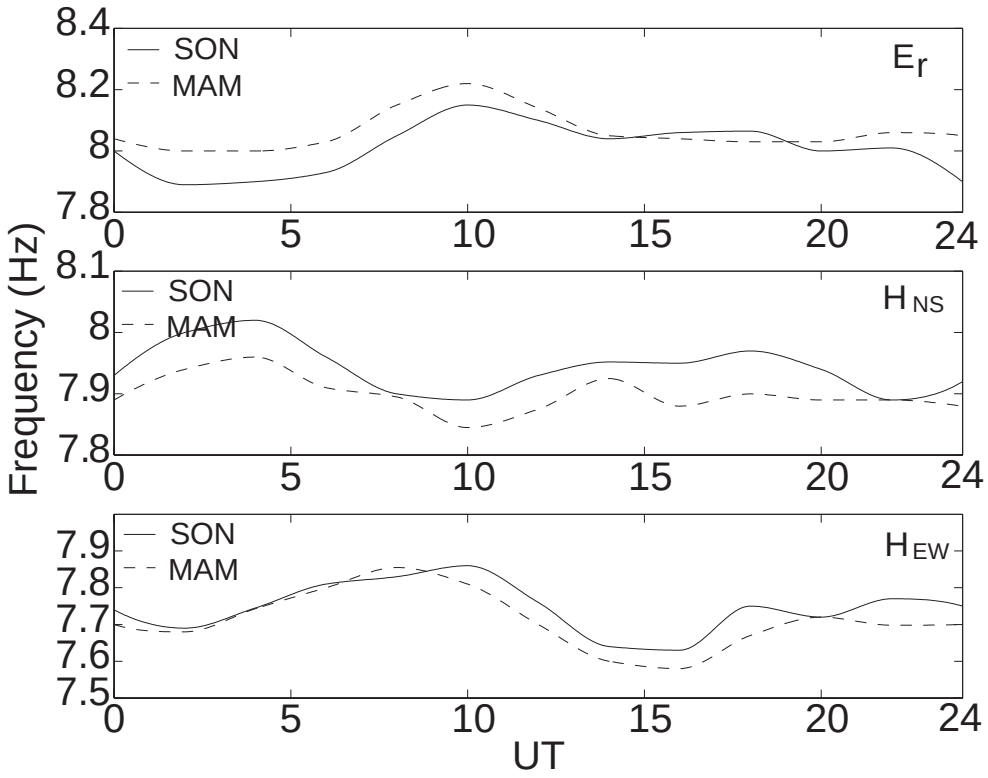

Figure 4.11. The realistic diurnal frequency variations in the E_r, H_{EW}, and H_{NS} components measured by [*Price and Melnikov*, 2004]. The abbreviations SON and MAM in this and subsequent figures and text correspond to periods of time from September to November, and March to May, respectively.

used to fit all of the splitting modes, the result will be influenced by the magnitude of all of the splitting modes, and the maximum error can be half splitting range (0.7-0.9 Hz), which can mask the real variation of the resonance frequency. Therefore, the Lorentzian function fitting method is not applicable for accurate finding method to find the eigenfrequencies of the realistic cavity with mode splitting. In this Chapter, the Prony's method is employed to find the eigenfrequencies of the cavity, by which the mode splitting can be clearly detected. Figure 4.12 shows the comparison of these two methods for analysis of the H_{EW} component derived from the FDTD model with conductivity profile at 0840 UT on September 15, 2000. The result derived from Prony's method matches the original power

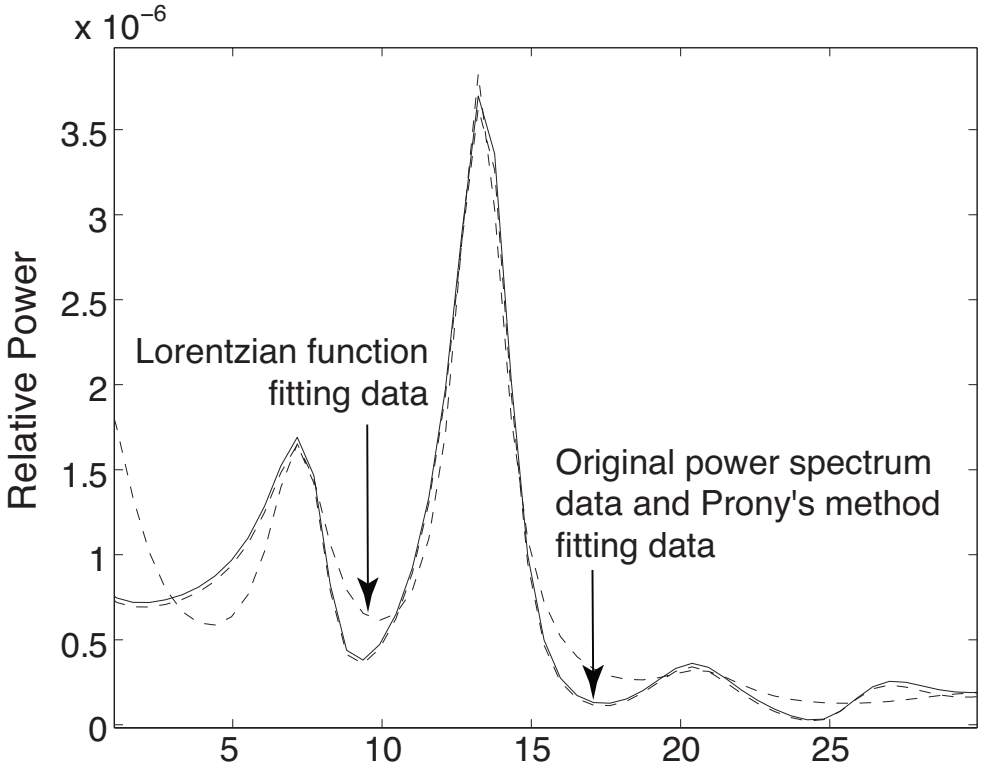

Figure 4.12. Comparison of the fitting curves using the Prony's method and the Lorentzian function fitting method.

spectrum data (solid line in Figure 4.12) much better than that from Lorentzian function fitting method (dashed line in Figure 4.12). By the Lorentzian function fitting method, the first SR frequency is found at 7.45 Hz. By the Prony's method, the first SR mode can be found splitting into 7.7 Hz and 7.59 Hz. Because the magnitude of 7.7 Hz mode is much stronger than that of 7.59 Hz mode, we used 7.7 Hz as the first SR frequency to show results presented in Figure 4.10. A 0.25 Hz difference can be found between these two methods and this difference is close to the magnitude of frequency variations reported by *Price and Melnikov* [2004].

In [*Roldugin et al.*, 2004], it is concluded that diurnal SR frequency variation is mainly controlled by local time, and the different field components undergo different variation patterns due to the horizontal inhomogeneity of the ionosphere.

Nickolaenko et al. [1998] found that the source area of the global lightning activity also plays an important role affecting the SR frequency variation. We conducted additional simulations (not shown), in which we changed the magnitude of the lightning activity at the three lightning centers, as well as the area and positions of these three lightning centers. We observed the obvious changes of the frequency variation pattern. At a specific time, the mode splitting produced by all of the lightning activity in the cavity is determined by the magnitude of each of the lightning discharges, and their positions with respect to the day-night terminator. With changing the area and the positions of these lightning centers, which determine the positions of the lightning discharges in these centers with respect to the day-night terminator, and the magnitude of these lightning centers, the associated change of the mode splitting leading to the SR frequency variation is expected. Therefore, we conclude that the magnitude of the lightning activity in three lightning centers, as well as the area and positions of these three lightning centers are the three main factors controlling the SR frequency variation.

4.3 Summary

The main conclusions of this Chapter can be summarized as follows:

• The FDTD results show a good agreement of the diurnal and seasonal SR power variations with the previous experimental studies [*Price and Melnikov*, 2004]. The power of the first SR mode changes with the local time, the global lightning activity, and the source-receiver geometry.

• The general pattern of the observed SR power variations is controlled primarily

by the variations in the level of lightning activity and the source-receiver geometry, and the height of the ionosphere as a function of the local time plays a secondary role.

• The diurnal frequency variation of the first SR mode is more complicated than the power variation. Some of the features seen in frequency variation derived from our FDTD model agree with the results reported by *Price and Melnikov* [2004], however, the agreement is not as good as in the case of power variation.

Chapter 5

SR Power Variations Related to El Niño and La Niña Phenomena

5.1 Introduction

Recent interest in how global lightning activity might change in the future as a result of global warming [*Williams*, 1992], and how the distribution and intensity of lightning activity changes from year to year as a result of the El Niño and La Niña phenomena [*Goodman et al.*, 2000; *Hamid et al.*, 2001], has led to a renewed interest in the remote sensing application of SR to detect the shifts of the global lightning regions related to the El Niño and La Niña phenomena [*Sátori and Zieger*, 1999]. The power minima of E_r component for the first two modes in 1994 and another one for the first mode in 1997/1998 due to a more southward position of the African thunderstorm region in the El Niño years have been reported in [*Sátori and Zieger*, 1999]. The power maxima are found in the second half of 1996 and 1998 when African thunderstorm region shifts northward in the La Niña years [*Sátori and Zieger*, 1999]. The preserved daily frequency patterns with changing

frequency levels in the same months of the different years imply that the meridional shifts of the lightning activity exist in worldwide sense, and the estimated shifts are about 4-8 degrees in latitude.

In [*Yang and Pasko*, 2006], the diurnal and seasonal variations of SR parameters have been discussed in the context of a 3D FDTD model with an asymmetric conductivity profile. However, the positions of the simulated lightning sources are fixed in these simulations. In this Chapter , the positions of the simulated sources are shifted southward and northward to account for the El Niño and La Niña phenomena, respectively. The associated SR power variations of the electric and magnetic components derived from our FDTD model are compared with previous experimental measurements by *Sátori and Zieger* [1999]. We also present a new method to detect the spatial shifts of the thunderstorm regions using the combination of both electric and magnetic components of Schumann resonances measured at a single station.

5.2 SR Power Variations Related to El Niño and La Niña Phenomena

The FDTD model used in this section is the same as the one applied in section 4.2. The typical number of FDTD cells in r and ϕ directions are 20 and 40, respectively. To describe the slight drift of the lighting center (several degrees), the number of FDTD cells in θ direction is increased to 60. The conductivity is derived from IRI on September 15, 2000. The peak power of the first SR mode is calculated every 1.2 hour from 0000 UT to 2400 UT. In each simulation, we locate the source at 27^oE 0^oS, 99^oE 0^oS, and 63^oW 0^oS, corresponding to the three main lightning regions

at Africa, South-East Asia and South America, respectively, in the case without El Niño and La Niña phenomena. The size of each source region is assumed to be 2000 km× 2000 km with the lightning discharges uniformly distributed in this region [*Yang and Pasko*, 2007]. To account for the influence of the El Niño and La Niña phenomena on the global lightning activity, the simulated lightning source in Africa is moved 3^o southward and northward in the simulations, respectively. A drift of the African thunderstorm region is estimated to be 4^o-8^o in latitude between El Niño and La Niña years [*Sátori and Zieger*, 1999]. [*Nickolaenko and Hayakawa*, 2002] discussed related 10^o shifts of African and American lightning centers. Therefore, the total 6^o shift assumed in our simulations is reasonable for accounting for the movement of the lightning center in Africa related to El Niño and La Niña phenomena.

The magnitude of the lighting activity in three major lightning centers used in this Chapter is shown in Figure 4.2. The total signal used in the final analysis can be expressed by the sum of the waves from these three sources. The modeling receiver is located at $\theta = 45^o$ and $\phi = 18^o$ just above the ground corresponding to the realistic location of the SR field station (47.6^oN, 16.7^oE) at Nagycenk, [*Sátori and Zieger*, 1999]. The vertical electric field component (E_r) and magnetic components in East-West (H_ϕ) direction are calculated and compared with some realistic measurements [*Sátori and Zieger*, 1999; *Price and Melnikov*, 2004].

Figures 5.1-5.3 report the FDTD results on the power variations in the E_r and H_ϕ components of the first three SR modes as a function of the universal time. The three curves in each figure describe the different power variation patterns associated with the different position of the lightning center in Africa during the El Niño, La Niña, and normal years. The African lightning center is located on the equator ($L = 0^o$) in the years without El Niño and La Niña. To account for the El Niño

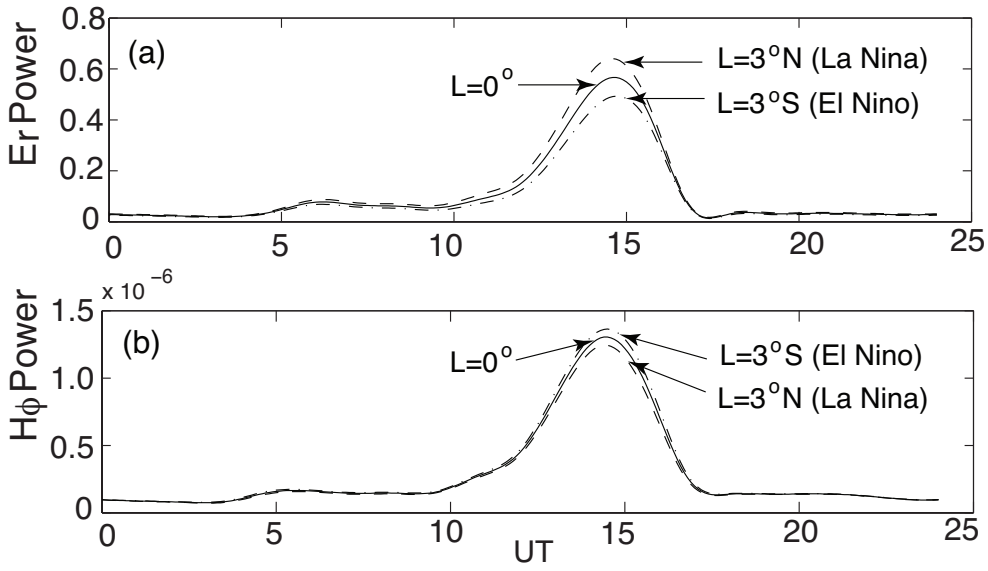

Figure 5.1. The diurnal power variations in the E_r and H_ϕ components of the first SR mode with the shifts of African thunderstorm center associated with El Niño and La Niña phenomena (L indicates the latitude of the lightning center in Africa).

and La Niña, the African lightning center is shifted 3^o southward ($L = 3^oS$) and northward ($L = 3^oN$), respectively. For the first mode, a significant power peak in both E_r and H_ϕ components related to the intensification of lightning activity in Africa is clearly observed around 1400 UT. The peak of E_r component decreases, but the peak of H_ϕ component increases when the lighting center shifts southward from 3^oN to 3^oS. For the second mode shown in Figures 5.2, the power peaks of the E_r component corresponding to the three centers of the lightning activity are found at 1000 UT, 1400 UT, and 2200 UT, respectively. The peak power of the E_r decreases with southward shift of African thunderstorm region from 3^oN to 3^oS. However, no obvious power variation of the H_ϕ component at 1400 UT is observed in Figure 5.2. For the third SR mode shown in Figure 5.3, the power of E_r and H_ϕ at 1400 UT increases and decreases with the southward moving of African lightning activity, respectively. Since we only change the position of the lightning activity in Africa in our FDTD simulations, only the obvious variations

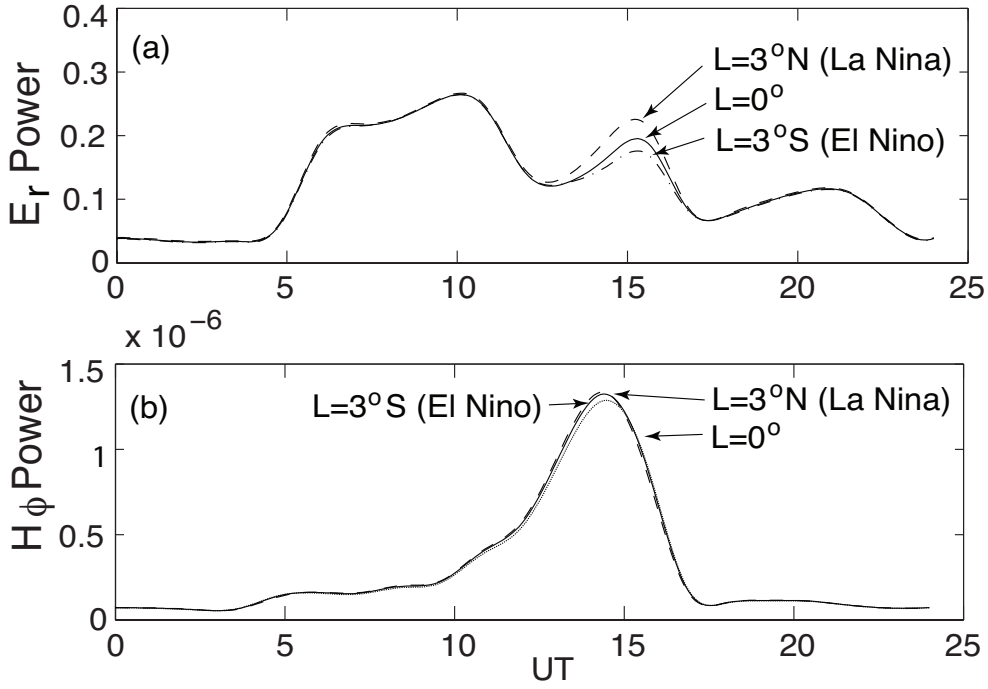

Figure 5.2. The diurnal power variations in the E_r and H_ϕ components of the second SR mode with the shifts of African thunderstorm center associated with El Niño and La Niña phenomena (L indicates the latitude of the lightning center in Africa).

of the SR power near 1400 UT are clearly found, and the power peaks related to the lightning activity at South-East Asia and South America remain constant in these figures.

In Chapter 4, we concluded that the SR power variation not only changes with the local and universal time, but also with the position of the receiver with respect to the lightning centers. The power peak appearing at 0500 UT in Figure 5.1 is related to the descent of the ionosphere due to the sunrise, and the second peak corresponds to the African lightning activity, which reaches the maximum at 1400 UT. Due to the nodal distance of the lightning centers in South-east Asia and South America with respect to the receiver, the lightning activity in these two regions contributes much less than that in Africa in Figure 5.1. Although the distance between the simulated receivers in Hungary (47.6^oN, 16.7^oE) and in Israel

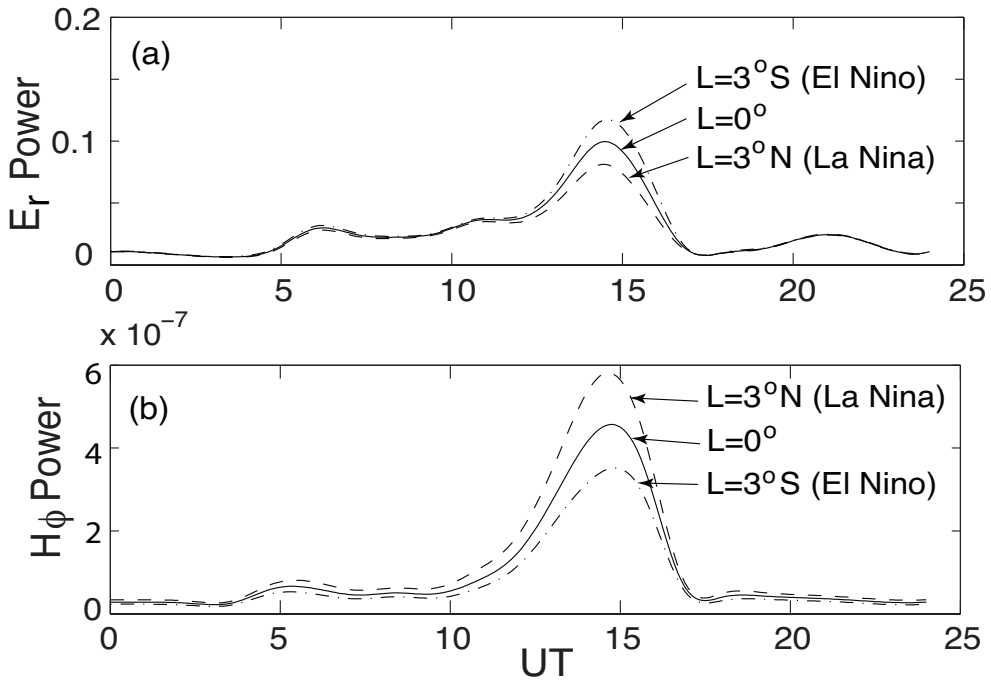

Figure 5.3. The diurnal power variations in the E_r and H_ϕ components of the third SR mode with the shifts of African thunderstorm center associated with El Niño and La Niña phenomena (L indicates the latitude of the lightning center in Africa).

$(35.45^o E,\ 30.35^o N)$ [*Price and Melnikov*, 2004] is approximately 2500 km, for SR waves whose wavelength is comparable with the perimeter of the Earth (40000 km), similar power variations are expected to be detected at these two stations. Comparing our FDTD results with the experimental measurements (Figure 3 in [*Price and Melnikov*, 2004]), a similarity is found of the power variations of the E_r and H_ϕ components of the first three SR modes.

The distributions of the E_r and H_ϕ components follow Legendre ($P_n(\cos\theta)$) and associated Legendre ($P_n^1(\cos\theta)$) polynomials as the function of the angular distance from the source to the receivers (see equation (3.1)) [*Nickolaenko and Hayakawa*, 2002, pp. 105]. Figure 5.4 shows these distribution functions for the first three SR modes (E_r: solid line, H_ϕ dashed line). The simulated lightning source is located at $\theta = 0^o$. For the SR station at Nagycenk, the angular distance

between the station and the lightning on the equator in Africa is about 45^o. Due to the northward and southward shifts of the lightning center, the angular distances are approximately 42^o and 48^o, respectively, in the La Niña and El Niño years. For the first SR mode, when the lightning center in Africa moves from 3^oN to 3^oS, the angular distance increases. In Figure 5.4(a), the magnitude of the E_r and H_ϕ components monotonously increases and decreases, respectively, with the increase of the angular distance, providing straightforward explanation for why the power of the E_r and H_ϕ components undergoes opposite variation patterns shown in Figures 5.1.

For the second SR mode, since the magnitude of the E_r field monotonously decreases with increasing the angular distance (Figure 5.4(b)) around $\theta = 45^o$, a decrease of the E_r field magnitude around 1400 UT is obviously observed during the southward shift of the center of African lightning center (Figure 5.2). There is a magnitude maximum of the H_ϕ component found at the position where $\theta = 45^o$ in Figure 5.2(b), so the magnitude of H_ϕ almost remains constant around $\theta = 45^o$. Since the H_ϕ component is not sensitive to the shift of African lightning activity, we conclude that the second SR mode is not suitable to detect the motion of African lightning centers in this case.

For the third SR mode, the E_r and H_ϕ power obviously increases and decreases with the southward shifts of African thunderstorm regions (shown in Figure 5.3), respectively. All these features are in a good agreement with the specific electric and magnetic field distributions shown in Figure 5.4(c).

Several techniques utilizing the modal distribution of SR electric and magnetic components have been applied in past studies to locate the lightning activity [*Polk*, 1969; *Jones and Kemp*, 1970] and SR parameters (e.g., power and frequency) can be effectively employed to study the shifts of the thunderstorm regions related

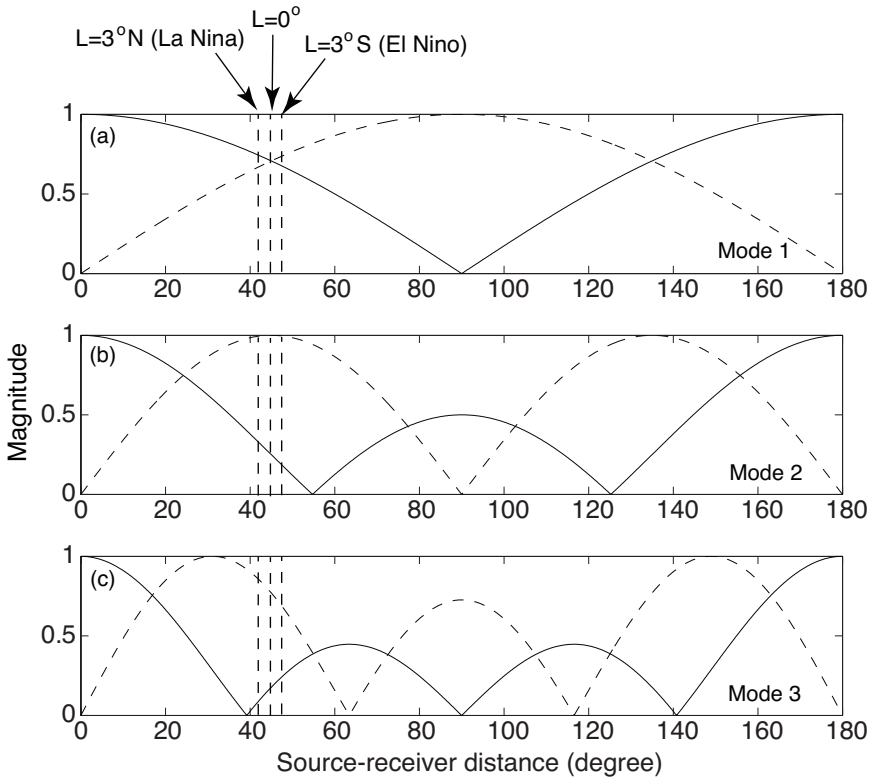

Figure 5.4. The distribution functions of the first three SR modes in the Earth ionosphere cavity (solid lines: E_r component, dashed lines: H_ϕ component). The 0^o corresponds to the position of the source. Three vertical lines indicate the source-receiver distances between African lightning center and Nagycenk station in normal, El Niño and La Niña years.

to El Niño and La Niña phenomena [*Sátori and Zieger*, 1999; *Nickolaenko and Hayakawa*, 2002, pp. 264]. A power minima of E_r component for the first two modes in 1994 and other minima for the first mode in 1997/1998 due to a more southward position of the African thunderstorm region were reported by *Sátori and Zieger* [1999]. A power maxima of the first SR mode was detected in the second half of 1996 and 1998 when African thunderstorm region shifts northward [*Sátori and Zieger*, 1999]. All these features can be identified in our FDTD results shown in Figures 4.14 and 4.15.

The intensity of the global lightning activity and the angular distance between

the sources and receivers are two important factors to determine the magnitude of SR. The E_r and H_ϕ components both become stronger with the increase of the global lightning activity. However, the effects of the shift of the lightning centers on electric and magnetic fields are different due to the different spatial field distributions of these components. For the first SR mode, the magnitude of the E_r component decreases with θ for $\theta < 90^o$, but increases for $\theta > 90^o$, and the H_ϕ component has an opposite variation tendency (shown in Figure 4.17(a)). Therefore, in practice it is difficult to determine which factor (i.e., lightning intensity or angular distance) is the dominant reason to affect the SR power by considering only one field component (E_r or H_ϕ). For example, an increase of the magnitude of first SR E_r component may be equally well produced by the increasing lightning activity or by the shift of the lightning center closer to the receivers as $\theta < 90^o$. By using both electric and magnetic components, the problem can be easily solved. The same power variation tendency of the E_r and H_ϕ components of the first SR mode would indicate that the variation of the intensity of lightning activity is the dominant factor to effect the SR power. The different power variations of the first SR mode electric and magnetic components would show that the shift of the lightning center contributes more to the SR power variations, and the direction of the shift depends on the variation of both electric and magnetic components and the angular distance between the lightning center and the receivers. For the SR stations which are located in Europe [*Sátori and Zieger*, 1999; *Price and Melnikov*, 2004; *Ondrášková et al.*, 2007], the angular distance to African thunderstorm center is within the range of $0^o < \theta < 90^o$. For the first SR mode, we predict that the intensity increase of the E_r component and the intensity decrease of the H_ϕ component would indicate that African thunderstorm center moves northward and therefore closer to these stations under La Niña conditions. The exactly opposite

trend should be observed when the African thunderstorm center shifts southward under El Niño conditions. Using the same methodology, the SR data measured at the station located at Rhode Island (USA) [*Williams and Sátori*, 2004] can be employed to remotely sense the thunderstorm activity in South America under El Niño and La Niña conditions.

For the higher order modes shown in Figures 5.2 and 5.3, the field distributions are complicated, with the appearance of more maximum and null points. The field intensity does not change significantly with several degree variation of the source distance around these maximum or null points (e.g., Figure 5.2(b)). Therefore, the first SR mode is a better candidate for detecting the El Niño and La Niña effects than other modes. In the realistic SR measurements, the experimental data is combined with all kind of external factors, such as diurnal and seasonal power variations, and the power variation associated with El Niño and La Niña phenomena. Since the time period of the El Niño and La Niña phenomena is much longer than the diurnal and seasonal cycles, the SR power variation associated with El Niño and La Niña phenomena can be clearly observed by averaging a long-term measurement data.

5.3 Summary

The main conclusions of this Chapter can be summarized as follows:

• The latitudinal shift of the global lightning activity center associated with El Niño and La Niña phenomena is an important effect leading to the SR power variations. The effects of this shift on the SR power variations of the electric and magnetic components are different from those produced by the intensity variation

of the global lightning activity.

• Due to the simplicity of the field distribution in the Earth-ionosphere cavity for the first SR mode, the combination of the electric and magnetic components of the first SR mode is a good tool to detect the power variations of the lightning activity and its spatial shift associated with the El Niño and La Niña phenomena.

• The same variation tendency of the first SR electric and magnetic components indicates that the lightning activity dominates the SR power variation. The different variation tendency of the first SR electric and magnetic components shows that the dominant effect leading to these power variations is the spatial shift of the thunderstorm regions. The direction of the shift depends on the spatial model structure of the electric and magnetic components and the angular distance between the thunderstorm region and the observation positions.

Chapter 6

Schumann Resonance Parameters on Other Celestial Bodies in the Solar System

6.1 Introduction

In recent years, there has been an increasing interest in exploration of other planets of the Solar System. Lightning discharges play an important role in the chemistry, energetics and dynamics of planetary atmospheres. Apart from the Earth, they have been detected on other planets either by direct imaging of the optical emissions from flashes emanating through the atmosphere or else by picking-up electromagnetic signals such as sferics or whistlers guided by the planet's magnetosphere (see extensive review by *Desch et al.* [2002]). There are two important factors to facilitate the existence of Schumann resonance on a planet. One is that the planet surface and the ionosphere should have high enough conductivity to reflect the electromagnetic waves and form a planetary resonant cavity for

the propagation of the electromagnetic waves. The other important factor is the existence of electrical discharges in the planetary resonant cavity, which can be considered as the sources of the electromagnetic waves to excite the planetary cavity. If SR were detected, they would provide a good support for the existence of the electrical discharges in the lower atmosphere on these celestial bodies, and the SR parameters are also useful in the study of the electromagnetic properties of their lower ionosphere. Recently, a number of papers have been published to discuss the SR problems on other celestial bodies in the Solar System [*Nickolaenko and Rabinowicz*, 1982; *Sentman*, 1990b; *Morente et al.*, 2003; *Pechony and Price*, 2004; *Molina-Cuberos et al.*, 2004; *Yang and Pasko*, 2006; *Navarro et al.*, 2007].

6.1.1 Mars

The radius of Mars is a=3393 km. According to equation (1.1), the first SR resonant frequency for the ideal Mars-ionosphere cavity is therefore approximately 20 Hz. The resonance frequencies are generally reduced if conduction losses in the cavity are accounted for [e.g., *Yang and Pasko*, 2005]. Calculated using our FDTD model [*Yang and Pasko*, 2005], the conductivity in Martian ionosphere needed to reflect ELF electromagnetic waves and to form the upper boundary for the planetary resonant cavity is about 10^{-3} to 10^{-1} S/m. *Cummer and Farrell* [1999] presented the profiles of the electron collision frequency and the electron density corresponding to the daytime and nighttime conditions on Mars. The conductivity derived from these profiles using well established techniques described in [*Yang et al.*, 2006] fully satisfy the condition of existence of the upper boundary of the Mars-ionosphere cavity at altitude ∼120 km under both day and night conditions.

In contrast to Earth, Mars has a very weak global magnetic field. The obser-

vations from Mars Global Surveyor (MGS) indicate existence of large scale weak magnetic field ($\leq$ 5 nT) below Martian ionosphere ($\sim$170-200 km), with localized regions of strong crustal magnetic field [*Acuña et al.*, 2001]. One of the significant observations of MGS electron reflectometer [*Mitchell et al.*, 2001, 2007; *Lillis et al.*, 2004] is the discovery of the unexpectedly strong crustal magnetic field. More frequent and intense magnetic sources were detected at the south hemisphere, particularly in the range of 120^oW-210^oW and 30^oS-85^oS, where fields were detected as large as $\sim$1600 nT [*Acuña et al.*, 1998, 1999; *Connerney et al.*, 1999, 2001, 2004]. The ionospheric variations associated with this strong crustal magnetic field has been reported in several previously published papers [*Krymskii et al.*, 2004; *Withers and Mendillo*, 2005; *Duru et al.*, 2006]. *Withers and Mendillo* [2005] found a significant change over vertical distances (1-2 km) of the electron density profiles preferentially located above crustal magnetic anomalies. High energy particles in solar wind are captured by the open vertical crustal magnetic field lines, and lead to heating of the bottom of the ionosphere in localized regions, especially in the southern hemisphere [*Duru et al.*, 2006]. An average displacement of Martian ionosphere surrounding the strong crustal anomalies is detected to be as much as 19 km according to the data from the MARSIS instrument on the Mars Express spacecraft [*Duru et al.*, 2006]. Furthermore, the strong localized crustal magnetic fields also affect the motion of electrons in Martian ionosphere, particularly at high altitudes where the electron-neutral collision frequency is small, leading to an anisotropic conductivity at these altitudes. Therefore, although the weak global magnetic field can be ignored, the strong localized crustal magnetic field plays a very important role in determining the electromagnetic properties in Martian ionosphere.

The electromagnetic properties of the Martian ionosphere have been discussed

in many previous publications [*Zhang et al.*, 1990; *Bougher et al.*, 2001, 2004; *Gurnett et al.*, 2005]. Like on Earth, Martian ionosphere also changes under influence of external factors. A sudden enhancement of the Martian ionosphere during solar flares has been reported in [*Mendillo et al.*, 2003, 2006]. The electron density in the Martian ionosphere changes with the solar flux due to solar rotation [*Withers and Mendillo*, 2005]. A north-south asymmetry in the Martian ionosphere is discussed in [*Zou et al.*, 2005], and is believed to be the result of the seasonal variation of the neutral Martian atmosphere. Due to the sensitivity of SR parameters to the conductivity distribution in the planetary resonant cavity, it is believed that SR parameters in the Martian-ionosphere cavity change with the solar activity, and with the diurnal and seasonal variations of the Martian ionosphere.

The position of another boundary of the planetary cavity, the ground boundary, depends on the conductivity of the planet's surface. On the Earth, the conductivity of the planet's surface ranges from 10^{-4} to 4 S/m, which can be regarded as a good conductor to terminate the cavity for ELF waves. However, Martian crust does not hold a conductivity like Earth until the depth of 40-60 km [*Grimm*, 2001]. It means that the low-conductivity upper Martian crust will be much less efficient as a reflecting boundary for ELF waves than the surface of the Earth, and the ELF waves can penetrate deeper into Martian crust than Earth shield and suffer more attenuation during their propagation. *Cummer and Farrell* [1999] presented calculations of attenuation of VLF and ELF waves propagating between ground and ionosphere on Mars. The results presented in [*Cummer and Farrell*, 1999] demonstrate a clear dependence of the attenuation on the ground conductivity. This dependence makes us believe that the SR parameters are also strongly determined by the conductivity distribution in the Martian crust. To derive SR parameters accurately, the low-conductivity Martian crust should be included in

our FDTD modeling.

Another important reason to study Martian crust using electromagnetic remote sensing techniques is related to a long standing question about presence of water on this planet. Although subsurface sounding radars mounted on Mars Express probed Martian subsurface to ∼1 km depth [*Picardi et al.*, 2005], ELF and VLF electromagnetic waves are believed to be a better candidate to identify and characterize groundwater on Mars [*Grimm*, 2001], since low frequency electromagnetic waves penetrate more deeply and are less affected by small-scale heterogeneity than sounding radar. Furthermore, the propagation of ELF and VLF waves minimally depends on ionospheric perturbations compared to higher frequency waves. The sounding studies of Earth's crust using ELF and VLF radio installation have been reported in [*Velikhov et al.*, 1998; *Bashkuev and Khaptanov*, 1999] based on the magnetotelluric method developed by *Cagniard* [1953], in which the ground impedance was calculated by using the horizontal components of the electric and magnetic fields. The methods of locating major oil deposits on the Earth by a novel ELF radar have been recently discussed in [*Simpson and Taflove*, 2006a, b, 2007].

The other important factor, which facilitates Schumann resonances on a planet, is the existence of electrical discharges in the planetary resonant cavity, which can be considered as sources of the electromagnetic waves to excite the planetary cavity. The Schumann resonances in the Earth-ionosphere cavity are produced by the global lighting activity. Although there has been no report of orbiter or lander optical images of lightning-like discharges, the charge separation and lightning strokes are considered possible in the Martian dust storms [*Farrell et al.*, 1999]. Terrestrial dust devils are known to be electrically active [*Farrell et al.*, 2004]. Theoretical investigations [*Farrell et al.*, 1999, 2006; *Zhai et al.*, 2006] and experimental studies [*Eden and Vonnegut*, 1973] of dust grain electrification show that

	Mars Dust Devil			Earth	
	Intense	Modest	Weak	Thunderstorm	Dust Devil
Density, e/cm^3	200	20	2	10^3	10^6
Radius (km)	5	3	2	2.8	0.011
Height (km)	10	7	5	5	0.1
Q_{dc} (C)	25	0.6	0.02	20	5e-3
M (kC m)	251	4.4	0.1	100	5e-4

Table 6.1. Some parameters of the electrical discharges on Mars and Earth [*Farrell et al.*, 1999].

electrical discharges can be generated in Martian dust storms. We note that the scale of the discharges produced by the dust storms on the Earth is much smaller than that produced by thunderstorms. Therefore dust storms make very little contribution to the Schumann resonances and always neglected in studies of Schumann resonances on the Earth. Table 6.1 lists some parameters of the electrical discharges on Mars and Earth taken from [*Farrell et al.*, 1999]. The size of the storm is described by its radius and height (shown on second and third lines in Table 6.1). Q_{dc} indicates the total charges in the cloud or dust storm, and M is the charge moment of the storm, which is defined as a product of the charge and the height of the storm. The dust devil on the Earth has much smaller size and charge moment than the thunderstorm. Most parameters are less than 1% of those of the thunderstorm. Martian dust devils are much larger in cross-sectional area than their 10-100 m terrestrial counterparts. Martian dust devils can reach heights of nearly 6 km and have widths of the order of many tens of kilometers [*Farrell et al.*, 1999]. As Table 6.1 shows, the sizes of the modest and weak dust devils on Mars are close to the terrestrial thunderstorms, but the total charges and charge moments are relatively small, when compared to a typical thunderstorm on the Earth. For the intense Martian dust devils, all the parameters are larger than those of Earth thunderstorms, which means it is very possible for these intense events to

have enough energy to produce strong electrical discharges and excite the planetary resonances in the Mars-ionosphere cavity, similarly to lightning discharges in the Earth-ionosphere cavity.

The hydromagnetic waves are generated by interactions between solar wind and ionosphere on the outer boundary of the magnetosphere on the Earth. Related ELF and VLF waves propagate through the ionosphere and are detected on the surface of the Earth [*Hultqvist*, 1966]. An analytical model has been developed to investigate the propagation parameters of hydromagnetic waves through the ionosphere [*Abbas*, 1968]. A day to day variability of the magnitude of the first SR mode was reported by *Füllekrug and Fraser-Smith* [1996], revealing a possible connection between SR power variation and magnetospheric sources originated from the interaction between solar activity and magnetosphere. Although Martian global magnetic field is weak, the "mini-magnetospheres" associated with crustal magnetization on Mars [e.g., *Withers and Mendillo*, 2005; *Withers et al.*, 2005; *Gurnett et al.*, 2005], discussed above in this section, may represent additional effective means to excite the global resonances in Martian cavity.

Overall, the ELF signals due to sources outlined above are expected to be more easily detectable on Mars than on the Earth, which has very high global lighting discharge rate resulting in relatively high background electromagnetic noise levels.

6.1.2 Titan

Titan is Saturn's largest moon. Its radius is approximately 2575 km, which exceeds the radius of the Mercury. Titan is also the largest moon in the Solar System possessing a very substantial atmosphere, with a surface pressure of 1.6 bars (similar to Earth), and a temperature of 95 K [*Desch et al.*, 2002]. On Jan-

uary 14, 2005, Huygens probe landed on Titan, and started the exploration of this largest moon of Saturn. One of multiple missions of Huygens probe was to detect if there were electrical discharges in the Titan's atmosphere [*Grard et al.*, 1995; *Fulchignoni et al.*, 2005]. Although no obvious signatures of lightning have been detected during a relatively short (∼2.5 hours) descent of Hugens probe, several electromagnetic pulses which are similar to terrestrial sferics have been reported [*Fulchignoni et al.*, 2005]. Titan is considered to harbor lightning activity. The possibility of lightning on Titan is supported by theoretical models and observations of Titan's troposphere [*Desch et al.*, 2002, and references cited therein]. The methane droplets in Titan's clouds may suddenly condense and undergo vertical motions, which probably play a role similar to that of water in thunderstorms on Earth. *Tokano et al.* [2005] have proposed that clouds on Titan can rapidly attach free electrons and become negatively charged. A temporary maximum electric field of -2.5×10^6 V/m can be produced by the negative cloud charges, which would be sufficient to cause lightning in Titan's lower troposphere. The negative cloud-to-ground strokes of the lightning would likely be about 20 km long [*Tokano et al.*, 2005].

Several conductivity profiles for the Titan's ionosphere have been discussed in [*Morente et al.*, 2003; *Nickolaenko et al.*, 2003; *Molina-Cuberos et al.*, 2004], in which the conductivity reaches 10^{-2} S/m at the altitude of roughly 500 km. Since the first SR frequency on Titan derived from equation (1.1) is 26.2 Hz, and the realistic one is expected to be less than that due to the conduction loss in Titan's atmosphere, there are grounds to believe that the conductivity of Titan's atmosphere is high enough to create a planetary resonant cavity for the propagation of electromagnetic waves. The SR problems on Titan have been discussed in [*Morente et al.*, 2003; *Nickolaenko et al.*, 2003; *Pechony and Price*, 2004; *Yang et al.*, 2006;

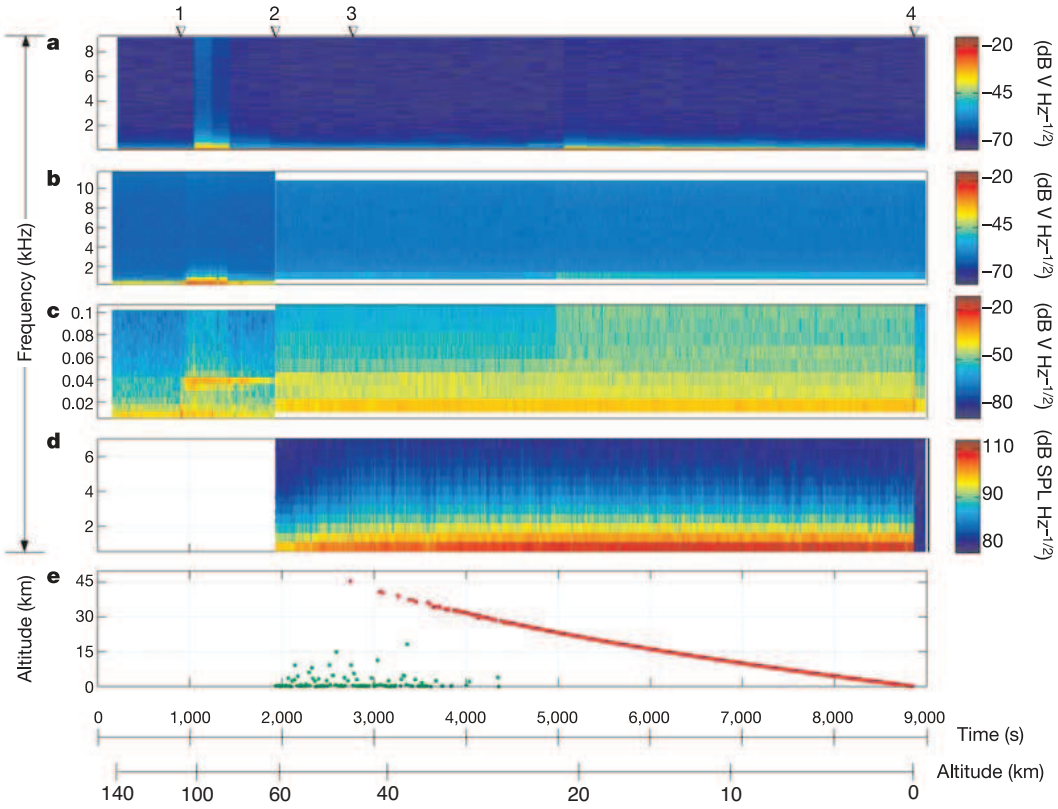

Figure 6.1. A synopsis of the electromagnetic field data detected by Huygens Atmospheric Structure Instrument (figure courtesy of [*Fulchignoni et al.*, 2005]).

Navarro et al., 2007]. The first SR frequency calculated using models discussed in these papers ranges from 11 Hz to 19 Hz due to the different conductivity profiles these models employed. We note that the conductivity profiles used in the above mentioned studies are simplified since they neglect presence of aerosols in the Titan's atmosphere. The attachment of the ions and electrons to the aerosols in the Titan's atmosphere leads to reduction in conductivity below 400 km [*Borucki et al.*, 1987] to values substantially lower than those calculated without including the aerosols [*Morente et al.*, 2003; *Molina-Cuberos et al.*, 2004]. The modification on the conductivity due to the aerosols must lead to changes in SR parameters.

During the descent of Huygens prober in Titan's atmosphere, Huygens Atmospheric Structure Instrument (HASI) provided a unique opportunity to investigate

in *situ* lightning and related phenomena (for example, corona discharges) on Titan that would produce electromagnetic waves, excite global and local resonance phenomena in the planetary resonant cavity. Several impulsive events have been observed during the descent. The narrow-band wave emission seen near 36 Hz appearing between 100 and 60 km during the descent is reminiscent of a possible resonance generated by lightning activity in the spherical waveguide formed by the surface of Titan and the inner boundary of its ionosphere, but should be interpreted with caution (shown in Figure 6.1(c)) [*Fulchignoni et al.*, 2005].

6.1.3 Venus

The speculations that lightning occurs on Venus can be traced back to about 30 years ago. The lightning activity on Venus has been deduced based on the VLF emissions detected by the Soviet landers Venera 11 and 12 [*Ksanfomaliti*, 1980]. However, the data from top-side observations by various spacecraft have not shown un-equivocal optical or electromagnetic signatures of lightning [*Russell*, 1993; *Gurnett et al.*, 2001]. Since there is no constant magnetic field on Venus, the electromagnetic power can not be guided through the bulk of ionosphere outside the global electromagnetic cavity, which may be the reason why such signals could not be detected outside the atmosphere of Venus. Probably, the same result could be expected on Titan having no constant magnetic field *A. Nickolaenko,* private communication, 2006].

The SR problems on Venus were first solved by [*Nickolaenko and Rabinowicz*, 1982]. The lower ionospheric conductivity was approximated by a two-scale-height profile, and the obtained first SR frequency and Q-factor were 9.0 Hz and 5.1, respectively. *Borucki et al.* [1982] predicted Venusian lower ionospheric conductivity

profile below 80 km. The maximum value of this profile is 10^{-10} S/m, which is not high enough to create a planetary resonant cavity. To form the Venus-ionosphere cavity for the propagation of the ELF waves, *Pechony and Price* [2004] extend this profile to high altitude by a "double-knee" model. At the altitude of about 120 km, the conductivity reaches roughly 10^{-2} S/m. The first SR frequency derived using this "double-knee" model is 9.0 Hz, which is close to the value calculated by *Nickolaenko and Rabinowicz* [1982]. However, the Q-factor is 10.5, two times of the previous result [*Nickolaenko and Rabinowicz*, 1982].

6.1.4 Potential Applications of Schumann Resonances on the Celestial Bodies.

In the previous sections, we discussed the possibility of the existence of Schumann resonances on several celestial bodies. In this section, we will discuss some potential practical applications of SR on these celestial bodies.

The previous theoretical [*Yang and Pasko*, 2005] and experimental [*Price and Melnikov*, 2004] studies of SR problems in the Earth-ionosphere cavity show a clear connection between the SR power variation and the lighting activity at three major regions (South-East Asia, Africa, and South America). SR power also undergoes a seasonal change due to the seasonal variation of the global lightning activity in the Earth-ionosphere cavity. This link between SR and global lightning represents a powerful diagnostic tool for studies of global lightning activity in the Earth-ionosphere cavity.

On Mars, the same approach can be used to remotely sense the electrical discharges in the atmosphere. For example, the possible maker of the electrical discharges on Mars, the dust storm, can cover a large fraction of the planet. The

dust storms start as a series of small isolated cores with diameters less than 500 km, but over 10-20 days these cores can enlarge to encircle the entire planet, and then persist for another 50-100 days. The favored locations for development of the bright cores are the elevated plateaus in the mid-southern latitudes. These storms also recur seasonally, appearing just prior to summer solstice [e.g., *Farrell et al.*, 1999], and references cited therein]. Such a strong variation in the magnitude and size of the Martian dust storm during its development would certainly lead to the variations in SR parameters.

Since SR parameters are also strongly determined by the electromagnetic properties of the planetary resonant cavity, which undergo diurnal and seasonal variations, and also affected by the short-term perturbations associated with solar activity, the monitoring of these resonances can be used to extract information about global state of the Martian lower ionosphere. The solutions of similar inverse problems with applications to the Earth-ionosphere cavity have been reported in [*Cummer*, 2000; *Price and Melnikov*, 2004].

As was already emphasized in Section 5.11, the conductivity distribution of Martian crust from ground surface to the depth of 40-60 km is also an important factor determining the SR parameters on this planet. The ELF measurements might provide a feasible method to remotely sense the Martian subsurface conductivity profile to depths of 40-60 km. Magnetotelluric method in ELF and VLF band developed by *Cagniard* [1953] is a feasible tool for location of anomalous conductivity structures in the Martian crust, such as mineral deposits and underground water or ice, using natural or artificial ELF sources.

The ELF waves generated by charged particles spiraling in vortex winds have been discussed in Section 5.1.1. In conjunction with ELF waves generated by electrical discharges in dust devils, these signals can provide a clear signature

for remote sensing of dust devils and have potential to be used for hazard alert purposes during manned or robotic missions to Mars to forecast the approaching dust devil [*Farrell et al.*, 2006].

6.2 Schumann Resonances on Titan

In this Chapter, the same FDTD model employed in the previous Chapters is applied. The typical number of FDTD cells in θ and ϕ directions are 20 and 40, respectively. The grid size in r direction is 5 km.

Three different conductivity profiles are employed to describe the Titan's lower ionosphere. The first one is the "knee" model (equation (2.19)). Figure 6.2 illustrates the "knee" model profile which is determined by the four parameters: $\sigma_{kn} = 1.23 \times 10^{-8}$ S/m, $h_{kn} = 75$ km, $\xi_a = 10.9$ km and $\xi_b = 29.0$ km [*Pechony and Price*, 2004]. Other two conductivity profiles on Titan used in this Chapter are taken from [*Borucki et al.*, 1987] and [*Molina-Cuberos et al.*, 2004] (shown in Figure 6.3). Due to the attachment of the ions and electrons to the cloud particles in the Titan's atmosphere, the conductivity profile including the clouds (dashed line in Figure 6.3) is much smaller than that without including the clouds (solid line in Figure 6.3) below 400 km. For the arbitrary conductivity profiles like what are shown in Figure 6.3, the FDTD method allows robust and easy solution of SR problems.

Figure 6.4 illustrates the time domain data of the E_r and H_ϕ components derived from our FDTD model for Titan conductivity profile shown in Figure 6.2. The distance between the source and receivers is approximately 2400 km. Figure 6.5 indicates the vertical distributions of E_r and H_ϕ components for the first SR mode from the ground to the altitude of 500 km. The E_r component remains con-

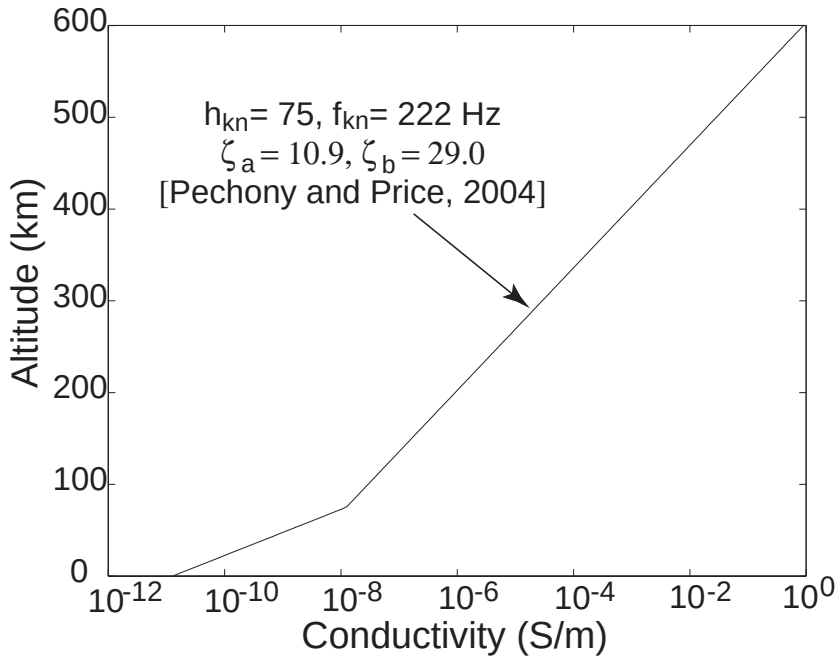

Figure 6.2. "Knee" model conductivity profile on Titan [*Pechony and Price*, 2004].

stant below 40 km, which can be considered as the conducting boundary (defined in [*Sentman,* 1983; 1990a]) for the first SR mode. The H_ϕ component can penetrate to the altitude of approximately 260 km. The eigenfrequencies and Q-factors are derived as described in Section 2.2 by fitting the time domain data. The comparison of the FDTD H_ϕ results and its approximation by Prony's method show in Figure 6.6. In Figure 6.6(a), a good agreement is found by comparing our FDTD results and the fitting data using Prony's method on the H_ϕ component. The FFT results of the time domain data is shown in Figure 6.6(b).

Table 6.2 shows the comparison of our FDTD results for Titan and previous studies [*Morente et al.*, 2003; *Nickolaenko et al.*, 2003; *Pechony and Price*, 2004]. The frequencies and Q-factors of the first three SR modes are given. All of the first SR frequency are in the range of 8-12 Hz, and Q-factor are approximately from 1 to 2.6. Our FDTD results with the "knee" model are close to the data

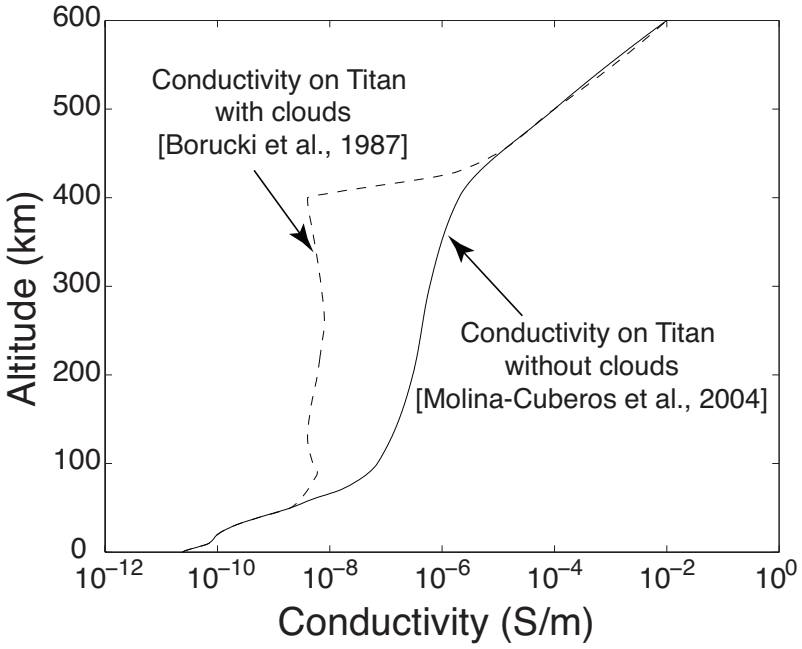

Figure 6.3. The modeled conductivity profiles on Titan [*Borucki et al.*, 1987; *Molina-Cuberos et al.*, 2004].

reported by *Pechony and Price* [2004], and somewhat lower than values calculated by *Morente et al.* [2003]. A large difference is found with the frequencies predicted by *Nickolaenko et al.* [2003], which are approximately 2 times higher than our FDTD results. However, the Q-factors obtained with FDTD model are within the range estimated by *Nickolaenko et al.* [2003].

The conductivity profile (Figure 6.2) used in our FDTD model is taken from [*Pechony and Price*, 2004], which is very close to the profile used in [*Morente et al.*, 2003]. However, a 2-7 Hz difference in the first three modes is found between the results calculated by transmission line matrix method (TLM) [*Morente et al.*, 2003] and our FDTD model. It is believed that this difference comes from the different way to terminate the upper boundary of the cavity in these two models. *Morente et al.* [2003] locate the upper boundary of the Titan resonant cavity at about 180 km, where the conduction current is about one order of magnitude greater than

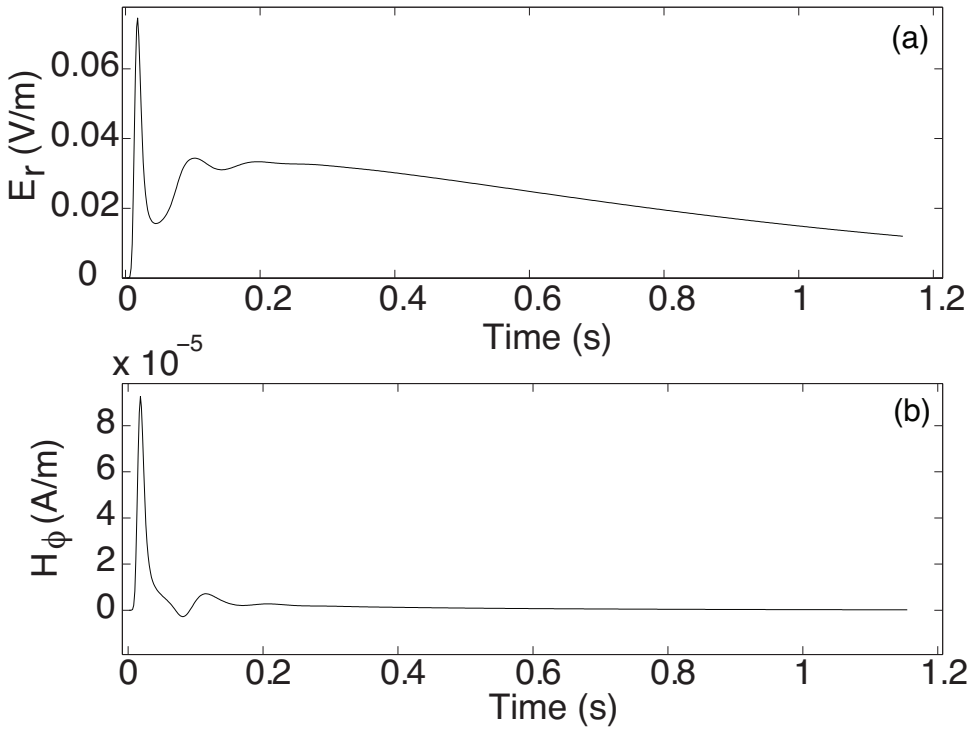

Figure 6.4. The E_r (a) and H_ϕ (b) components in time domain derived by FDTD model for a case of Titan conductivity profile shown in Figure 6.2.

the displacement current. At this altitude, the conductivity is approximately 10^{-7} S/m. We note that the conductivity around 10^{-7} S/m is not high enough to reflect most energy of the extremely low frequency wave. If the upper boundary is located at this altitude, a significant part of the dissipating region for ELF wave at higher altitudes is neglected, and the total energy dissipation in the cavity is reduced. Therefore, the resonance frequencies and Q-factors derived from the TLM model [*Morente et al.*, 2003] appear to be higher than these obtained from FDTD model. We conducted additional tests to find the altitude where the upper boundary can be correctly placed without disturbing the electromagnetic properties of the resonant cavity and the propagation of the ELF waves. In the test simulations, a perfectly conducting surface was positioned at different altitude, h. For h = 180 km, the

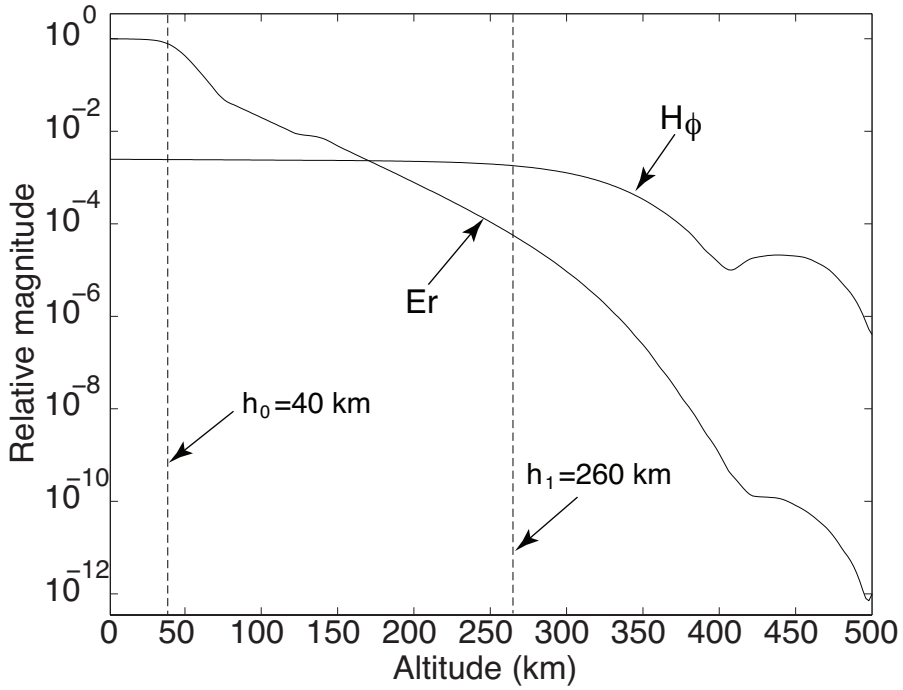

Figure 6.5. The vertical distribution of the magnitude of the E_r and H_ϕ components for the first SR mode on Titan with the conductivity profile shown in Figure 6.2. The h_0 and h_1 indicate the penetration heights of the electric and magnetic components in Titan's atmosphere, respectively.

corresponding first SR frequency is 13.1 Hz, which is close to the value 12.8 Hz, obtained by *Morente et al.* [2003]. The first SR frequency decreases with increasing of the height h of the upper boundary above 180 km. When h is more than 500 km, the first SR frequency remains 10.6 Hz, and does not change any more with increasing h. It means that all of electromagnetic waves are reflected around or below the altitude of 500 km in Titan's atmosphere. Therefore, the upper boundary should be located at the altitude of 500 km or higher in the simulations, rather than at 180 km employed in [*Morente et al.*, 2003]. Two conductivity profiles for Titan taken from [*Molina-Cuberos et al.*, 2004] and [*Borucki et al.*, 1987] (shown in Figure 6.3) are different from the model profile shown in Figure 6.2. In order to determine the correct altitude to place the upper boundary discussed above, we

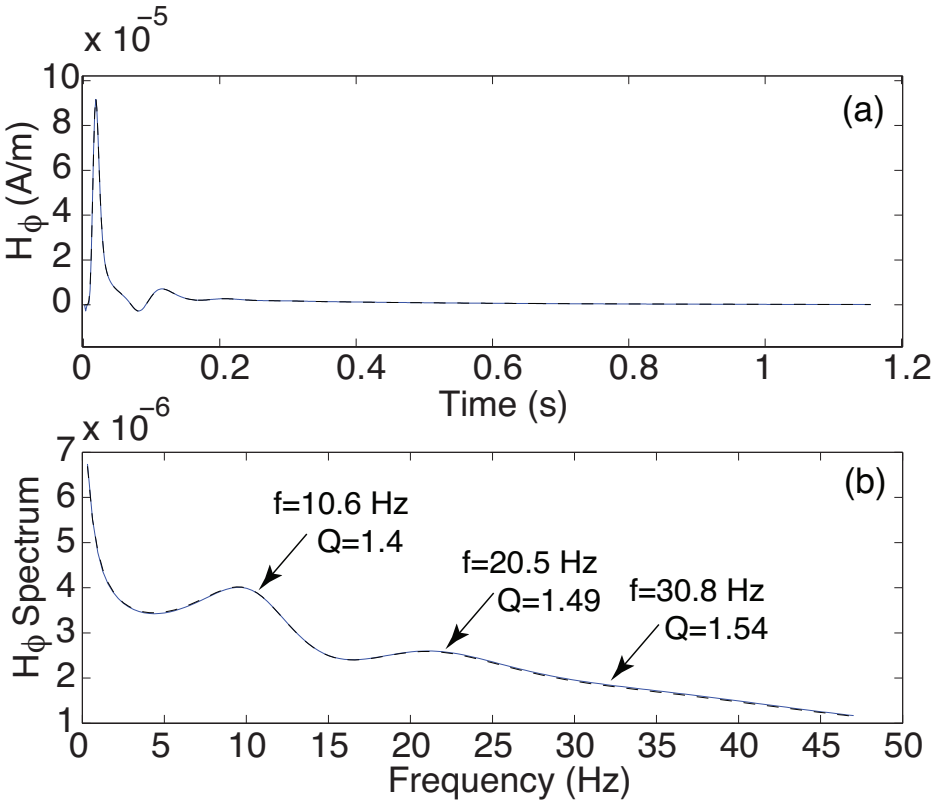

Figure 6.6. (a). Comparison the FDTD result (the dashed line) and the fitting data derived from the Prony's method (the solid line). (b). The FFT results of the two time domain data shown in (a). Note that solid and dashed lines nearly coincide in both panels (a) and (b).

performed series of test runs in which a perfectly conducting surface was positioned at different altitudes above 180 km. It was determined that the first three SR frequencies derived from these two profiles (shown in Table 6.2) remain constant, when the upper boundary positioned at 600 km or higher.

Nickolaenko et al. [2003] derived the SR frequencies using the modified Greifinger's formula [*Nickolaenko and Rabinowicz*, 1982], which is given by:

$$f_n = \frac{c}{2\pi a}\sqrt{n(n+1)}\sqrt{\frac{h_0}{h_1}} \tag{6.1}$$

where h_0 is the altitude of the conducting boundary where the displacement current

Mode number	TLM [*Morente et al.*, 2003]	*Nickolaenko et al.*, [2003]		PUK [*Pechony and Price*, 2004]		FDTD with "knee" model		FDTD with profile from [*Molina-Cuberos et al.*, 2004]		FDTD with profile from [*Borucki et al.*, 1987]	
	f_n	f_n	Q_n	f_n	Q_n	f_n	Q_n	f_n	Q_n	f_n	Q_n
1	12.8	19.9	0.96-2.6	11.8	1.8	10.6	1.40	8.2	0.92	9.4	1.04
2	24.4	35.8	0.97-2.7	22.5	1.9	20.5	1.49	17.4	0 .99	14.3	0.82
3	38.1	51.8	1.01-2.8	34.1	2.0	30.8	1.54	27.3	1.06	31.4	1.23

Table 6.2. Schumann resonances on Titan calculated by different models.

is equal to the conducting current at a given frequency f, namely, the conductivity at altitude h_0 is equal to $2\pi f\varepsilon_0$, and h_1 is the altitude of the reflection boundary defined in [*Sentman*, 1990a]. The h_0 and h_1 are related by equation (6) in [*Nickolaenko et al.*, 2003] as follows:

$$h_1 = h_0 - 2\xi_0 ln(2k\xi_0) \tag{6.2}$$

where k is the wavenumber, and ξ_0 is the scale height of the conductivity profile at altitude h_0. This equation comes from the equation (31) in [*Greifinger and Greifinger*, 1978], which is valid for a single exponential conductivity profile. Therefore, the conductivity in the cavity is assumed to exponentially increase neglecting a "knee point" around 60 km. To illustrate this point, two single exponential profiles are employed in our FDTD model. The single exponential profile is given by:

$$\sigma(z) = \sigma_0 \exp\left(\frac{z-G}{H}\right) \tag{6.3}$$

where G is the reference height and H is the scale height. The parameters are chosen to be the same as those in the Optimistic and Pessimistic models mentioned in [*Nickolaenko et al.*, 2003]. The reference heights are 42 and 38 km, and the scale heights are 2.7 and 4.7 km, respectively, and $\sigma_0 = 5.55 \times 10^{-10}$ S/m. We found a

good agreement on the SR frequencies between our FDTD model results and the data shown in Table 2 of [*Nickolaenko et al.*, 2003]. As discussed above, the large difference between [*Nickolaenko et al.*, 2003] and other models (see Table 6.2) can be explained mainly by the different conductivity profiles used in these models.

6.3 Schumann Resonances on Venus

Borucki et al. [1982] reported the conductivity profile on Venus below altitude of 80 km. Because cloud and haze particles attach ions at around the altitude of 50 km, the conductivity is reduced in this region, and discontinuity in conductivity appears around 50 km. Such a profile can not be approximated by a "knee" model profile, so a "double-knee" model developed by *Pechony and Price* [2004] is employed. The first line in Table 6.3 indicates the parameters determining the conductivity on Venus. The conductivity profile on Venus is shown by a solid line in Figure 6.7.

The E_r time domain data and spectrum derived from FDTD model are shown as solid lines in Figure 6.8. Dashed lines illustrate the approximation by Prony's method. Comparing with SR on Titan, the resonant modes are much sharper, and high-order modes can be clearly observed in Figure 6.8(b). The first three SR frequencies and Q factors on Venus derived from three different models are shown in Table 6.4. A good agreement is found for the frequencies, with the difference generally not exceeding 3%. The Q-factors derived from our FDTD model and those given in [*Pechony and Price*, 2004] are close to each other. These values, however, are approximately 2 times greater than the values calculated by *Nickolaenko and Rabinowicz* [1982]. The equation which was used to derive the Q

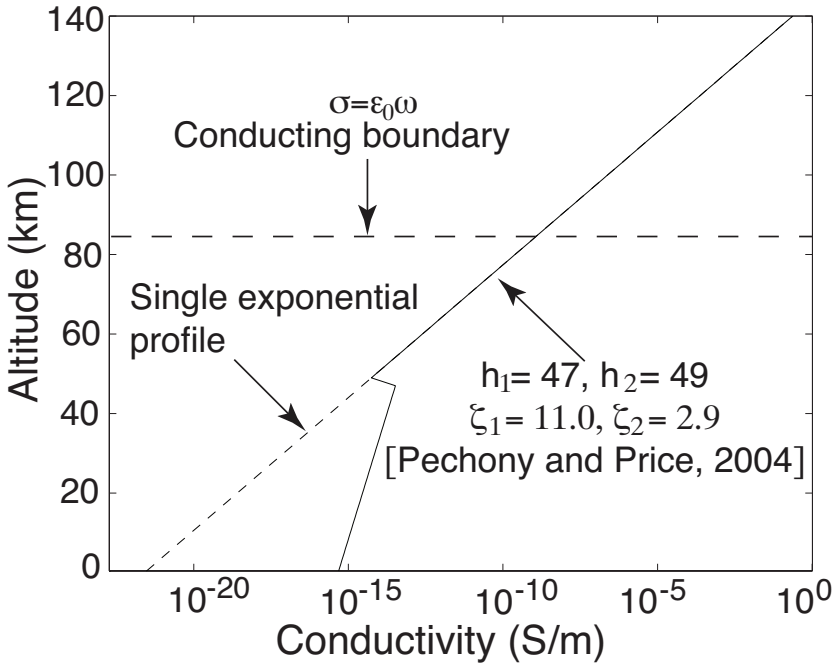

Figure 6.7. "Double-knee" model on Venus [*Pechony and Price*, 2004].

factors in [*Nickolaenko and Rabinowicz*, 1982] is:

$$Q_n = \frac{1}{\pi}\left(\frac{\xi_1}{h_1} + \frac{\xi_2}{h_2}\right)^{-1} \tag{6.4}$$

where h_1 and h_2 are the altitudes of the conducting and reflection boundary, respectively, and ξ_1 and ξ_2 are the corresponding conductivity scale heights. In other papers [*Sentman*, 1990b, 1996a], a similar equation used to derive Q-factors is given by:

$$Q_n = \frac{2}{\pi}\left(\frac{\xi_1}{h_1} + \frac{\xi_2}{h_2}\right)^{-1} \tag{6.5}$$

A factor of two difference between equations (6.4) and (6.5) is a likely reason for the observed difference in Q-factors between our FDTD model and the analytical model presented in [*Nickolaenko and Rabinowicz*, 1982].

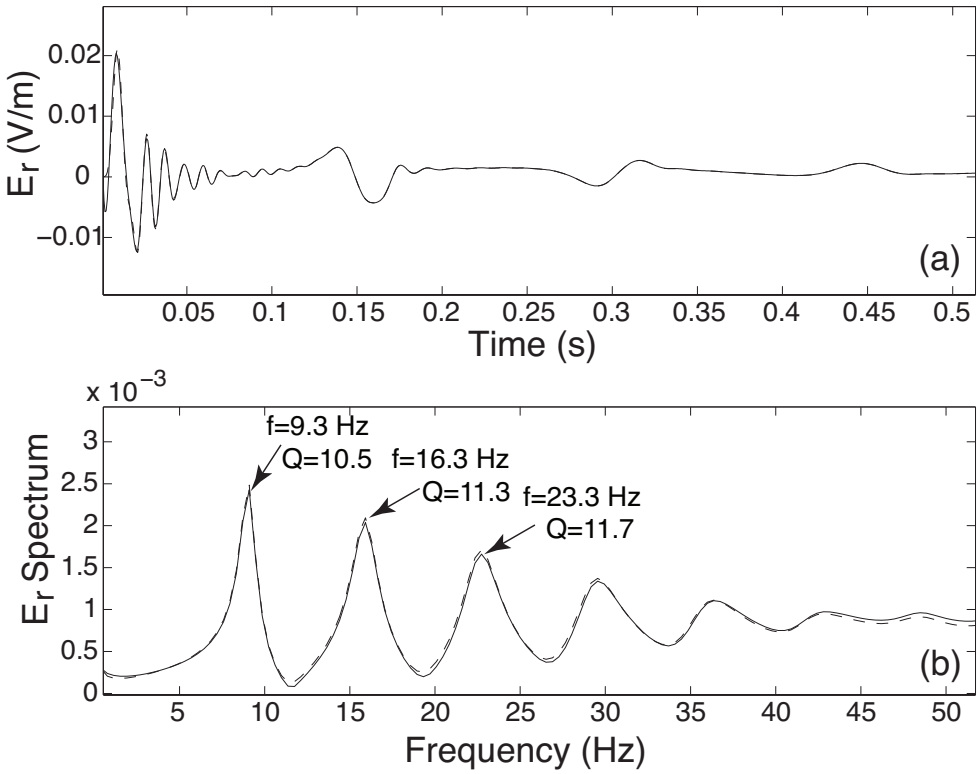

Figure 6.8. The time domain data (a) and spectrum data (b) of SR on Venus with "Double-knee" model. (Solid line: FDTD results; Dashed line: approximation using Prony's method)

	σ_1 (S/m)	σ_2 (S/m)	h_1 (km)	h_2 (km)	ξ_1 (km)	ξ_2 (km)
Venus	3.34×10^{-14}	5.57×10^{-15}	47.0	49.0	11.0	2.9
Mars(day)	8.35×10^{-9}	5.57×10^{-8}	28.0	53.0	3.5	4.6
Mars(night)	8.35×10^{-9}	5.57×10^{-8}	30.0	58.0	3.5	6.1

Table 6.3. The parameters of conductivity profiles on Mars and Venus.

The altitude where $\sigma = 2\pi\varepsilon_0 f$ can be considered as a conducting boundary (see Figure 6.7) for a specific frequency, f. The atmosphere below this boundary can be considered as insulating, whereas the atmosphere is conducting above this boundary [*Sentman*, 1990a, 1996a]. For the first SR mode on Venus, the frequency, f, is approximately 10 Hz. The boundary between the conducting and nonconducting atmosphere therefore corresponds to the altitude where $\sigma = 2\pi\varepsilon_0 f = 5 \times 10^{-10}$

Mode number (n)	*Nickolaenko* and *Rabinowicz* [1982]		PUK [*Pechony and Price*, 2004]		FDTD	
	f_n	Q_n	f_n	Q_n	f_n	Q_n
1	9.0	5.1	9.3	10.5	9.05	10.07
2	15.8	5.1	16.3	11.3	15.9	10.23
3	22.7	5.2	23.3	11.7	22.64	10.31

Table 6.4. Comparison of FDTD results and previous studies of SR on Venus.

S/m. *Borucki et al.* [1982] reported only conductivity profile below 80 km on Venus, and the maximum value of the conductivity is approximately 10^{-10} S/m at 80 km. Therefore, the region studied by *Borucki et al.* [1982] (below 80 km) can be considered as an insulating space for ELF waves, and the conductivity distribution in this region is not important for SR studies. *Pechony and Price* [2004] extended the conductivity to a higher altitude by a "double-knee" model. Since the SR parameters are only dependent on the conductivity distribution in the conducting region (above 80 km) in Venus-ionosphere cavity, which is determined by the reference height (h_2) and the scale height (ξ_2) in this "double-knee" model (see Table 6.2), it is believed that the nearly identical results can be obtained using both the "double-knee" model (solid line in Figure 6.7) and a single exponential conductivity profile (dashed line in Figure 6.7). We have performed additional simulations with single exponential conductivity profile with the same reference height ($G = 49$ km) and the scale height ($H = 2.9$ km) as those in the upper part of the "double-knee" model. As expected, the results appeared to be in a good agreement with those derived from the "double-knee" model. The flat frequency dependence of Q-factors (last column in Table 6.3) also support our conclusion, that the "double-knee" model shown in Figure 6.7 has the same effect on SR parameters as a single exponential profile. Readers are referred to additional discussion on related topics in [*Mushtak and Williams*, 2002; *Yang and Pasko*, 2005].

6.4 Schumann Resonances on Mars

Two conductivity profiles are employed in the present study to account for distribution of conductivity in Martian atmosphere. The first one is a two scale height profile [*Sukhorukov*, 1991] (see equation (2.18)) with six parameters as follows: h_1=53 km, ξ_1=6.0 km, h_2=100 km, ξ_2=4.8 km, $\sigma(h_1)=2\pi f_0\varepsilon_0=7.5\times10^{-10}$ S/m, and $\sigma(h_2)=1/8\mu_0\pi f_0\xi_1^2=1.02\times10^{-4}$ S/m assuming f_0= 13.5 Hz (see Figure 6.9). Another conductivity profile on Mars is taken from PUK model [*Pechony and Price*, 2004] (see Figure 6.10 and discussion in section 2.3.2). The PUK model is principally different from the conductivity profiles discussed above, because it employs a nonuniform conductivity profile. The Martian conductivity on day and night sides is assumed to have different distributions. For this purpose, in PUK model, two "double-knee" conductivity profiles with different parameters (shown in Table 6.2) are chosen. In the simulation, half planet is covered by day-time conductivity profile, and the other half is covered by night-time conductivity profile. The specific choice of parameters for the profiles presented above is motivated by the availability of solutions of related SR problems [e.g., *Pechony and Price*, 2004], against which the FDTD results presented in this Chapter are compared. The E_r time domain data and spectrum derived from FDTD model are shown as solid lines in Figure 6.11. Dashed lines illustrate the approximation by Prony's method.

Table 6.5 shows the simulation results on the first three SR frequencies and Q-factors for the resonant cavity on Mars. The first three SR frequencies predicted by *Sukhorukov* [1991] are approximately 13, 25, and 37 Hz, and the Q-factors are between 3.3 and 4.0. These values appear to be substantially different from those calculated by *Pechony and Price* [2004]. The first three SR frequencies reported by *Pechony and Price* [2004] are 8.6, 16.3, and 24.4 Hz, and the Q-factors are around

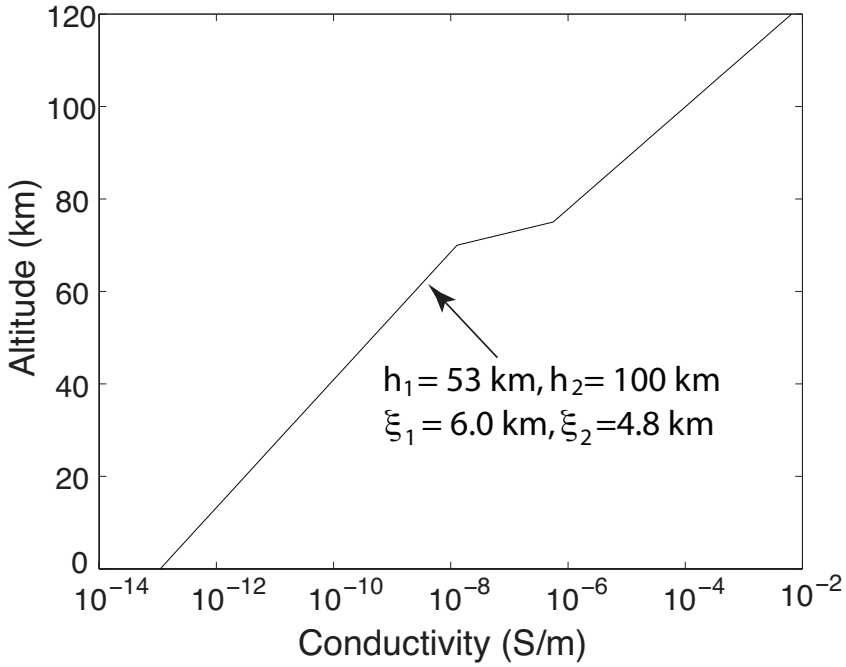

Figure 6.9. Two scale height conductivity profile on Mars [*Sukhorukov*, 1991].

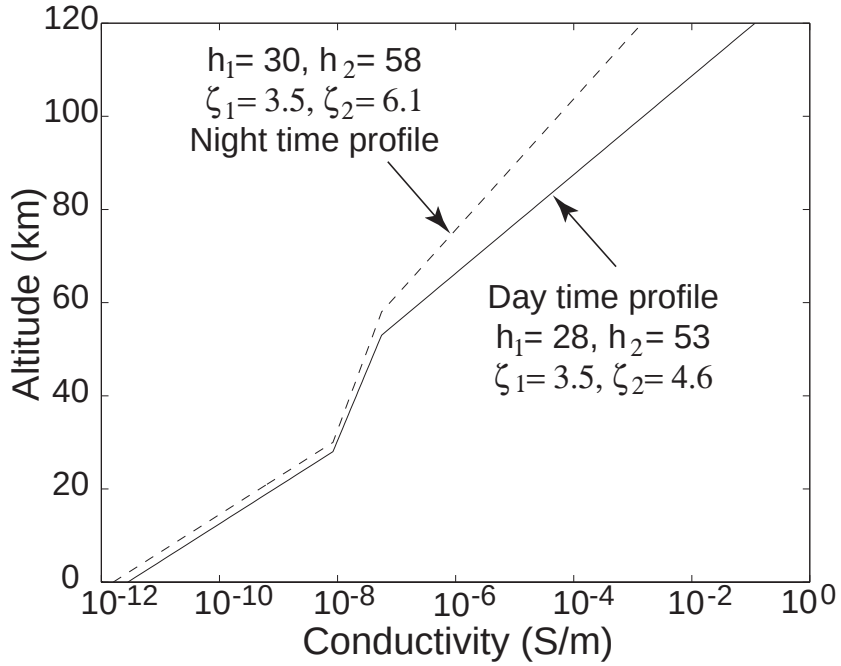

Figure 6.10. Partially uniform knee model on Mars [*Pechony and Price*, 2004].

2.4. The observed differences can be explained by the different conductivity profiles used in these models as illustrated in Figures 6.9 and 6.10. *Pechony and Price* [2004] used a PUK model. FDTD simulations have been performed using these two conductivity models. The results are shown in Table 6.5. A good agreement is found between our FDTD results and results reported in [*Sukhorukov*, 1991; *Pechony and Price*, 2004] for the corresponding conductivity profiles. The results shown in the last column in Table 6.5 are the peak frequencies of the first three SR modes calculated recently by [*Molina-Cuberos et al.*, 2006] using TLM model [*Morente et al.*, 2003], in which the second and third modes have same frequencies. The peak frequency is defined as the frequency where the maximum power occurs. Due to the interference between the different modes in the resonant system, the peak frequencies deviate from the eigenfrequencies, and the deviation depend on the magnitude of each mode at the observation point. Therefore, we can find the different peak frequencies at different locations in the cavity and on different wave components. In [*Molina-Cuberos et al.*, 2006], the second and third modes form a single peak at 21.7 Hz due to the interference, and can not be clearly distinguished. Therefore, we conclude that the peak frequency is not suitable for the study of SR in a planetary resonant cavity with low Q-factor, such as Mars and Titan. We note that numerical techniques have been reported to calculate the SR parameters in the time domain and frequency domain, such as Lorentzian fitting [*Sentman*, 1987; *Mushtak and Williams*, 2002], the complex demodulation method [*Sátori et al.*, 1996], and Prony method [*Füllekrug*, 1995; *Yang and Pasko*, 2005], which allow accurate derivation of eigenfrequencies for low Q-factor cavity. The Prony method, in particular, is employed for all calculations reported in this section (see Section 2.2).

To simplify the problem, the Martian crust is assumed to be perfectly conduct-

Mode number (n)	*Sukhorukov* [1991]		PUK [*Pechony and Price*, 2004]		FDTD with conductivity profile of [*Sukhorukov*, 1991]		FDTD with PUK		FDTD with low conductivity Martian crust		*Molina-Cuberos et al.* [2006]
	f_n	Q_n	f_n	Q_n	f_n	Q_n	f_n	Q_n	f_n	Q_n	f_n (peak)
1	13-14	3.3-3.7	8.6	2.3	14.3	3.8	8.8	2.27	7.3	2.5	11.0
2	25-26	3.5-3.8	16.3	2.4	25.8	4.0	16.1	2.35	13.1	2.5	21.7
3	37-38	3.7-4.0	24.4	2.4	37.4	4.2	23.6	2.45	19.2	2.8	21.7

Table 6.5. Schumann resonances on Mars calculated by different models.

ing. Although a low-frequency resonant cavity is roughly established for Mars, the low-conductivity upper Martian crust will be much less efficient as a boundary to reflect ELF waves than the surface of the Earth. The Martian surface does not hold a conductivity characteristic of the Earth shield (10^{-4} S/m) until depth of approximately 40-60 km [*Grimm*, 2001]. It means that the ELF waves can penetrate deeper into Martian crust than Earth shield, and ELF waves should suffer more attenuation during the propagation. We have performed some additional numerical experiments in which we inserted a low conductivity layer below Martian surface to account for the Martian crust. The depth of this layer is 40 km, and the conductivity in this layer is 10^{-7} S/m. The first three SR frequencies decrease from 8.8, 16.1, and 23.6 Hz to 7.3, 13.1, and 19.2 Hz, respectively. The difference between the models with and without low conductivity Martian crust is approximately 20% (see Table 6.5). Therefore, the conductivity distribution of Martian crust from ground surface to the depth of 40-60 km is also an important factor determining the SR parameters on this planet. The measurements of the SR parameters can provide a good method to remotely sense the Martian subsurface conductivity profile to depths of 40-60 km, and locate anomalous conductivity structures in the Martian crust, such as mineral deposits and underground water or ice [*Simpson and Taflove*, 2006a].

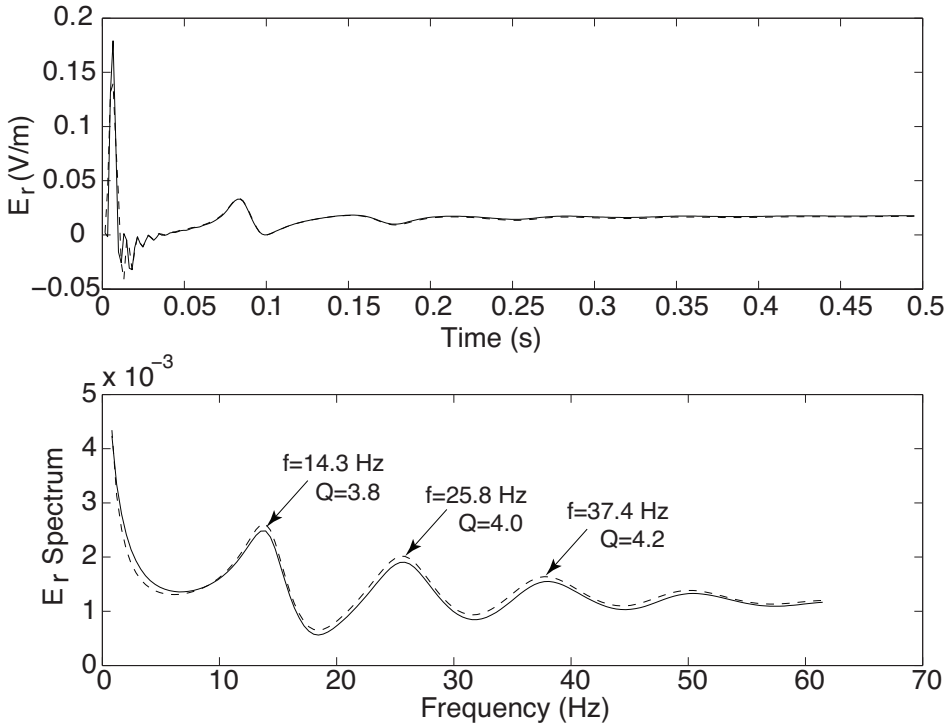

Figure 6.11. Time domain data and spectrum of E_r component derived from the cavity with two scale height conductivity profile [*Sukhorukov*, 1991].

6.5 Comparative Remarks

Following equation (1.1), the SR frequencies are inversely proportional to the radius of the planet. Since the radius of Titan (2575 km) is approximately 40% of the Earth's radius (6370 km), the SR frequencies on Titan should be 2.5 times of those on the Earth. However, the SR frequencies in these two cavities derived from our modeling are close to each other (See Tables 3.1 and 5.2). It is important to emphasize that the conductivity distribution in a planetary resonant cavity is also an important factor which determines the SR frequencies, besides the radius of the planet. In Figure 6.2, the conducting boundary in Titan's atmosphere is around 40 km. The large region between this conducting boundary and the altitude of 500

km with the conductivity ranging from 10^{-9} to 10^{-6} S/m critically damps the ELF waves leading to the SR frequencies which are much lower than those predicted by equation (1.1) and also to the very low Q-factor in the cavity. In Venus modeling (see Section 5.3), the conducting boundary begins at 82 km. The small scale height of the Venusian conductivity above 82 km leads to a relatively sharp increase in the conductivity above this altitude allowing to terminate the cavity at 130 km. The dissipating region for ELF waves on Venus has much smaller altitude extent than that on Titan, and the planetary resonant cavity on Venus is a low loss system. Therefore, the Q-factors are very high and the SR frequencies appear to be close to those calculated using equation (1.1). Besides the atmospheric conductivity distributions, the conductivity below the planetary surface is also important to determine the SR parameters. As discussed in Section 5.4, the low conductivity in the Martian crust causes a 20 % decrease of the first SR frequency. Since the crust conductivity used in the simulations is artificial, the accurate calculation can be determined by the realistic measurement of the planetary crust.

6.6 Summary

The main conclusions in this Chapter can be summarized as follows:

• The first SR frequency on Titan is approximately 8-10 Hz, and the Q-factor is around 0.9-1.4. The height of Titan-ionosphere cavity depends on the conductivity profile. To accurately calculate SR parameters on Titan, the cavity should be terminated at the altitude where the conductivity is approximately equal to 10^{-3} S/m. The distribution of the clouds is also an important factor to influence SR parameters on Titan.

• The first SR frequency on Venus is approximately 9 Hz, and the Q-factor is around 10. The conductivity on Venus below 80 km is not important for the SR parameters. The results demonstrate that an accurate conductivity profile above 80 km is needed to provide accurate solutions for SR parameters on Venus.

• The first SR frequency on Mars is approximately 8-9 Hz, and the Q-factor is around 2.4. However, these SR parameters are also influenced by the conductivity distribution of Martian crust from the ground surface to the depth of 40-60 km.

Chapter 7

The Seasonal Variations of Global Lightning Activity Extracted From Schumann Resonances Using a Genetic Algorithm Method

7.1 Introduction

The genetic algorithm (GA) is an optimization and search technique based on the principles of genetics and natural selection. Due to its powerful ability to optimize a large number of variables with extremely complex cost surfaces, GA becomes a popular method to solve the optimization problems [e.g., *Haupt and Haupt*, 2004].

In previous Chapters, the diurnal and seasonal variations of SR parameters have been calculated using FDTD model. The global lightning activity employed in those simulations are taken from previously published sources [*Sentman and Fraser*, 1991]. In this Chapter, the global lightning activities in Africa, South-

East Asia, and South America in different seasons are inversely calculated from experimental Schumann resonance power measurements reported by *Price and Melnikov* [2004] using a new optimization method based on GA [e.g., *Haupt and Haupt*, 2004]. The associated connection between SR frequency variations and the global lightning activity during different seasons are discussed.

7.2 Global Lightning Activity Inversely Derived From Schumann Resonances

7.2.1 Global Lightning Activity Inversely Derived From Schumann Resonances Using GA Method

The same 3D FDTD modeling as applied in Chapter 4 is employed in this Chapter. The typical number of FDTD cells in r, θ and ϕ directions are 20, 20 and 40, respectively. The conductivity profile in the cavity is derived from the IRI model for a representative day of January 15, 2000, May 15, 2000 and October 15, 2000 from 0000 UT to 2400 UT, respectively, to account for the diurnal conductivity variations during Winter, Spring ,and Fall seasons. Two modeling receivers are located at the locations corresponding to the SR field stations at Nagycenk, Hungary [*Sátori and Zieger*, 1999] and Negev desert, Israel [*Price and Melnikov*, 2004]. The vertical electrical field component (E_r) and magnetic component in North-South (H_{NS}) direction are calculated and compared with measurements reported in [*Sátori et al.*, 1996; *Price and Melnikov*, 2004].

Unit magnitude of each source at three major lightning regions is employed in FDTD simulations. The total signal received at the station can be expressed by the sum of the waves from these three unit sources multiplied by the magnitude

of the lightning activity in these three thunderstorm regions. Assuming that the power of lightning activity in South-East Asia, Africa, and South America follows Gaussian distribution with universal time t, lightning power variations in these three regions can be represented as $P_i = A_i e^{\left(\frac{t-T_i}{w_i}\right)^2} + c_i$ $(i = 1, 2, 3)$, respectively, where A_i, T_i, and w_i indicate the magnitude, central time, and time width of the lightning activity, and c_i is the background level of the lightning activity in each region.

The global lightning activity is inversely derived by a continuous GA optimization method [*Haupt and Haupt*, 2004, pp. 51]. The time integration of the square of the difference between our FDTD results and the experimental measurements reported by *Price and Melnikov* [2004] is chosen as the cost function in the optimization. Thirteen parameters (three sets of A_i, T_i, w_i, and c_i, as well as a DC component corresponding to the global lightning background noise) are adjusted to minimize the cost function by GA method. A population of 80 chromosomes is generated to begin the GA procedure. In every iteration, 20 most-fit chromosomes forming the mating pool are chosen to reproduce offspring in the next generation. Heuristic crossover [e.g., *Haupt and Haupt*, 2004, pp. 58] is employed in the chromosome mating process. We choose a mutation of 20% indicating that $0.2 \times 13 \times 80 \simeq 208$ variables are randomly mutated in each generation [*Haupt and Haupt*, 2004, pp. 60].

Figure 7.1 shows North-South migrations of lightning activity in America, Africa, and Asia [*Sátori et al.*, 1999]. It is clearly observed that lightning activity occurs mainly in the Summer hemisphere, moving from one hemisphere to the other during the annual cycle. From April to October, the lightning centers in these three regions are all located in northern hemisphere, and reach the northernmost positions during July. From October to next April, these centers move

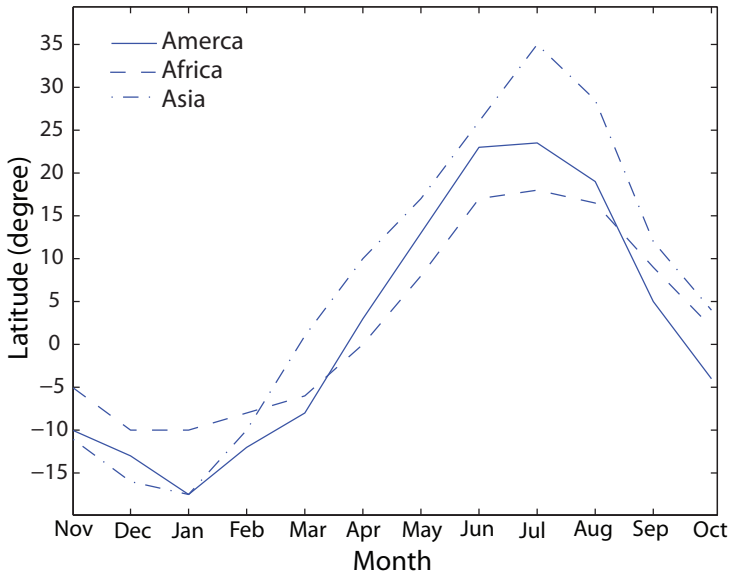

Figure 7.1. Seasonal North-South migrations of the lightning activity centers in South-East Asia, Africa, and America [*Sátori et al.*, 1999].

to southern hemisphere, and go to the southernmost locations around January. In FDTD calculations, three seasons (May, October, and January) have been simulated, and the latitudes of three lightning centers associated with each season are taken from Figure 7.1. The dashed line shown in Figure 7.2(a) is experimental H_{NS} measurement of the first SR mode as a function of universal time reported in [*Price and Melnikov*, 2004], which is applied as the aim function in GA optimization. The fitting curve (solid line in Figure 7.2(a)) is calculated by our FDTD model with the optimized lightning activity in May. The magnitude (A_i), width (w_i), central time (T_i), and background level (c_i) in three centers are adjusted by GA, and a good fitting is completed in Figure 7.2(a). The associated optimized distributions of the lightning activity in Asia, Africa, and America are given in Figure 7.2(b). Three peaks appear at 0800, 1200, and 1900 UT in Asia, Africa, and America, respectively. Africa has the strongest lightning activity magnitude, about 50%

greater than Asia. American lightning is much weaker than in other two regions. Diurnal frequency variation of the first SR mode (Figure 7.2(c)) is derived from E_r component received at the simulated SR station in Hungary. Same method has been applied to calculate the lightning distributions in October and January shown in Figure 7.3. Different with Figure 7.3(b), lightning activities in Asia and Africa both approximately decrease by a factor of 40% in October. American lightning becomes two times as strong as that in May, and exhibits almost the same level as African one. In January, Asian lightning activity reaches its maximum in the annual cycle, about two times greater than that in May and October, and becomes the dominant one in the cavity, but African lightning activity goes to its minima. The SR frequency variations derived in October and January are shown in Figures 7.3(c) and 7.3(f), respectively.

Due to the position of the SR stations with respect to the three lightning centers, African lightning center shows less contribution to H_{NS} power spectrum than other two centers [*Yang and Pasko*, 2006]. However, comparing with other components (E_r and H_{EW}), which are dominated by African lighting, H_{NS} component is the most optimal candidate bringing the best information about the lightning activity in all three lightning centers. This is the reason why we choose H_{NS} power spectrum as the aim function in GA optimization. Since GA optimization method randomly selects the results to minimize the cost function during iterations, its results are not exactly the same in every simulation. However, these results have the same features which are illustrated in Figures 7.2 and 7.3.

Obvious seasonal power variations of the lightning activity in Asia, Africa, and America are observed in Figures 7.2 and 7.3. In May, African lightning has the strongest power level in three centers, and American lightning goes to the weakest level at the same time. In October, lighting activity in Asia and Africa are both

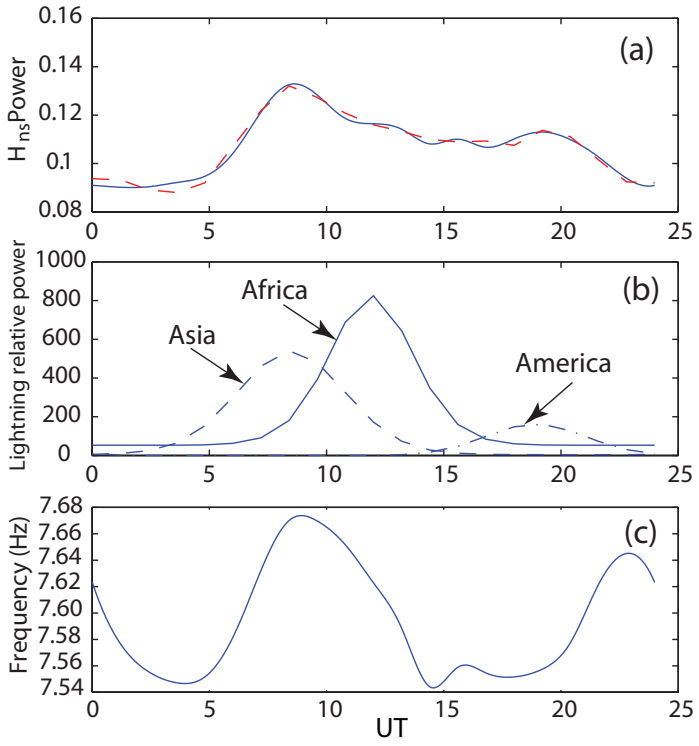

Figure 7.2. (a) Comparison of diurnal H_{NS} power variations of the first SR mode in May derived from experimental measurements (dashed line) [*Price and Melnikov*, 2004] and FDTD results (solid line). (b) The distributions of the lightning activity in Asia, Africa, and America derived by GA optimization in May. (c) Diurnal frequency variation of the first SR mode with the lightning distributions shown in (b).

reduced to 60% of their level in May. American lighting activity increases by a factor of 3, and almost has the same magnitude as African lightning activity. Due to the longer duration time of American lightning activity, we believe that America makes more significant contribution to global lightning activity in October. Since May is close to Summer time in Africa, it is easy to understand that African lightning activity in May is greater than that in other two lightning centers, and its own level in October and January. Similarly, American lighting reaches its peak when South America goes to Summer in October. In January, African lighting is reduced to its minimum in the annual cycle, since it is Winter in Africa. Amer-

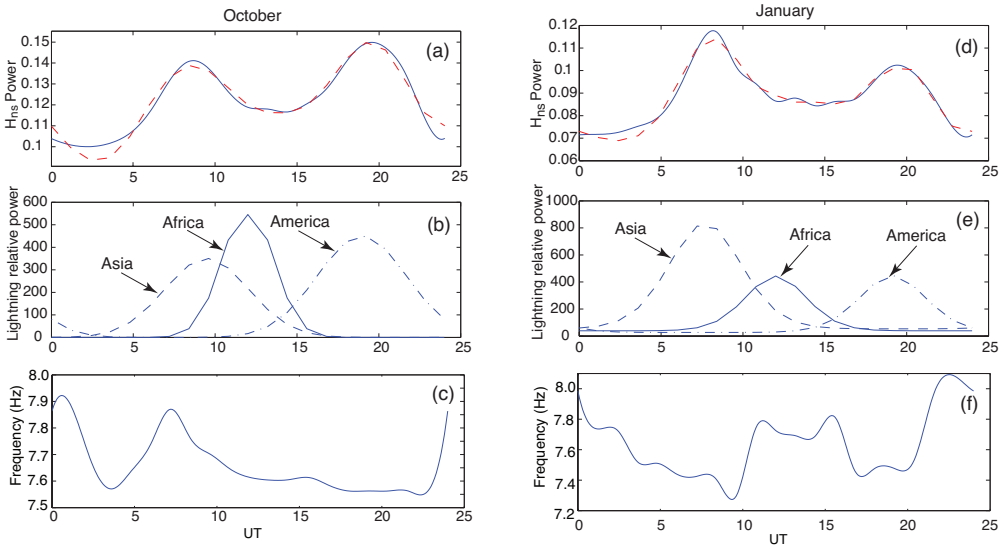

Figure 7.3. Comparisons of diurnal H_{NS} power variations of the first SR mode in October (a) and January (d) derived from experimental measurements (dashed line) [*Price and Melnikov*, 2004] and FDTD results (solid line). The distributions of the lightning activity in Asia, Africa, and America derived by GA optimization in October (b) and January (e). Diurnal frequency variation of the first SR mode with the lightning distributions in October (c) and January (f).

ican lightning keeps the same level as that in October. The maximum of Asian lightning appears during this season, and is approximately two times as great as other two regions. Since the simulated receiver is covered by the lightning source region centered at the latitude shown in Figure 7.2 in July, the detected SR power spectrum is strongly disturbed by the strong source currents. Therefore, we do not report the simulation results in July. However, we believe that African lighting should reach its annual maximum in July when it is Summer time in Africa.

Consistent with measurements given in Figure 4.2, reported by *Sentman and Fraser* [1991], African lightning activity becomes the strongest among the three regions in April and increases by 50% in compasion with its September level. Inversely, in September, the magnitude of American lighting becomes greater than other two regions, and approximately 25% greater than that in April. Although

the data in [*Sentman and Fraser*, 1991] were collected in April and September, one month earlier than the months we studied in our simulations, all of these features can be still found in our simulation results. However, in contrast with our results, Asian lightning activity in both April and September has the same magnitude in [*Sentman and Fraser*, 1991], and always is the weakest one among the these three lightning centers during both months.

Some related results detected by the Optical Transient Detector (OTD) have been given in [*Christian et al.*, 2003]. Africa is the most active lightning center with the highest annualized flash rate, and Americas ranks second. Flash density is generally greatest during the respective hemisphere Spring and Summer seasons over land and year-round in coastal zones. In Figure 6(b) of [*Christian et al.*, 2003], lightning activity in Africa and Asia has almost comparable magnitude in May, and America has much weaker lightning activity than other two regions, which agrees with our result shown in Figure 7.2(b). Furthermore, OTD data reveals that Africa has stronger lighting activity than America, and Asia is the region having weakest lightning activity among the three lightning centers in October. The same features can be also observed in Figure 7.3(b). The disagreement appears between our FDTD results and OTD measurement in January. Asian lightning becomes much stronger than other two regions in our FDTD simulations, while Africa still has the highest lightning flash rate shown in Figure 6(a) of [*Christian et al.*, 2003]. Since OTD data includes both intra-cloud and cloud-to-ground lightning discharges, and only cloud-to-ground lightning contributes to Schumann resonances, it might be an explanation for this disagreement. A similar problem has been discussed in [*Greenberg and Price*, 2007].

7.2.2 Seasonal SR Frequency Variation Related to Global Lightning Activity

The diurnal frequency variations of the first SR mode with GA optimized lightning activity are shown in Figures 7.2 and 7.3. In May, the frequency goes to the peak around 1000 UT, and the magnitude of the variation is approximately 0.1 Hz, which agrees with the experimental Summer measurements [*Sátori et al.*, 1996; *Sátori*, 1996; *Ondrášková et al.*, 2007] very well. In October, the frequency peak appears at 0800 UT, and still has similar variation tendency with that in May. In January, the situation is significantly different. SR frequency decreases during the initial several hours, and reaches the minimum (7.3 Hz) at approximately 1000 UT, then increases to 7.8 Hz at 1200 UT. Similar features have been reported in experimental Winter measurements [*Sátori et al.*, 1996; *Sátori*, 1996; *Ondrášková et al.*, 2007]. We believe that the different frequency variations during different seasons can be explained by the seasonal variations of lighting activity. In Spring and Summer (May to September), African lightning center is located in north hemisphere with the latitude more than 10^o. Its distance to Nagycenk station is less than 4000 km. The other two centers are approximately at the distances of 10000 km from the station close to nulls of spatial field distribution of the first SR E_r component. Furthermore, African lightning activity reaches its peak, and is much stronger than at other two centers during Summer time. An additional FDTD simulation, in which only one source is located at Africa, has been performed. The result shown in Figure 7.4 is in a good agreement with that shown in Figure 7.2(c) with a peak at around 1000 UT. Therefore, we believe that the magnitude of E_r component and its frequency variation detected at Nagycenk station are mainly determined by the waves from Africa in Spring and Summer, when African lightning center is close

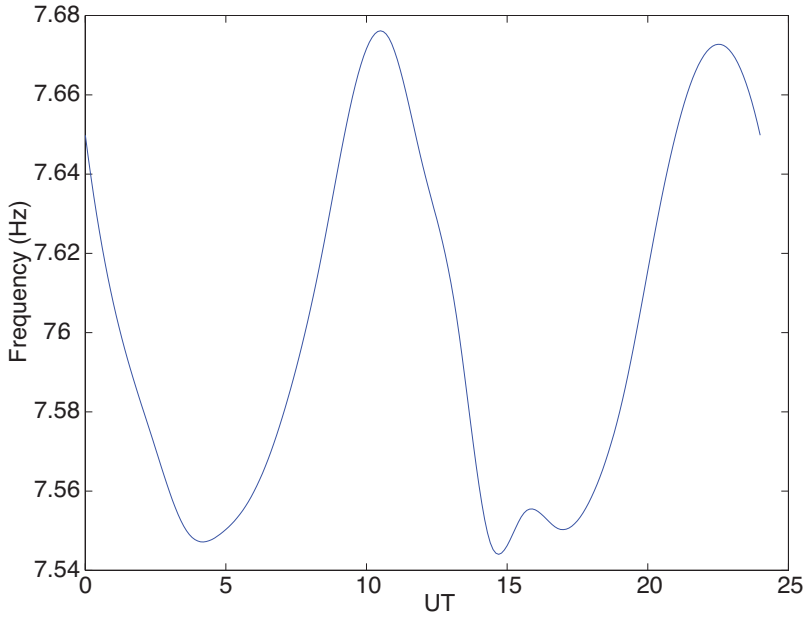

Figure 7.4. Diurnal frequency variation of the first SR mode accounting for only African lightning center obtained using FDTD model.

to the station and its magnitude reaches maximum. In October, African lightning moves southwards to equator, and its influence on Nagycenk station decreases due to the spatial distribution of E_r component [*Yang and Pasko*, 2007]. Although the lightning activity in Asia and America shows more influence on the frequency variation, African lightning activity is still the most significant one to control the frequency variation. Therefore, the results shown in Figure 7.3(c) are similar with Figure 7.2(c). In January, African lighting center moves to its southmost position in the annual cycle (7000 km to Nagycenk station), and its magnitude is reduced to the level less than half value of that in Summer. At the same time, Asian lightning activity increases to its maximum in the annual cycle, and is approximately two times as great as those in Africa and America. Therefore, Asian lightning becomes the dominant one to control SR frequency in Winter.

To provide additional insight on SR frequency variations, a set of additional

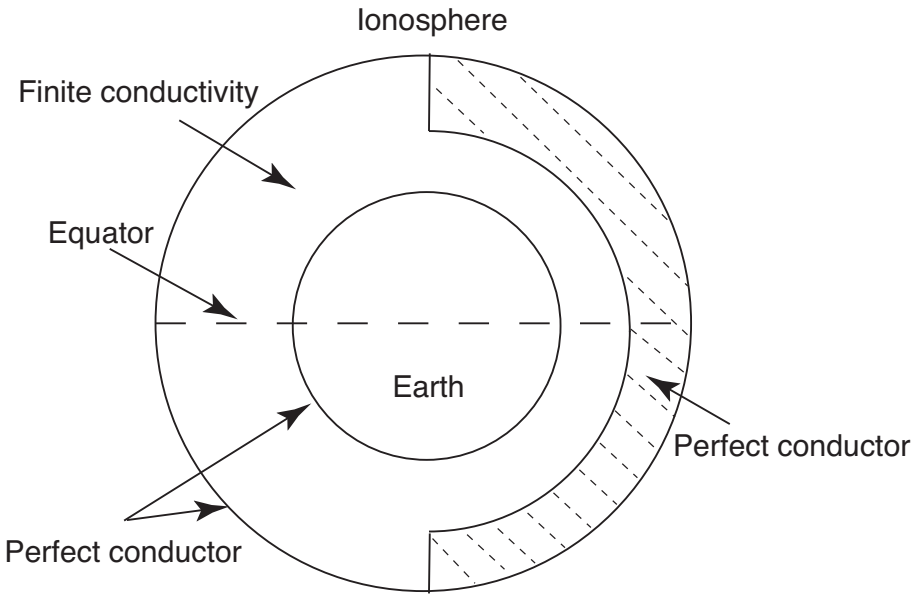

Figure 7.5. The cavity with artificially asymmetric conductivity. The height of half cavity is 100 km. For another half, the height is 50 km.

FDTD simulations have been performed. In these simulations, an artificially asymmetric cavity as shown in Figure 7.5 is employed. Half cavity has a height of 100 km, and another half has height of 50 km. The half cavity with a height of 50 km effectively accounts for the Earth at daytime, and the other half accounts for the Earth at night. A single source (3000 km by 3000 km) moves around the Earth on the equator synchronized with the motion of the day-night terminator, and is always activated in regions at local afternoon in the cavity. Figure 7.6 shows FDTD results derived from the cavity (shown in Figure 7.5) without the inclusion of the conductivity between the perfectly conducting cavity boundary. Due to the asymmetry of the cavity, the first SR mode is split into two frequencies. One is 10.1 Hz (f_1), and another is 10.45 Hz (f_2). Here, we define the modes with the frequencies f_1 and f_2 as modes M_1 and M_2, respectively. At 0824 and 0936 UT, the magnitude of M_1 is much stronger than that of M_2. At 1048 UT, the receiver is close to the nodal line of the first SR mode. The magnitude of M_1 and M_2 de-

creases and increases, respectively. At 1200 UT, the receiver passed the nodal line. The M_2 magnitude becomes much stronger than that of M_1. Since the receiver is close to the nodal line of the first SR mode at 1048 and 1200 UT, the magnitude of first SR mode is much weaker at these time than at other times. After 1200 UT, the magnitude of M_1 increases, and the M_2 magnitude decreases to the level at 0824 UT. For test purposes, several different conductivity profiles are employed in Figures 7.7-7.9 to observe the variation of the mode splitting spectrum within a cavity conductivity variation from zero to the realistic values. Figure 7.7 shows the spectrum derived with a conductivity $= 8 \times 10^{-12}$ S/m. The spectrum of the resonance modes becomes wide and flat due to the conducting loss in the cavity. The modes with weak magnitudes (e.g., peaks at 10.45 Hz at 0824 and 0936 UT) are merged in the adjacent strong modes. However, two splitting frequencies can be still observed in the plots corresponding to 1312 and 1424 UT. With the conductivity increasing to 3×10^{-11} S/m (shown in Figure 7.8), all splitting modes of the first SR mode are merged together and form one single peak. A jump of the first peak frequency is clearly observed between 1048 and 1200 UT. Figure 7.9 shows FDTD results derived from a cavity with a realistic conductivity calculating from IRI model. A jump of the first peak frequency is also clearly observed between 1048 and 1200 UT. We believe that this frequency jump comes from the mode splitting, which is clearly observed in Figure 7.6 (1048 UT and 1200 UT). As shown in Figure 7.6, when the receiver is close to the nodal line, M_1 is much stronger than M_2 at 1048 UT. When the receiver passes the nodal line, the magnitude of M_1 quickly decreases, and M_2 becomes much stronger than M_1. Since one of the splitting modes is much weaker than another one, Pronys method, which we used to find the eigenfrequency of the cavity, can only detect the stronger splitting mode. Therefore, a singularity-like frequency jump appears when the receiver

passes the nodal line. Therefore, we believe that the frequency jump at 1000 UT in Figure 7.3(f) could be produced by Asia lightning, which is located close to the nodal line and active from 0500 to 1000 UT. All of the features of frequency variations during different seasons, which are shown in Figures 7.2 and 7.3 can be also found in the experimental measurements reported by *Ondrášková et al.* [2007]. In particular, in Figure 3 of [*Ondrášková et al.*, 2007], from June to September when African lightning reach maximum, a frequency peak appears at 1000 UT consistent with the data shown in Figure 7.4. From November to March when Asian lightning becomes the strongest one, the frequency decreases from 0000 to 1000 UT, and a singularity-like frequency jump appears around 1000 UT, then reaches the maximum value around 1500 UT.

7.3 Summary

The main conclusions in this Chapter can be summarized as follows:

• A genetic algorithm (GA) optimization method has been employed to inversely calculate the intensity of lightning activity in Asia, Africa, and America using the experimental H_{NS} component of the first SR mode. The simulated lightning distributions in three regions are in a good agreement with OTD measurements in May and October. In contrast to OTD data, Asian lightning activity is found to be the most intensive one in January.

• The SR frequency variation depends on the distributions of the lightning activity in the three lightning centers. Due to the positions with respect to the observing station and their seasonal variations, the three lightning centers make different contributions to the frequency variations. The difference between the frequency

variation detected during Summer and Winter comes from the fact that the lightning activity in Africa and Asia becomes the dominant one in Earth-ionosphere cavity during Summer and Winter, respectively.

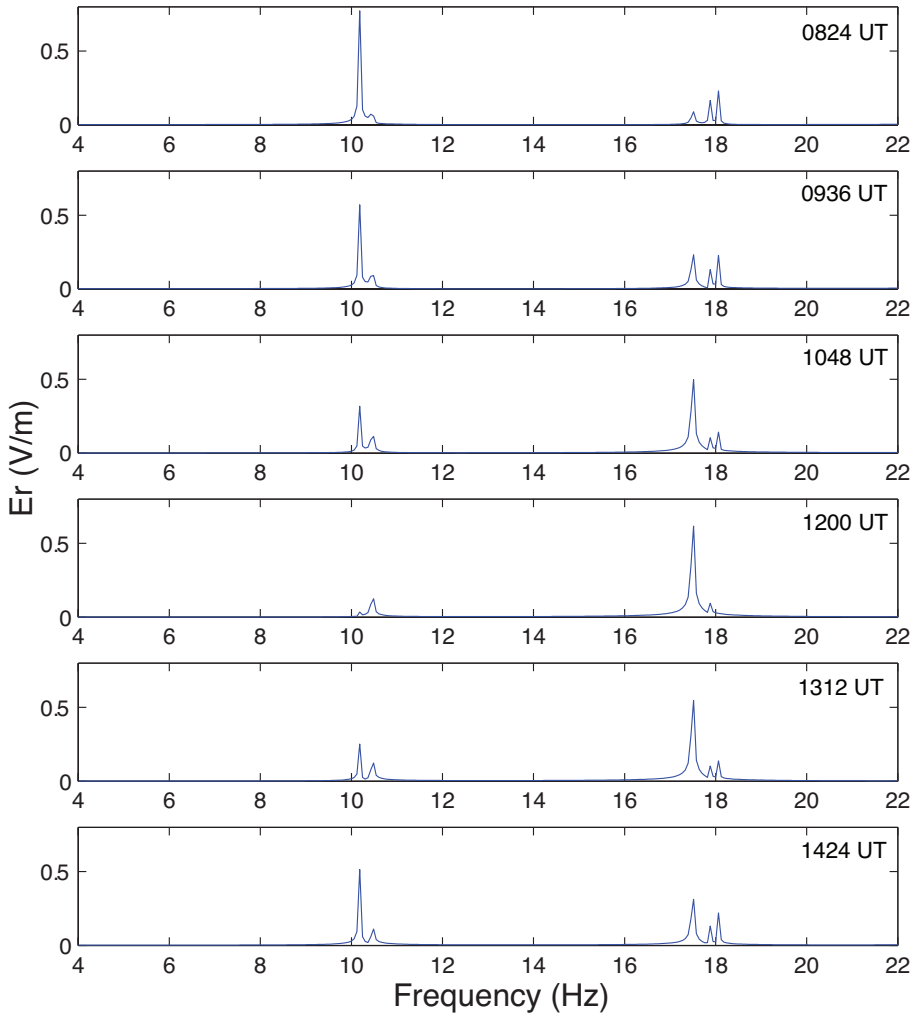

Figure 7.6. FDTD results derived from an artificially asymmetric cavity shown in Figure 7.5 without conductivity inside the cavity. A single source (3000 km by 3000 km) moves around the Earth on the equator synchronized with the motion of the day-night terminator, and is always activated in regions corresponding to local afternoon in the cavity.

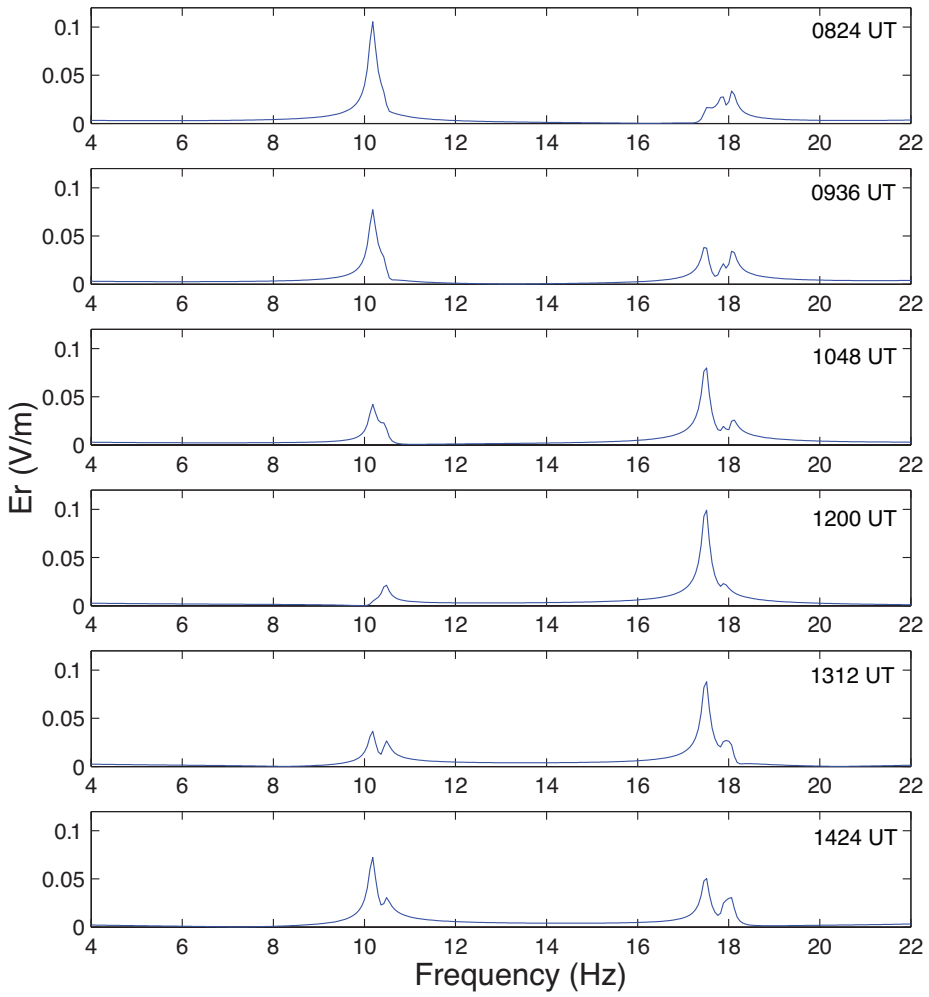

Figure 7.7. The same as Figure 7.6. Only for conductivity = 8×10^{-12} S/m in the cavity.

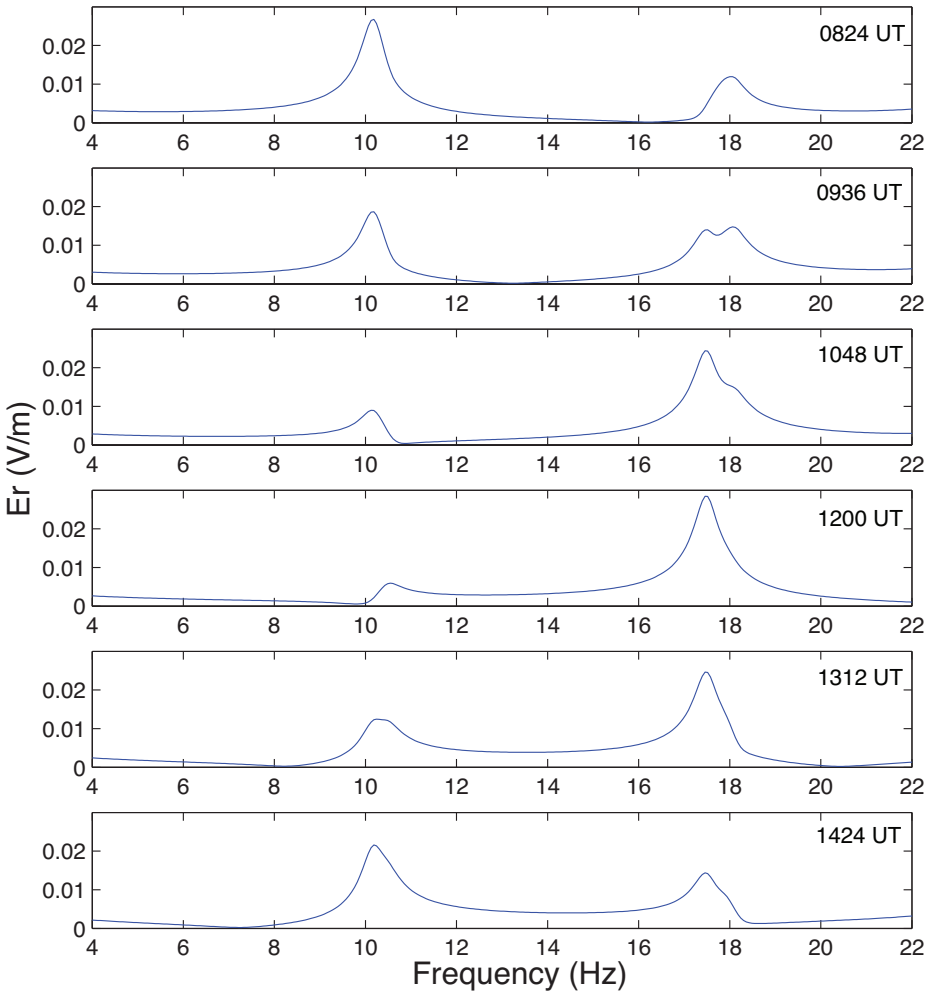

Figure 7.8. The same as Figure 7.6. Only for conductivity $= 3 \times 10^{-11}$ S/m in the cavity.

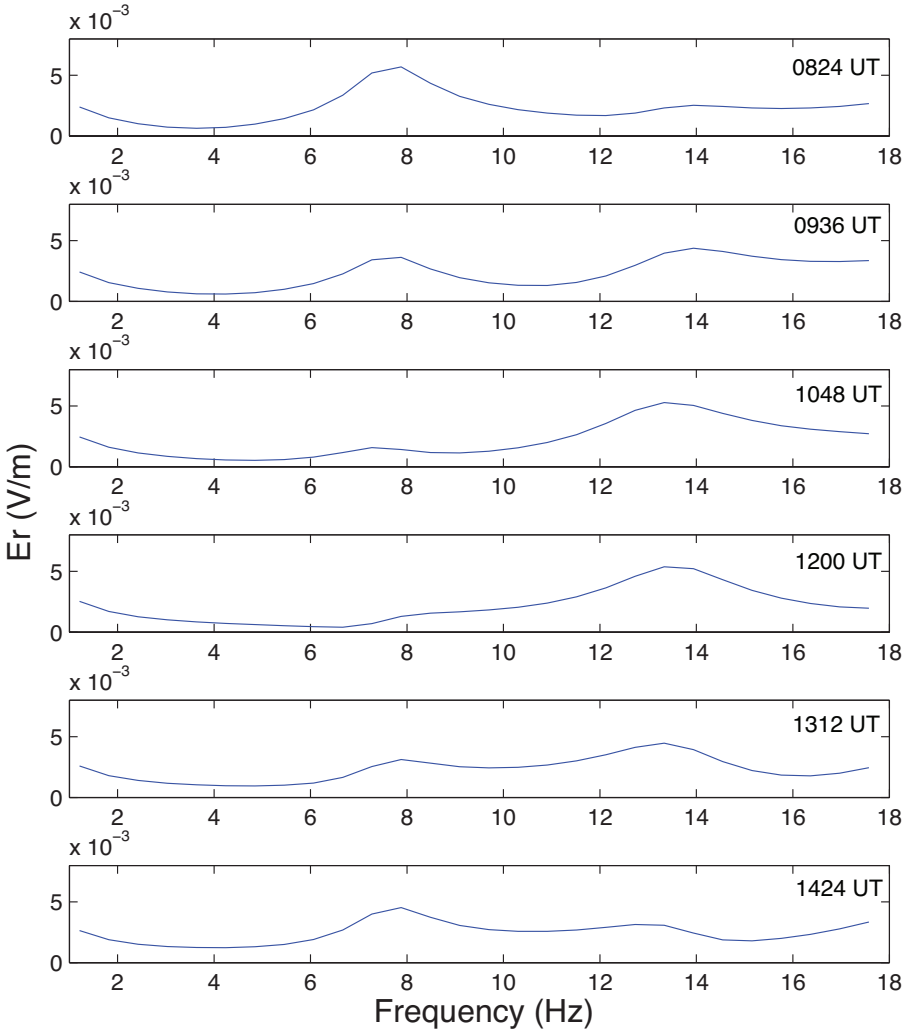

Figure 7.9. The same as Figure 7.6. Only for conductivity derived from International Reference Ionosphere model.

Chapter 8

FDTD Modeling of Earth-Ionosphere Cavity With the Presence of the Geomagnetic Field

8.1 The dynamics of Electrons in the Magnetic Field and Collision Processes

In the FDTD models applied in the previous Chapters, an isotropic conductivity profiles are employed. In the realistic case, the electrons and ions in the ionosphere drift and rotate with the addition of the geomagnetic fields leading to an anisotropic conductivity in the ionosphere. The fluid equation describing the plasma's response to the given electric ($\vec{E}$) and magnetic ($\vec{B}$) field is given by [e.g., *Chen*, 1984, pp. 63]:

$$nm\left[\frac{\partial \vec{v}}{\partial t} + (\vec{v}\cdot\vec{\nabla})\vec{v}\right] + nm\nu\vec{v} = nq\vec{E} + nq\vec{v}\times\vec{B} - \vec{\nabla}p \tag{8.1}$$

where n is the density of fluid particles and $\vec{v}$ is the velocity of the particles. The mass and charge of the particle in the plasma are given by m and q, respectively. The collision frequency is given by ν, and p indicates the pressure. Assuming that there are no thermal motions, and all particles in the fluid element move together with the same average velocity, the equation (8.1) can be rewritten in the single particle form:

$$m\frac{\partial \vec{v}}{\partial t} + m\nu\vec{v} = q\vec{E} + q\vec{v} \times \vec{B} \tag{8.2}$$

Assuming the particles in plasma are electrons with mass (m_e) and charge (q_e), the current density ($\vec{J}$) corresponding to the motion of electrons is expressed by $\vec{J} = N_e q_e \vec{v}$, where N_e is the number density of electrons. The current density equation is derived by multiplying both sides of equation (8.2) by $N_e q_e$:

$$\frac{d\vec{J}}{dt} - \frac{q_e}{m_e}\vec{J} \times \vec{B} + \nu_e \vec{J} = \frac{N_e q_e^2}{m_e}\vec{E} \tag{8.3}$$

where ν_e is the electronic collision frequency. The problem is solved in a 2D domain. In tests presented below, we assume that only E_x and B_z components exist in our FDTD simulations, so the rotation and drift of the electrons driven by these two field components can be clearly observed in xy plane. The equation (8.3) can be simplified in a 2D domain as following:

$$\begin{aligned} \frac{dJ_x}{dt} &= -\nu_e J_x + \frac{q_e B_z}{m_e} J_y + \frac{N_e q_e^2}{m_e} E_x \\ \frac{dJ_y}{dt} &= -\nu_e J_y - \frac{q_e B_z}{m_e} J_x \end{aligned} \tag{8.4}$$

The J_x and J_y are both equal to zero when $t = 0$. The equation (8.3) can be solved analytically. The solution for J_x and J_y are represented as following:

$$J_x = \left[\frac{\nu_e}{\nu_e^2+\omega_c^2}e^{-\nu_e t}\cos(\omega_c t) - \frac{\omega_c}{\nu_e^2+\omega_c^2}e^{-\nu_e t}\sin(\omega_c t) - \frac{\nu_e}{\nu_e^2+\omega_c^2}\right]\frac{E_x}{B_z}N_e q_e \omega_c \quad (8.5)$$
$$J_y = \left[\frac{\nu_e}{\nu_e^2+\omega_c^2}e^{-\nu_e t}\sin(\omega_c t) + \frac{\omega_c}{\nu_e^2+\omega_c^2}e^{-\nu_e t}\cos(\omega_c t) - \frac{\omega_c}{\nu_e^2+\omega_c^2}\right]\frac{E_x}{B_z}N_e q_e \omega_c$$

where ω_c is the cyclotron frequency of electrons, which is equal to $\frac{|q_e|B_z}{m_e}$. The E_x and B_z components are set as 10^{-4} V/m and 3×10^{-5} T, respectively. Two different kinds of components can be found in equations (8.5). The first two terms of J_x and J_y in equations (8.5) are time varying components with the frequency of ω_c and a damping factor $e^{-\nu_e t}$. Both these two terms correspond to the rotation of electrons under the influence of the magnetic field. The last term of J_x and J_y can be considered as a DC component, which corresponds to the $\vec{E} \times \vec{B}$ drift of electrons. When the collision frequency is not equal to zero, the electronic rotation is attenuated with time due to the energy loss by the collisions between electrons and neutral particles, and J_x and J_y converge to their DC values due to the $\vec{E} \times \vec{B}$ drift of electrons. From equations (8.5), we can observe that the collision frequency plays a very important role in the solution, since it determines not only the attenuation rate of the rotations, but also drift and rotation velocities in x and y directions. In the following discussion, the influence of this parameter (ν_e) will be discussed in detail.

In the case of $\nu_e \ll \omega_c$, which corresponds to a low-collision model, the equations (8.5) can be reduced to

$$J_x = -\sin(\omega_c t)\frac{E_x}{B_z}N_e q_e e^{-\nu_e t} \quad (8.6)$$

$$J_y = \left[\cos(\omega_c t)\frac{E_x}{B_z}e^{-\nu_e t} - \frac{E_x}{B_z}\right] N_e q_e$$

The electrons rotate in the xy plane with the cyclotron frequency of ω_c. The magnitude of the rotation velocity is $\frac{E_x}{B_z}$ at $t \ll \frac{1}{\nu_e}$. Due to the existence of the electric field $\vec{E}$, the electrons also undergo the $\vec{E} \times \vec{B}$ drift in $-y$ direction with a velocity of $\frac{E_x}{B_z}$. When $t \gg \frac{1}{\nu_e}$, the rotation disappears and electrons only move in $\vec{E} \times \vec{B}$ direction.

In the case of the high collision frequency between electrons and neutral gas particles ($\nu_e \gg \omega_c$), the motion of electrons can be described by equations (8.7) shown here. When $t \ll \frac{1}{\nu_e}$, electrons rotate under influence of B_z field, and the magnitude of their rotation velocity is less than that in the low collision case by a factor of $\frac{\omega_c}{\nu_e}$.

$$\begin{aligned} J_x &= \left[\frac{1}{\nu_e}e^{-\nu_e t}\cos(\omega_c t) - \frac{1}{\nu_e}\right]\frac{E_x}{B_z}N_e q_e \omega_c \\ J_y &= \left[\frac{1}{\nu_e}e^{-\nu_e t}\sin(\omega_c t)\right]\frac{E_x}{B_z}N_e q_e \omega_c \end{aligned} \tag{8.7}$$

When $t \gg \frac{1}{\nu_e}$, the electronic rotation is reduced to a negligible level, and only drift velocities can be clearly observed. Therefore, J_x and J_y components can be derived from equations (8.7) as following when $\nu_e \gg \omega_c$ and $t \gg \frac{1}{\nu_e}$:

$$\begin{aligned} J_x &= -\frac{\omega_c}{\nu_e}\frac{E_x}{B_z}N_e q_e \\ J_y &= 0 \end{aligned} \tag{8.8}$$

From equations (8.8), J_x and J_y can be further simplified by replacing ω_c with

$\frac{|q_e|B_z}{m_e}$:

$$J_x = -\frac{\omega_c}{\nu_e}\frac{E_x}{B_z}N_e q_e = -\frac{|q_e|B_z}{m_e\nu_e}\frac{E_x}{B_z}N_e q_e = \frac{q_e^2 N_e}{m_e\nu_e}E_x = \sigma_e E_x \qquad (8.9)$$
$$J_y = 0$$

where $\sigma_e = \frac{q_e^2 N_e}{m_e\nu_e}$ is the electronic conductivity of the plasma. In the high collision case, the influence of collisions between electrons and neutral gas particle becomes more significant than the magnetic field. The plasma behaves as an isotropic conducting material with electronic conductivity σ_e. Same conclusion can be derived from equation (8.3). When ν_e is high enough, the terms $\frac{d\vec{J}}{dt}$ and $\frac{q_e}{m_e}\vec{J}\times\vec{B}$ are much smaller than $\nu_e\vec{J}$ and can be neglected. Therefore equation (8.3) can be rewritten giving the same result as specified by equations (8.9):

$$\nu_e\vec{J} = \frac{N_e q_e^2}{m_e}\vec{E} \qquad (8.10)$$

In the case when the collision frequency is comparable to the cyclotron frequency of electrons ($\nu_e \simeq \omega_c$), the equations (8.5) can not be simplified. The rotation and drift of electrons can be simultaneously found in the motion of electrons at $t \ll \frac{1}{\nu_e}$. The rotation is attenuated with the growing time and the speed of the attenuation is dependent on the value of collision frequency. The drift velocities in x and y directions are comparable, and are determined by both ν_e and ω_c. In this case, J_x and J_y are directly provided by more general equations (8.5).

A two dimensional FDTD model is developed to solve the problem in equation (8.3) numerically. The 2D FDTD equations in the rectangular coordinates (x and y) are derived from equations (8.4). The cell size of this 2D FDTD model is chosen

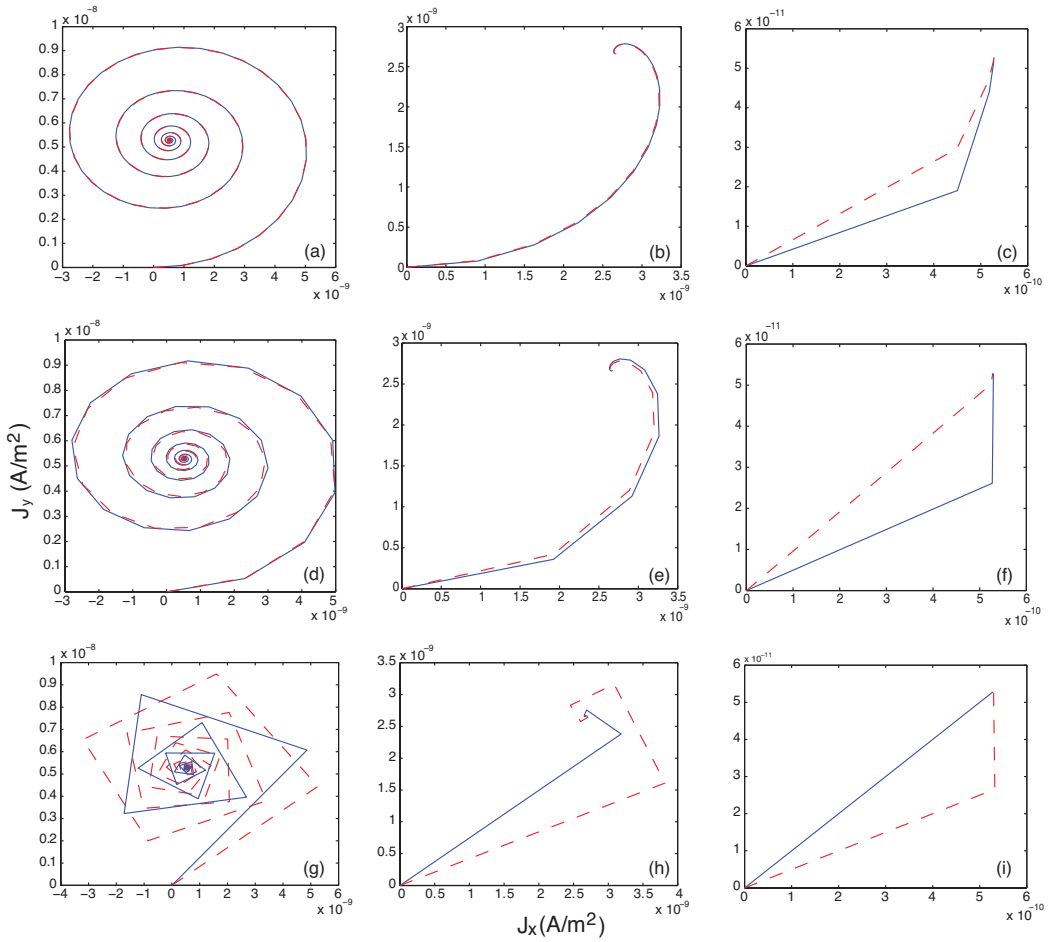

Figure 8.1. The current densities obtained using FDTD model with different collision frequencies and time steps.

to be the same as employed in our 3D FDTD modeling for testing and comparison. The numbers of FDTD cells in x and y directions are 100 and 100, respectively. Each cell has shape of a rectangle with a size of 1000 km $\times$ 1000 km which is comparable to the value we used in our 3D FDTD Earth-ionosphere cavity model. The $\vec{E}$ and $\vec{B}$ components are set along x and z directions with the magnitude of 10^{-4} V/m and 3×10^{-5} T, respectively. The cyclotron frequency, ω_c, is equal to $\frac{|q_e|B_z}{m_e} = 5.26 \times 10^6\ rad/s$. The number density of electrons is $N_e = 10^{10}\ m^{-3}$ which is comparable with the ionospheric electron density at the altitude of 100

km. The time step (Δt) is derived using Courant condition [*Taflove and Hagness*, 2000]. According to Courant condition, in a vacuum, the stability condition of the FDTD method is given by:

$$\Delta t < \Delta t_c = \frac{1}{c}\left[\frac{1}{(\Delta x)^2} + \frac{1}{(\Delta y)^2}\right]^{-1/2} \tag{8.11}$$

where Δt_c is the maximum time step of FDTD stability, Δx and Δy are the space steps applied in FDTD simulations and c is the speed of light. In a plasma with free electrons, the stability criterion differs from that given in equation (8.11), and is given by:

$$\Delta t < \Delta t_c = \frac{1}{c}\left[\frac{1}{(\Delta x)^2} + \frac{1}{(\Delta y)^2} + \frac{\mu_0 N_e q_e^2}{4m_e}\right]^{-1/2} \tag{8.12}$$

If the value of N_e is big enough, the FDTD time step in plasma (Δt) is mainly determined by N_e. Equation (8.12) can be rewritten as following:

$$\Delta t < \Delta t_c = \left[\frac{\mu_0 N_e q_e^2}{4m_e \varepsilon_0}\right]^{-1/2} = \frac{1}{\pi f_p} \tag{8.13}$$

Where f_p is the plasma frequency. The maximum time step of FDTD stability (Δt_c) can be derived from equation (8.13), and is equal to 3.55×10^{-7} s. The purpose of this section is to find whether the FDTD model properly describes the motion of electrons with the presence of the geomagnetic field. Three different time steps ($\Delta t = 0.1\Delta t_c$, $0.5\Delta t_c$, $0.99\Delta t_c$)and collision frequencies ($\nu_e = 0.1\omega_c$, ω_c, $10\omega_c$) are employed to study there parametric influence on FDTD results.

The time step applied in Figures 8.1(a-c) is equal to $0.1\Delta t_c$. The comparison of the analytical solution derived from equations (8.5) and FDTD results are shown in Figures 8.1(a-c) with different collision frequencies ($\nu_e = 5.26 \times 10^5$, 5.26×10^6,

and 5.26×10^7 $1/s$) corresponding to the cases of $\nu_e \ll \omega_c$, $\nu_e \simeq \omega_c$, and $\nu_e \gg \omega_c$, respectively. The analytical solution and FDTD results are shown by solid and dashed lines, respectively. When $\nu_e \ll \omega_c$ ($\nu_e = 5.26 \times 10^5$ $1/s$), the rotation of electrons can be clearly observed in Figure 8.1(a). J_x and J_y are slowly attenuated due to the small value of the collision frequency. Since the attenuation factor of the rotation is $e^{-\nu_e t}$, the amplitude of the rotation velocity is reduced to $1/e$ times of its original value in $1/\nu_e$ (1.9×10^{-6} second). At least 5 obvious circles of the electronic rotation can be found in Figure 8.1(a). Calculated using equations (8.5), J_x and J_y components converge to 5.28×10^{-10} and 5.28×10^{-9} A/m^2, respectively. In the case of $\nu_e = \omega_c$ (shown in Figure 8.1(b)), the electron collides neutral gas particle once per period. J_x and J_y decay more rapidly in comparison with results of Figure 8.1(a). The electron can only rotate one circle before J_x and J_y become constant. The constant current densities in x and y directions are 2.67×10^{-9} and 2.67×10^{-9} A/m^2, respectively. When $\nu_e \gg \omega_c$ ($\nu_e = 5.26 \times 10^7$ $1/s$), the rotation is strongly attenuated due to the high collision frequency. There is no obvious rotation observed.

Comparing Figures 8.1(a-c), the different influences of the collision between electrons and neutral gas and the magnetic field on the motion of electrons are clearly found. In a non-collision case, electrons only drift along $\vec{E} \times \vec{B}$ $(-y)$ direction with the velocity of E_x/B_z simultaneously with the rotation in xy plane, and there is no drift of electrons in x direction. The collision process has much weaker influence on the electronic motion than the magnetic field when $\nu_e \ll \omega_c$. The velocity in $\vec{E} \times \vec{B}$ $(-y)$ direction is almost as same as E_x/B_z. With increasing of the collision frequency, the effect of collision processes becomes stronger. The electronic rotation attenuates more rapidly. The $\vec{E} \times \vec{B}$ drift velocity becomes smaller and the velocity in x direction increases. In Figure 8.1(b) ($\nu_e = \omega_c$), the

J_x and J_y already have similar magnitudes. If ν_e is further increased, the collision process has amore significant influence at the motion than the magnetic field. In Figure 8.1(c) ($\nu_e \gg \omega_c$), electrons move almost along the direction of $\vec{E}$ (x), and J_x component is one order of magnitude stronger than the J_y component. In this case, the plasma becomes an isotropic conducting material with the conductivity (σ_e) and current density $\vec{J}$, which can be obtained using equations (8.9). Concluding above discussions, the collision frequency determines the attenuation rate of the electronic rotations. Moreover, the collision frequency can also control electronic drift velocities in different directions. With the small collision frequency, electrons drift in $\vec{E} \times \vec{B}$ direction more rapidly than in $\vec{E}$ direction. With increasing collision frequency, the velocity in $\vec{E}$ direction becomes stronger with respect to that in $\vec{E} \times \vec{B}$ direction. The total velocity is dominated in the $\vec{E}$ direction when $\nu_e \gg \omega_c$. Furthermore, we can also find that FDTD results match the analytical solutions very well. FDTD modeling produces accurate rotation and drift current densities in Figures 8.1(a-b). Although a difference is found at the beginning of the simulations between FDTD and analytical solutions, accurate drift current densities are rapidly achieved by FDTD model in Figure 8.1(c).

In Figures 8.1(d-f), Δt is increased to $0.5\Delta t_c$. the results shown in figures 8.1(d,e,f) correspond to the cases of $\nu_e = 0.1\omega_c, \omega_c, 10\omega_c$, respectively. Although, at the beginning of the motion of electrons, the errors between FDTD and analytical solutions increase during electronic rotations, both J_x and J_y components derived from the FDTD model converge to the analytical solutions, after the rotations disappear due to the collisions between electrons and neutral gas particles. With increasing Δt to $0.99\Delta t_c$ (shown in Figures 8.1(g-i)), the errors between analytical and FDTD results during electronic rotations become more obvious. However, the analytical and FDTD results still correctly converge to same DC value.

The purpose of this section is to investigate if our FDTD model can correctly model Schumann resonance frequencies and Q-factors with the presence of the geomagnetic field. The FDTD model parameters are chosen to be the same as what we used in our 3D FDTD simulations. Since the cyclotron frequency in this case is 8.4×10^5 Hz, which is much greater than Schumann resonance frequencies we are interested in, the rotation of electrons with the presence of geomagnetic fields does not make a direct distribution to the properties of Schumann resonances. Although phase errors in FDTD simulations increase with the time step during the electronic rotations, they do not influence the frequencies and Q-factors of Schumann resonances.

The DC component of the current density due to the drift of electrons is a very important factor to determine the total energy dissipation in the cavity in Schumann resonance frequency band, especially above 70 km where the ionosphere becomes anisotropic. Whether our FDTD model can accurately produce the DC current component is very important for the correct calculation of the energy dissipation in the whole cavity and Schumann resonance parameters. Figure 8.1 demonstrates that although the errors increase with time steps during the electronic rotations, there is a good agreement between the DC components of analytical solution and FDTD results indicating that the drifts of electrons with presence of the magnetic field and collision processes are accurately described by the FDTD model.

8.2 FDTD Model With Zero Geomagnetic Field Model

In this Chapter, the number of FDTD cells in r, θ and ϕ directions are 20, 20 and 40, respectively. Two kinds of geomagnetic field model are employed. The first one is simply $\vec{B} = 0$. The FDTD scheme discussed in section 2.2.2 is applied. The electron and ion densities (N_e and N_i), and their collision frequencies (ν_e and ν_i) with the neutral gas particles have been given in Section 2.3.3. Figure 8.2 shows the vertical distributions of the E_r, E_θ, and H_ϕ field components corresponding to the first SR mode, which are excited by a vertical current source, in the Earth-ionosphere cavity with zero geomagnetic field. The E_r and H_ϕ components are normalized to 1 at the ground level. The E_r component remains constant below 50 km, and drops exponentially above 50 km. The horizontal electric field component, E_θ, increases from zero at the ground, and reaches the maximum at 50 km. The H_ϕ component remains constant until the altitude of 90 km, and starts to decay exponentially above this altitude. In the region above 100 km, the magnitude of these three components decreases exponentially with the same rate.

The results shown in Figure 8.2 can be interpreted following ideas presented in [*Sentman*, 1983] based on introduction of a conducting boundary defined by a condition, $\sigma = \omega\varepsilon_0$, where ω is a specific frequency. The atmosphere is divided by this conducting boundary into two altitude regions dominated by displacement (below it) and conduction (above it) currents, respectively. For this case, the first SR frequency is approximately 7.5 Hz, so the conducting boundary is at the altitude of 50 km, where $\sigma = 4.2 \times 10^{-10} S/m$. Below 50 km, the electric field is predominantly vertical and its behavior is similar to that in a lossless free space resonator, so the E_r remains constant in this region. Above this boundary, the

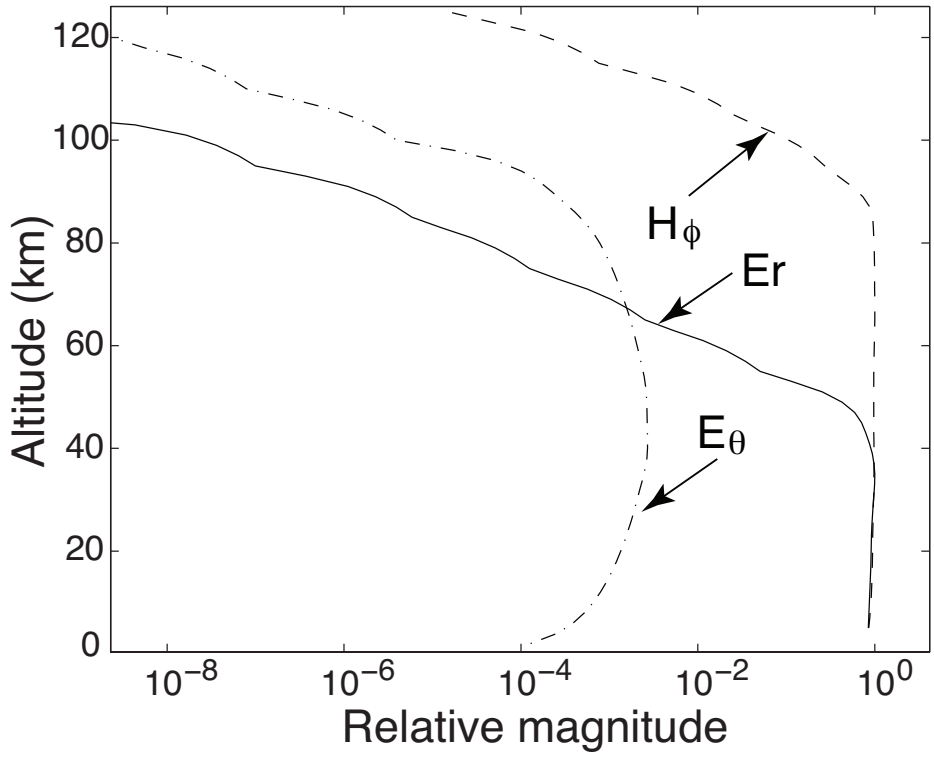

Figure 8.2. The vertical distributions of the E_r, E_θ, and H_ϕ components in the Earth-ionosphere cavity with zero geomagnetic field obtained using the FDTD model.

atmospheric conductivity is large enough to significantly reduce the E_r component, and the vertical component of the field drops exponentially. The E_θ component increases from zero at ground and reaches a maximum at the conducting boundary in agreement of the results derived in [*Greifinger and Greifinger*, 1978]. However, the E_θ component is substantially smaller than the E_r component at this altitude. Since the E_θ component decays with altitude much less rapidly than the E_r component between 50 and 80 km, the electric field becomes predominantly horizontal above 80 km [*Sentman*, 1983]. In [*Greifinger and Greifinger*, 1978], the altitude where the magnetic field can penetrate was defined by a condition of $4\mu_0\omega\sigma\xi^2 = 1$, where ξ is the scale height of the conductivity at this altitude. For the conductivity

profile used, this altitude is approximately at 90 km. This related boundary can be clearly observed in Figure 8.2. Below 90 km, the H_ϕ component remains constant, but falls off exponentially above 90 km.

Because the geomagnetic field is zero in these above simulations, the conductivity profile in the cavity is still spherically uniform. For the ELF waves, the total conductivity profile in the atmosphere (σ) can be derived from the electron and ion densities, and the electron and ion collision frequencies with the neutral gas as following:

$$\sigma = \frac{N_e q_e^2}{m_e \nu_e} + \frac{N_i q_i^2}{m_i \nu_i} \tag{8.14}$$

Some additional simulations have been performed using the FDTD model discussed in Section 2.2.2 with the conductivity profiles derived from N_e, N_i, ν_e, and ν_i using equation (8.14). The obtained results are consistent with those shown in Figure 8.2. We conclude that same results can be derived from two different FDTD models given in Chapter 2 without the presence of the geomagnetic field, if the conductivity, particle densities and collision frequencies satisfy the relation shown in equation (8.14).

8.3 FDTD Model With Dipole Geomagnetic Field Model

The FDTD simulation results including a dipole geomagnetic field are presented in Figures 8.3 and 8.4. In this case, the E_ϕ and H_θ components are also excited by a vertical current source. All five components shown in Figures 8.3 and 8.4 are collected at the location where the latitude is equal to $18^o N$. Figure 8.3 illustrates the vertical distributions of three electric field components (E_r, E_θ, and E_ϕ). Some

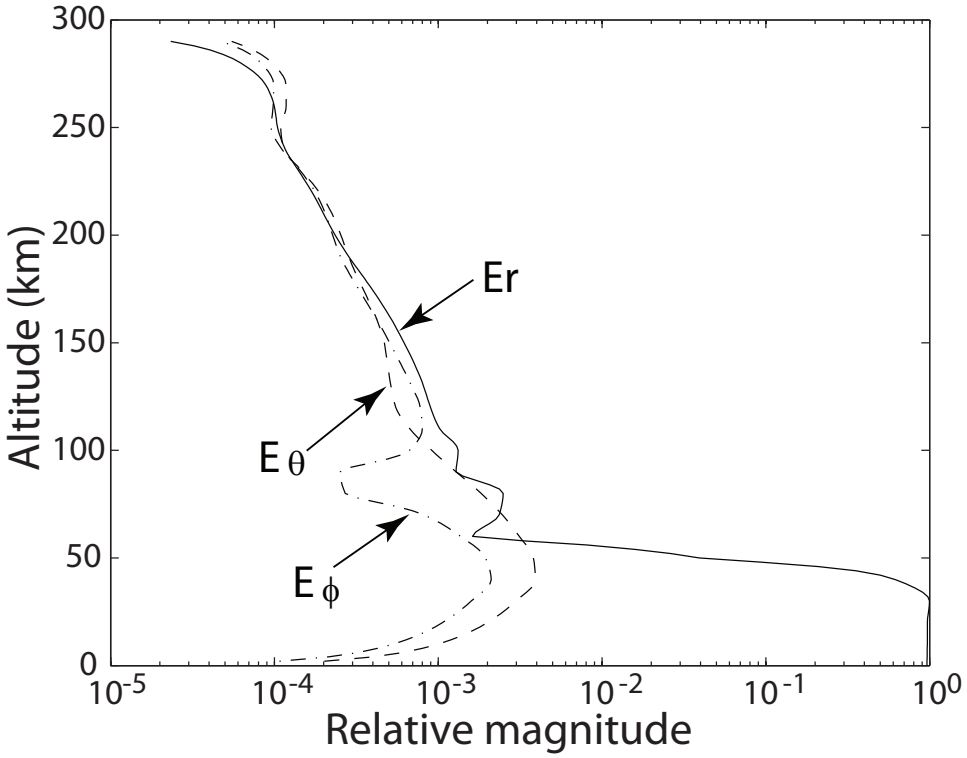

Figure 8.3. The vertical distributions of the E_r, E_θ, and E_ϕ components in the Earth-ionosphere cavity with the presence of the dipole geomagnetic field.

features of the E_r and E_θ components are similar to these shown for the same field components in Figure 8.2 below 70 km. The magnitude of the E_r component remains constant below 50 km, and drops exponentially above the altitude of 70 km. The E_θ component increases from zero at ground level and reaches the peak at 50 km. However, above 70 km, the attenuation rates of these two components with altitude become much smaller than those shown in Figure 8.2. Therefore, the E_r and E_θ components can penetrate to higher altitudes with the presence of the geomagnetic field. For the magnetic components, H_θ and H_ϕ (shown in Figure 8.4), the field magnitude of H_ϕ component remains constant and begins to fall off above the altitude of 90 km. However, the attenuation rate above 90 km is smaller than that in Figure 8.2.

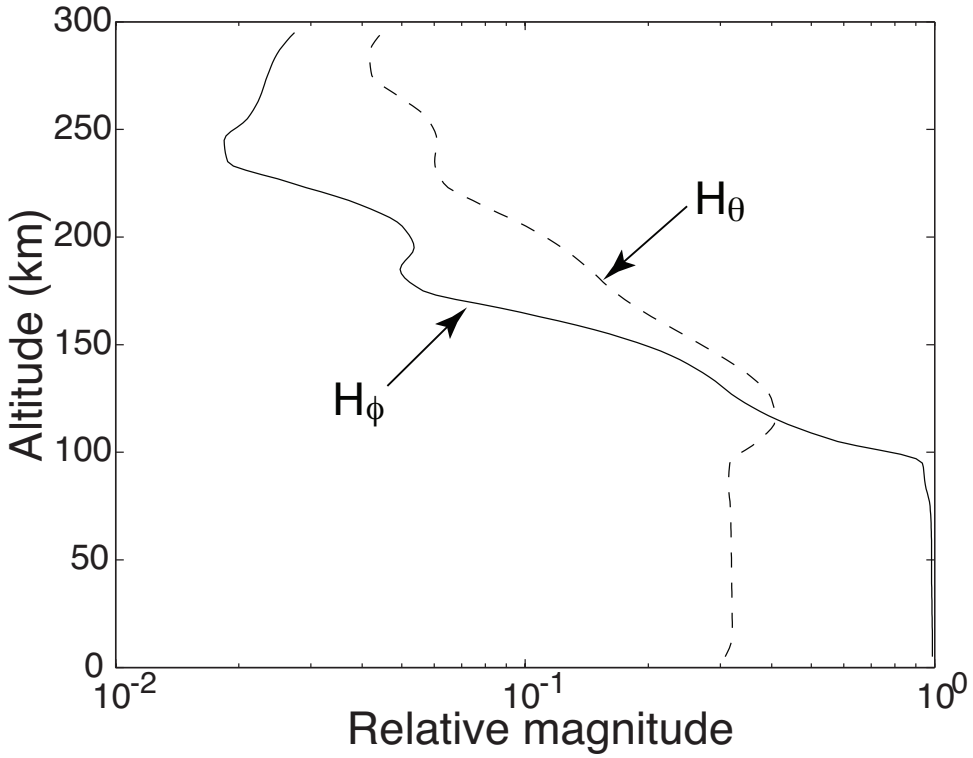

Figure 8.4. The vertical distributions of the H_θ, and H_ϕ components in the Earth-ionosphere cavity with the presence of the dipole geomagnetic field.

The variation of the penetration heights of the five wave components as a function of latitude is presented in Figures 8.5, 8.6 and 8.7. The latitude of the observation point obviously affects the penetration height of all the components. For E_r component, the penetration height in the low latitude region is much higher than that in the polar region. Figures 8.6 and 8.7 show the comparison of the vertical field profiles of other four horizontal components at different latitudes. Unlike the E_r component, the magnitude of these four components decreases rapidly above 70 km in the equatorial region, but much more slowly in the high latitude regions.

In Figures 8.2, 8.3, and 8.4, some similar features can be observed in the modeling results with and without the geomagnetic field in the region below 70 km. For example, the E_r component in Figure 8.3 begins to fall off at 50 km, and drops

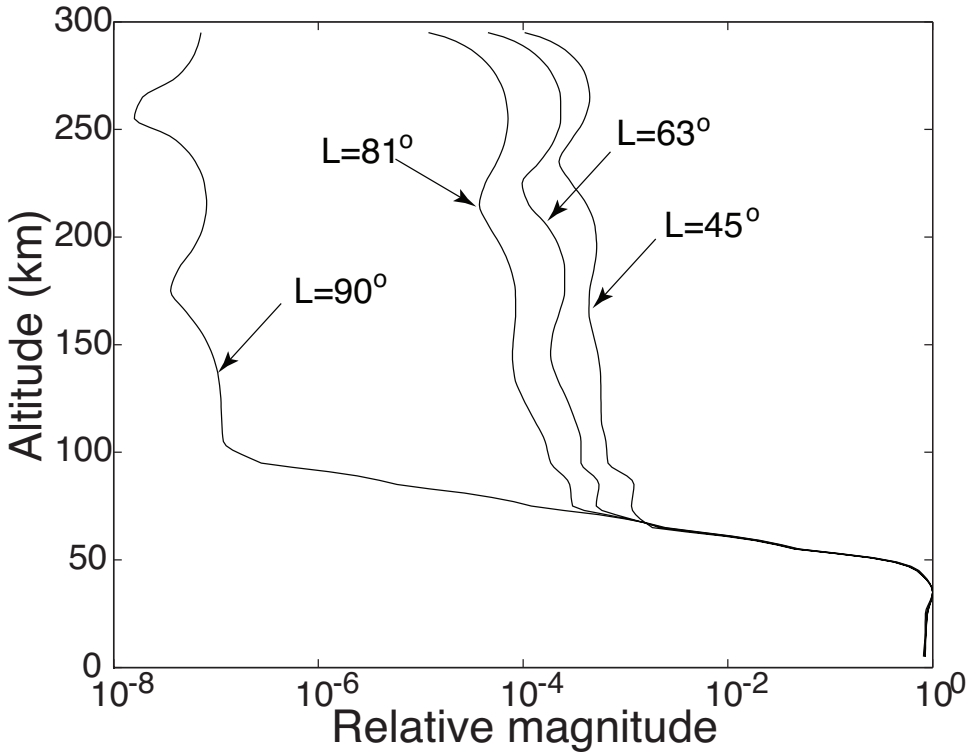

Figure 8.5. The vertical distributions of the E_r component in the Earth ionosphere cavity with the presence of the dipole geomagnetic field. L indicates the latitude of the different observation points.

to 10^{-3} at about 70 km, which is in agreement of the results shown in Figure 8.2. Moreover, the E_θ component (shown in Figure 8.3) also reaches the maximum at 50 km, and the H_ϕ component remains constant below 70 km. In the region above 70 km, the E_r and E_θ components still decrease, but not as rapidly as in Figure 8.2. In Figure 8.2, the relative magnitude of the E_r and H_ϕ components can be found decreasing to 10^{-5} at 80 and 120 km, respectively. However, in Figures 8.3 and 8.4, the relative magnitude of the E_r component becomes 10^{-5} at 200 km and H_ϕ drops to 10^{-3} at 290 km. Therefore, we conclude that the geomagnetic field plays a significant role above about 70 km in the atmosphere, but its effects are not important below 70 km. The vertical distributions of the electric and mag-

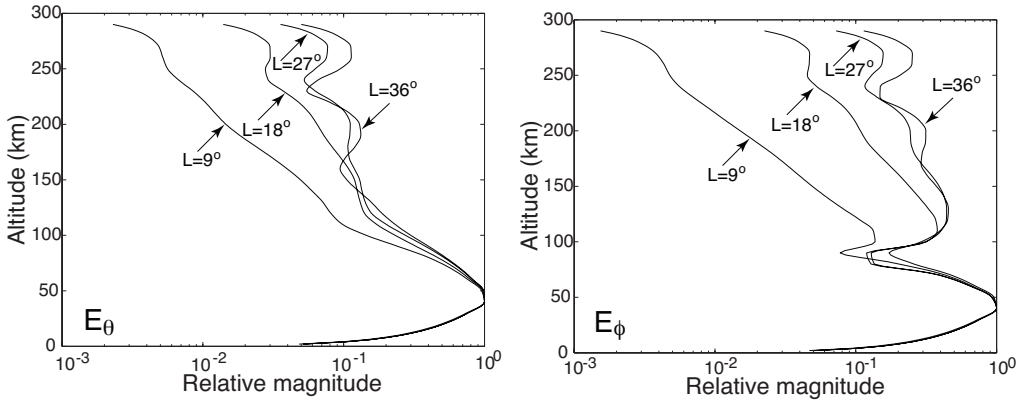

Figure 8.6. The vertical distributions of the E_θ, and E_ϕ components in the Earth ionosphere cavity with the presence of the dipole geomagnetic field at different latitude. (L indicates the latitude of the different observation points)

netic fields are significantly modified by the geomagnetic field in the region above 70 km, and the attenuation rates of these fields with altitude are much smaller than these in the model cavity without the geomagnetic field. Therefore, the electric and magnetic fields can penetrate to higher altitudes in the presence of the geomagnetic field. Another point we want to note here is that the three electric components (shown in Figure 8.3) and two magnetic components (shown in Figure 8.4) have almost same attenuation rates with altitude. Moreover, the E_r becomes of the same order as the E_θ and E_ϕ above 100 km. All of these features can be found to be good agreement with previously results reported in [*Grimalsky et al.*, 2005].

In [*Grimalsky et al.*, 2005], a dependence of the penetration height of the H_ϕ and H_θ components of the first SR mode on the inclination angle of the geomagnetic field, Θ, has been discussed, where Θ indicates the angle between the direction of the geomagnetic field and the direction vertical to the ground. It has been concluded that the penetration heights of these two magnetic components increase with decreasing Θ [*Grimalsky et al.*, 2005]. Additional simulations have been

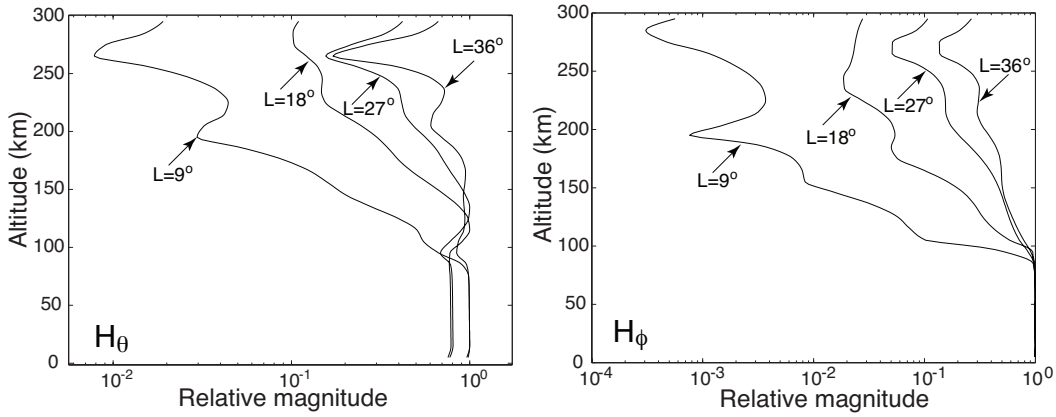

Figure 8.7. The vertical distributions of the H_θ, and H_ϕ components in the Earth-ionosphere cavity with the presence of the dipole geomagnetic field. L indicates the latitude of the different observation points.

performed here to provide additional insight on this point and the corresponding results are shown in Figures 8.5-8.7. Since a magnetic dipole model is employed to account for the geomagnetic field in the Earth-ionosphere cavity, the inclination angle of the geomagnetic field is dependent on the latitude of the observation positions. Near the equator, the geomagnetic field points preferentially in the θ (north-south) direction, so that Θ is close to 90^o, whereas Θ is close to 0^o in the polar regions. In the simulations, several receivers are located at different latitudes to collect the H_ϕ and H_θ components. Results shown in Figure 8.6 clearly indicate that these two magnetic components can penetrate to higher altitude in high latitude regions in comparison with the equatorial region. The penetration heights of the E_θ and E_ϕ components are also illustrated in Figure 8.6. Similarly to the H_ϕ and H_θ components, they can penetrate to higher altitudes at higher latitude locations.

For the E_r component, the penetration height is different from other four components discussed above. In Figure 8.5, the vertical field profiles of the E_r component are collected at four different locations. With increasing the latitude, the

Mode number (n)	FDTD results with the geomagnetic field		FDTD results without the geomagnetic field	
	f_n	Q_n	f_n	Q_n
1	7.3	4.8	6.8	3.8
2	13.1	5.4	12.4	4.4
3	18.8	6.0	18.1	5.2

Table 8.1. The first three SR frequencies and Q factors derived from the FDTD model with and without the geomagnetic field.

penetration height of the E_r component decreases, and at the pole ($L = 90^o$) the E_r component undergoes the same vertical variation as that in the case without the geomagnetic field (shown in Figure 8.2). The SR frequencies are much lower than the electron cyclotron frequency in the geomagnetic field, so E_r is essentially static and only $\vec{E} \times \vec{B}$ drift of electrons is observed. Near the equator, the geomagnetic field is mostly directed in θ direction. Obviously, the electrons do not move in the r direction driven by a vertical electric field, but in the $\vec{E} \times \vec{B}$ direction, which leads to the decrease of the conductivity in the r direction. Therefore, the E_r component can penetrate to a higher altitude than that in the case without the geomagnetic field. In the polar regions, the geomagnetic field concentrates in r direction, and the electrons can easily move along the geomagnetic field line driven by a vertical electric field without any effects of the geomagnetic field. Therefore, the atmospheric conductivity in the r direction is not affected by the geomagnetic field, and the vertical field profile at the poles is similar to that in the case without the geomagnetic field (shown in Figure 8.2).

Another important point we discuss here is the influence of the geomagnetic field on the SR frequency and Q-factor. As discussed in [*Yang and Pasko*, 2005], the ionospheric conductivity enhancement associated with X-ray bursts makes the ionospheric medium above 70 km a better conductor, therefore providing a better reflection of the electromagnetic energy back into the cavity. The decrease of the

total energy dissipation leads to the increase of the SR frequency and Q-factor. Here, the situation is opposite. The ionospheric conductivity decreases due to the geomagnetic field, especially above 70 km, and the medium in this region becomes effectively less conducting. The electromagnetic waves can penetrate to higher altitude, and the whole resonant system will suffer more energy dissipation. Therefore, the associated decrease of SR frequencies and Q factors are expected. Table 8.1 gives the comparison of the first SR frequencies and Q -factors derived from the FDTD models with and without the geomagnetic field. For the specific electron density profile employed here, the SR frequencies are lower than the results shown in [*Yang and Pasko*, 2005]. In the presence of the geomagnetic field, the first SR frequency decreases from 7.3 Hz to 6.8 Hz. The corresponding Q factor decreases from 4.8 to 3.8. The frequencies and Q-factors of the other two modes show similar treads. Therefore, the presence of the geomagnetic field increases the total energy dissipation in the cavity and decreases the SR frequencies and Q-factors.

8.4 Summary

The main conclusions in this Chapter can be summarized as follows:

• The 3D FDTD model discussed in this Chapter provides a good technique to solve SR problems in the Earth-ionosphere cavity with the presence of the geomagnetic field. Results calculated using two different FDTD models given in Section 2.2 were shown to be same in the case of the zero geomagnetic field, if the conductivity, particle densities, and collision frequencies satisfy the relation shown in equation (8.14).

• The penetration heights of the electric and magnetic fields of the first SR mode are approximately 150 km and 250 km, respectively, and these heights are a function of the latitude of the observation positions due to the distribution of the geomagnetic field in the Earth-ionosphere cavity.

• The higher penetration heights of the electromagnetic fields due to the geomagnetic field increase the total energy dissipation in the cavity, and lead to the decrease of the SR frequencies and Q-factors of the Earth-ionosphere cavity.

Chapter 9

Future Research

The diurnal and seasonal variations of SR parameters in the Earth-ionosphere cavity have been discussed in Chapter 4. Same techniques should be extended to describe similar SR variations appearing on Mars, due to the diurnal change of Martian ionosphere and seasonal variation of the dust storms acting as the sources of SR. Information on diurnal and seasonal variations of ionospheric conductivity on Mars is quite limited at present. The existing radar soundings and occultation measurements of ionospheric electron density profiles under variety quiet and perturbed (i.e., dust storms) conditions published in previous papers can be employed to formulate the most realistic spatial and temporal conductivity distributions in Martian cavity as inputs in our 3D FDTD model.

One of the key goals in the exploration of Mars is detection of underground water in the crust. Water with even a small amount of dissolved solids has an electrical conductivity orders of magnitude higher than dry rock. There have been some publications in refereed scientific literature related to the exploration of underground water on Mars by low-frequency, diffusive electromagnetic methods [*Grimm*, 2001]. *Simpson and Taflove* [2006a] recently proposed a method to locate

anomalous conductivity structures (i.e., major oil deposits) in the Earth crust using ELF radars. The sounding studies of Earth's crust using ELF and VLF radio installation have been reported in [*Velikhov et al.*, 1998; *Bashkuev and Khaptanov*, 2001] based on the magnetotelluric method developed by *Cagniard* [1953], in which the ground impedance was calculated by using the horizontal components of the electric and magnetic fields. It is believed that similar technique can be used to locate the mineral deposits and underground water or ice in Martian crust using artificial ELF/VLF sources or naturally generated lightning. In the future research, a high conductivity region can be placed in Martian crust to account for the underground water or other anomalous conductivity structures in our FDTD modeling. The horizontal electric and magnetic field components are directly available from FDTD simulations. The distribution of unknown materials below Martian surface can be identified by different surface impedances. The perturbation of ELF propagation due to the discontinuity formed by the high-conductivity underground water and low-conductivity Martian crust is another interesting effect which need further investigation.

Some interesting new ULF and ELF magnetic signatures from a terrestrial dust devil have been reported in recent literature. [*Houser and Farrell*, 2003] detected a magnetic emission between 1-50 Hz at a distance of many 100's of meters from a dust devil in Nevada desert. Similar ELF magnetic signatures below 40 Hz are clearly detected when a dust devil approached the receiver in Martian Atmosphere and Dust in the Optical and Radio (MATADOR) project in Arizona desert [*Farrell et al.*, 2004]. Unlike ELF waves produced by electrical discharges in the dust devils, the cause of these waves can be explained by charged grains spiraling in a dust devil driven by cyclonic winds and thus forming a magnetic dipole [*Farrell et al.*, 2006]. These ELF and ULF waves can be applied as a safety alert for detection

of approaching dust devils in future manned and robotic missions [*Farrell et al.*, 2006]. The ELF waves derived from our FDTD model can be used to study the connection between these waves and some parameters of the dust devils (e.g., spiral wind speed and total charge mount).

In this thesis, we discussed the different shifts of the first SR frequency on Earth due to ionospheric perturbations associated with solar proton events and x-ray bursts. Similar SR frequency variations are expected on Mars, Venus, and Titan with some additional factors (e.g., ionospheric heating due to crustal magnetic fields on Mars [*Duru et al.*, 2006], the clouds and aerosols on Venus and Titan [*Borucki et al.*, 1982, 1987]). The corresponding changes in the SR parameters are determined by the spatial distribution of these ionospheric perturbations, therefore providing a possible way to evaluate overall size and altitude of atmospheric regions affected by these factors. The related study of SR parameters on these celestial bodies represents a topic which can be investigated using our 3D FDTD model.

Bibliography

Abbas, M. (1968), Hydromagnetic wave propagation and excitation of Schumann resonances, *Planet. Space. Sci.*, *16*, 831.

Acuña, M., J. Connerney, P. Wasilewski, R. Lin, K. Anderson, C. Carlson, J. McFadden, D. Curtis, D. Mitchell, H. Réme, C. Mazelle, J. A. Sauvaud, C. d'Uston, A. Cros, J. Medale, S. Bauer, P. Cloutier, M. Mayhew, D. Winterhalter, and N. Ness (1998), Magnetic field and plasma observations at Mars: Initial results of the Mars Global Surveyor Mission, *Science*, *279*(5357), 1676.

Acuña, M., J. Connerney, N. Ness, R. Lin, D. Mitchell, C. Carlson, J. McFadden, K. Anderson, H. Réme, C. Mazelle, D. Vignes, P. Wasilewski, and P. Cloutier (1999), Global distribution of crustal magnetization discovered by the Mars Global Surveyor MAG/ER Experiment, *Science*, *284*(5415), 790.

Acuña, M., J. Connerney, P. Wasilewski, R. Lin, D. Mitchell, K. Anderson, C. Carlson, J. McFadden, H. Réme, C. Mazelle, D. Vignes, S. Bauer, P. Cloutier, and N. Ness (2001), Magnetic field of Mars: Summary of results from the aerobraking and mapping orbits, *J. Geophys. Res.*, *106*(E10), 23,403.

Balanis, C. A. (1989), *Advanced engineering electromagnetics*, John Wiley & Sons, Inc., New York.

Balser, M., and C. A. Wagner (1960), Observations of Earth-ionosphere cavity resonances, *Nature*, *188*, 638.

Balser, M., and C. A. Wagner (1962), On frequency variations of the Earth-ionosphere cavity mode, *J. Geophys. Res.*, *67*, 4081.

Bashkuev, Y., and V. Khaptanov (1999), Deep radio impedance sounding of the crust using the electromagnetic field of a VLF radio installation, *Izvestiya. Physics of the Solid Earth*, *37*(2), 157.

Bashkuev, Y. B., and V. B. Khaptanov (2001), Deep radio impedance sounding of the crust using the electromagnetic field of a VLF radio installation, *Izvestiya-Phys. of the Solid Earth*, *37*(2), 157.

Berenger, J. P. (1994), finite-difference computation of VLF-LF propagation in the Earth-ionosphere waveguide, *EUROEM Symp.*, bordeaux, France, May 29 - June 3, 1994.

Berenger, J. P. (2002), FDTD computation of VLF-LF propagation in the Earth-ionosphere waveguide, *Ann. Telecommun.*, *57*, 1059.

Besser, B. P. (2007), Synopsis of the historical development of Schumann resonances, *Radio Sci.*, *42*, RS2S02, doi:10.1029/2006RS003495.

Bilitza, D. (2001), International reference ionosphere 2000, *Radio Sci.*, *36*(2), 261.

Borucki, W. J., Z. Levin, R. C. Whitten, R. G. Keesee, L. A. Capone, O. B. Toon, and J. Dubach (1982), Predicted electrical conductivity between 0 and 80 km in the Venusian atmosphere, *Icarus*, *51*, 301.

Borucki, W. J., Z. Levin, R. C. Whitten, R. G. Keesee, L. A. Capone, A. L. Summers, O. B. Toon, and J. Dubach (1987), Predictions of the electrical conductivity and charging of the aerosols in Titan's atmosphere, *Icarus*, *72*, 604.

Bougher, S. W., S. Engel, D. P. Hinson, and J. M. Forbes (2001), Mars Global Surveyor Radio Science electron density profiles: Neutral atmosphere implications, *Geophys. Res. Lett.*, *28*, 3091.

Bougher, S. W., S. Engel, D. P. Hinson, and J. R. Murphy (2004), MGS radio science electron density profiles: Interannual variability and implications for the Martian neutral atmosphere, *J. Geophys. Res.*, *109*, E03010, doi:10.1029/2003JE002154.

Budden, K. G. (1985), *The Propagation of Radio Waves*, Cambridge Univ. Press, Cambridge.

Cagniard, L. (1953), Basic theory of the magnetotelluric method of geophysical prospecting, *Geophysics*, *18*(3), 605.

Chapman, F. W., and D. L. Jones (1964), Observations of Earth-ionosphere cavity resonances and their interpretation in terms of a two-layer ionosphere model, *J. Res. Natl. Bur. Stand. U.S., Sect. D*, 1177.

Chen, F. F. (1984), *Introduction to plasma physics and controlled fusion*, Plenum Press, New York.

Christian, H. J., R. J. Blakeslee, D. J. Boccippio, W. L. Boeck, D. E. Buechler, K. T. Driscoll, S. J. Goodman, J. M. Hall, W. J. Koshak, D. M. Mach, and M. F. Stewart (2003), Global frequency and distribution of lightning as observed from space by the optical transient detector, *J. Geophys. Res.*, *108*(D1), 4005, doi: 10.1029/2002JD002347.

Connerney, J., M. A. na, P. Wasilewski, N. Ness, H. Réme, C. Mazelle, D. Vignes, R. Lin, D. Mitchell, and P. Cloutier (1999), Magnetic lineations in the ancient crust of Mars, *Science*, *284*(5415), 794.

Connerney, J., M. A. na, P. Wasilewski, G. Kletetschka, N. Ness, H. Réme, R. Lin, and D. Mitchell (2001), The global magnetic field of Mars and implications for crustal evolution, *Geophys. Res. Lett.*, *28*(21), 4015.

Connerney, J., M. A. na, N. Ness, and G. Schubert (2004), Mars crustal magnetism, *Space Science Reviews*, *43*, 1.

Cummer, S. A. (2000), Modeling electromagnetic propagation in the Earth-ionosphere waveguide, *IEEE Trans. on Antennas Propagat.*, *48*(9), 1420.

Cummer, S. A., and M. Farrell (1999), Radio atmospheric propagation on Mars and potential remote sensing applications, *J. Geophys. Res.*, *104*, 14,149.

Desch, S. J., W. J. Borucki, C. T. Russell, and A. Bar-Num (2002), Progress in planetary lightning, *Rep. Prog. Phys.*, *65*, 955.

Duru, F., D. Gurnett, T. Averkamp, D. Kirchner, R. Huff, A. Persoon, J. Plaut, and G. Picardi (2006), Magnetically controlled structures in the ionosphere of Mars, *J. Geophys. Res.*, *111*, A12204, doi:10.1029/2006JA011975.

Eden, H. F., and B. Vonnegut (1973), Electrical breakdown caused by dust motion in low pressure atmospheres: Considerations for Mars, *Nature*, *280*, 962.

Farrell, W. M., M. L. Kaiser, M. D. Desch, J. G. Houser, S. A. Cummer, D. M. Wilt, and G. A. Landis (1999), Detecting electrical activity from Martian dust storms, *J. Geophys. Res.*, *104*, 3795.

Farrell, W. M., P. H. Smith, G. T. Delory, G. B. Hillard, J. Marshall, D. Catling, M. Hecht, D. M. Tratt, N. Renno, M. D. Desch, S. A. Cummer, J. G. Houser, and B. Johnson (2004), Electric and magnetic signatures of dust devils from the 2000-2001 MATADOR desert tests, *J. Geophys. Res.*, *109*(E3), E03004, doi: 10.1029/2003JE002088.

Farrell, W. M., N. Renno, G. T. Delory, S. A. Cummer, and J. R. Marshall (2006), Integration of electrostatic and fluid dynamics within a dust devil, *J. Geophys. Res.*, *111*(E1), E01006, doi:10.1029/2005JE002527.

FitzGerald, G. F. (1893a), *The Scientific Writings of the Late George Francis FitzGerald, edited by J. Larmor*, 576 pp., Hodges, Dublin.

FitzGerald, G. F. (1893b), The period of vibration of disturbances of electrification of the Earth, *Nature*, *48*, 526.

Fulchignoni, M., F. Ferri, F. Angrilli, A. J. Ball, A. Bar-Nun, M. A. Barucci, C. Bettanini, G. Bianchini, W. Borucki, G. Colombatti, M. Coradini, A. Coustenis, S. Debei, P. Falkner, G. Fanti, E. Flamini, V. Gaborit, R. Grard, M. Hamelin, A. M. Harri, B. Hathi, I. Jernej, M. R. Leese, A. Lehto, P. F. L. Stoppato, J. J. Lopez-Moreno, T. Makinen, J. A. M. McDonnell, C. P. McKay, G. Molina-Cuberos, F. M. Neubauer, V. Pirronello, R. Rodrigo, B. Saggin, K. Schwingenschuh, A. Seiff, F. Simoes, H. Svedhem, T. Tokano, M. C. Towner, R. Trautner, P. Withers, and J. C. Zarnecki (2005), In situ measurements of the physical characteristics of Titans environment, *Nature*, *438*, 785.

Füllekrug, M. (1995), Schumann-resonances in magnetic-field components, *J. Atmos. Terr. Phys.*, *57*(5), 479.

Füllekrug, M., and A. Fraser-Smith (1996), Further evidence for a global correlation of the Earth-ionosphere cavity resonances, *Geophys. Res. Lett.*, *23*(20), 2773.

Galejs, J. (1972), *Terrestrial Propagation of Long Electromagnetic Waves*, Elsevier, New York.

Goodman, S. J., D. E. Buechler, K. Knupp, K. T. Driscoll, and E. W. McCaul (2000), The 1997-1998 el nino event and related wintertime lightning variations in the southeastern united states, *Geophys. Res. Lett.*, *27*, 541.

Grard, R., H. Svedhem, V. Brown, P. Falkner, and M. Hamelin (1995), The effects of air pressure and water vapor content on the propagation of positive corona streamers, and their implications to lightning initiation, *J. Atmos. Terr. Phys.*, *57*(2), 575.

Greenberg, E., and C. Price (2007), Diurnal variations of ELF transients and background noise in the Schumann resonance band, *Radio Sci.*, *42*, RS2S08, doi:10.1029/2006RS003477.

Greifinger, C., and P. Greifinger (1978), Approximation method for determining ELF eigenvalues in the Earth-ionosphere cavity, *Radio Sci.*, *12*, 831.

Grimalsky, V., S. Koshevaya, A. Kotsarenko, and R. P. Enriquez (2005), Penetration of the electric and magnetic field components of schumann resonances into the ionosphere, *Annales Geophysicae*, *23*, 2559.

Grimm, R. E. (2001), Low- frequency electromagnetic exploration for groundwater on Mars, *J. Geophys. Res.*, *107*, No. 5006.

Gurnett, D. A., P. Zarka, R. Manning, W. S. Kurth, G. B. Hospodarski, F. T. Averkamp, M. L. Kaiser, and W. M. Farrell (2001), Non-detection at Venus of high-frequency radio signals characteristic of terrestrial lightning, *Nature*, *409*, 313.

Gurnett, D. A., D. L. Kirchner, R. L. Huff, D. D. Morgan, A. M. Persoon, T. F. Averkamp, F. Duru, E. Nielsen, A. Safaeinili, J. J. Plaut, and G. Picardi (2005), Radar soundings of the ionosphere of Mars, *Science*, *310*, 1929.

Hale, L. C. (1984), Middle atmosphere electrical structure, dynamics, and coupling, *Adv. Space Res.*, *4*, 175.

Hamid, E. F., Z.-I. Kawasaki, and R. Mardiana (2001), The 1997-1998 el nino event and related wintertime lightning variations in the southeastern united states, *Geophys. Res. Lett.*, *27*, 147.

Haupt, R. L., and S. E. Haupt (2004), *Practical Genetic Algorithms*, Wiley, Hoboken, New Jersey.

Hayakawa, M., K. Ohta, A. P. Nickolaenko, and Y.Ando (2005), Anomalous effect in schumann resonance phenomena observed in japan, possibly associated with the chi-chi earthquake in taiwan, *Annales Geophysicae*, *23*, 1335.

Hildebrand, F. B. (1956), *Introduction to Numerical Analysis*, McGraw-Hill, New York.

Houser, J., and W. Farrell (2003), ULF and ELF magnetic activity from a terrestrial dust devil, *Geophys. Res. Lett.*, *30*(1), 1027, doi:10.1029/2001GL014144.

Hu, W., and S. A. Cummer (2006), An FDTD model for low and high altitude lightning-generated EM fields, *IEEE Trans. on Antennas Propagat.*, *54*, 1513.

Huang, E., E. Williams, R. Boldi, S. Heckman, W. Lyons, M. Taylor, T. Nelson, and C. Wong (1999), Criteria for sprites and elves baseed on schumann resonance observations, *J. Geophys. Res.*, *104*(D14), 16,943.

Hultqvist, B. (1966), Ionosphere absorption of cosmic radio noise, *Space Science Reviews*, *5*, 771.

Ishaq, M., and D. L. Jones (1977), Method of obtaining radiowave propagation parameters for the earth-ionosphere duct at elf, *Electron. Lett.*, *13*, 254.

Jones, D. L., and D. T. Kemp (1970), Experimental and theoretical observations on the transient excitation of Schumann resonances, *J. Atmos. Terr. Phys.*, *32*, 1095.

König, H. (1959), Atmosperics geringstser frequenzen, *Z. Agnew. Phys.*, *11(7)*, 264.

Krymskii, A., N. Ness, D. Crider, T. Breus, M. A. na, and D. Hinson (2004), Solar wind interaction with the ionosphere/atmosphere and crustal magnetic fields at Mars: Mars Global Surveyor Magnetometer/ Electron Reflectometer, radio science, and accelerometer data, *J. Geophys. Res.*, *109*, A11306, doi:10.1029/2004JA010420.

Ksanfomaliti, L. (1980), Lightning in the cloud layer of Venus, *Cosmic Research*, *17*(5), 617.

Larmor, J. (1893), *Electric vibrations in condensing dielectric systems, in Mathematical and Physical Papers, vol. 1*, 356 pp., Cambridge Univ. Press, Cambridge.

Lillis, R., D. Mitchell, R. Lin, J. Connerney, and M. A. na (2004), Mapping crustal magnetic fields at Mars using electron reflectometry, *Geophys. Res. Lett.*, *31*, L15702, doi:10.1029/2004GL020189.

Melnikov, A., C. Price, G. Sátori, and M. Füllekrug (2004), Influence of solar terminator passages on Schumann resonance parameters, *J. Atmos. Sol. Terr. Phys.*, *66*, 1187.

Mendillo, M., S. Smith, J. Wroten, and H. Rishbeth (2003), Simultaneous ionospheric variability on Earth and Mars, *J. Geophys. Res.*, *108*(A12), 1432, doi:10.1029/2003JA009961.

Mendillo, M., P. Withers, D. Hinson, H. Rishbeth, and B. Reinisch (2006), Effects of solar flares on the ionosphere of Mars, *Science*, *311*, 1135.

Mitchell, D., R. Lin, C. Mazelle, H. Réme, P. Cloutier, J. Connerney, M. A. na, and N. Ness (2001), Probing Mars' crustal magnetic field and ionosphere with the MGS Electron Reflectometer, *J. Geophys. Res.*, *106*(E10), 23,419.

Mitchell, D., R. Lillis, R. Lin, J. Connerney, and M. A. na (2007), A global map of Mars crustal magnetic field based on electron reflectometry, *J. Geophys. Res.*, *112*, E01002, doi:10.1029/2005JE002564.

Molina-Cuberos, G. J., J. Porti, B. P. Besser, J. A. Morente, J. Margineda, H. Lichtenegger, A. Salinas, K. Schwingenschuh, and H. Eichelberger (2004), Schumann resonances and electromagnetic transparence in the atmosphere of Titan, *Adv. Space Res.*, *33*, 2309.

Molina-Cuberos, G. J., J. A. Morente, B. P. Besser, J. Porti, H. Lichtenegger, K. Schwingenschuh, A. Salinas, and J. Margineda (2006), Schumann resonances as a tool to study the lower ionospheric structure of Mars, *Radio Sci.*, *41*, RS1003, doi:10.1029/2004RS003187.

Morente, J. A., G. J. Molina-Cuberos, J. A. Porti, k. Schwingenschuh, and B. P. Besser (2003), A study of the propagation of electromagnetic waves in Titan's atmosphere with the TLM numerical method, *Icarus*, *162*, 374.

Mushtak, V. C., and E. Williams (2002), ELF propagation parameters for uniform models of the Earth-ionosphere waveguide, *J. Atmos. Solar-Terr. Phys.*, *64*(18), 1989.

Navarro, E., A. Soriano, J. Morente, and J. Porti (2007), A finite difference time domain model for the Titan ionosphere Schumann resonances, *Radio Sci.*, *42*, RS2S04, doi:10.1029/2006RS003490.

Nickolaenko, A. P., and M. Hayakawa (2002), *Resonances in the Earth-Ionosphere Cavity*, Kluwer Acad., Norwell.

Nickolaenko, A. P., and L. M. Rabinowicz (1982), On the possibility of existence of global electromagnetic resonances on the planets of solar system, *Space Res.*, *20*, 82.

Nickolaenko, A. P., G. Sátori, B. Zieger, L. M. Rabinowicz, and I. G. Kuduntseva (1998), Parameters of global thunderstorm activity deduced from the long-term schumann resonance records, *J. Atmos. Sol. Terr. Phys.*, *60*, 387.

Nickolaenko, A. P., M. Hayakawa, I. G. Kudintseva, S. V. Myand, and L. M. Rabinowicz (1999), ELF sub-ionospheric pulse in time domain, *Geophys. Res. Lett.*, *26*, 999.

Nickolaenko, A. P., B. P. Besser, and K. Schwingenschuh (2003), Model computations of Schumann resonance on Titan, *Planet. Space Sci.*, *51*, 853.

Nickolaenko, A. P., M. Hayakawa, M. Sekiguchi, Y. Ando, and K. Ohta (2006), Model modifications in Schumann resonance intensity caused by a localized ionosphere disturbance over the earthquake epicenter, *Ann. Geophys.*, *24*, 567.

Ondrášková, A., P. Kostecký, S. Ševčík, and L. Rosenberg (2007), Long-term observations of Schumann resonances at Modra observatory, *Radio Sci.*, *42*, RS2S09, doi:10.1029/2006RS003478.

Otsuyama, T., D. Sakuma, and M. Hayakawa (2003), FDTD analysis of ELF wave propagation and Schumann resonances for a subionospheric waveguide model, *Radio Sci.*, *38*(6), doi:10.1029/2002RS002752.

Pappert, R. A., and F. A. Ferguson (1986), VLF/LF mode conversion model calculations for air to air transmissions in the Earth-ionosphere waveguide, *Radio Sci.*, *21*(551).

Pasko, V. P., U. S. Inan, T. F. Bell, and Y. N. Taranenko (1997), Sprites produced by quasi-electrostatic heating and ionization in the lower ionosphere, *J. Geophys. Res.*, *102*, 4529–4561.

Pasko, V. P., U. S. Inan, T. F. Bell, and S. C. Reising (1998), Mechanism of ELF radiation from sprites, *Geophys. Res. Lett.*, *25*(18), 3493.

Pechony, O., and C. Price (2004), Schumann resonance parameters calculated with a partially uniform knee model on Earth, Venus, Mars, and Titan, *Radio Sci.*, *39*, RS5007, doi:10.1029/2004RS003056.

Pechony, O., and C. Price (2007), Schumann resonances: Interpretation of local diurnal intensity modulations, *Radio Sci.*, *42*, RS2S05, doi:10.1029/2006RS003455.

Picardi, G., J. Plaut, D. Biccari, O. Bombaci, D. Calabrese, M. Cartacci, A. Cicchetti, S. Clifford, P. Edenhofer, W. Farrell, C. Federico, A. Frigeri, D. Gurnett, , T. Hagfors, E. Heggy, A. Herique, R. Huff, A. Ivanov, W. Johnson, R. Jordan, D. Kirchner, W. Kofman, C. Leuschen, E. Nielsen, R. Orosei, E. Pettinelli, R. Phillips, D. Plettemeier, A. Safaeinili, R. Seu, E. Stofan, G. Vannaroni, T. Watters, and E. Zampolini (2005), Radar soundings of the subsurface of Mars, *Science*, *310*, 1925.

Polk, C. (1969), *Relation of ELF noise and Schumann resonances to thunderstorm activity, in Planetary Electrodynamics*, Coronoti and Hughes, New York.

Price, C. (2000), Evidence for a link between global lightning activity and upper tropospheric water vapour, *Nature*, *406*, 290.

Price, C., and A. Melnikov (2004), Diurnal, seasonal and inter-annual variations of the Schumann resonance parameters, *J. Atmos. Solar-Terr. Phys.*, *66*, 1179.

Roldugin, V. C., Y. P. Maltsev, G. A. Petrova, and A. N. Vasiljev (2001), Decrease of the first Schumann resonance frequency during solar proton events, *J. Geophys. Res.*, *106*(A9), 18,555.

Roldugin, V. C., Y. P. Maltsev, A. N. Vasiljev, A. V. Shvets, and A. P. Nikolaenko (2003), Changes of Schumann resonance parameters during the solar proton event of 14 july 2000, *J. Geophys. Res.*, *108*(A3), A31103, doi: 10.1029/2002JA009495.

Roldugin, V. C., Y. P. Maltsev, A. N. Vasiljev, A. Y. Schokotov, and G. G. Belyajev (2004), Schumann resonance frequency increase during solar x-ray bursts, *J. Geophys. Res.*, *109*(A1), A01216, doi:10.1029/2003JA010019.

Russell, C. T. (1993), Planetary lightning, *Annual Rev. Earth Planet. Sci.*, *21*, 43.

Sato, M., and H. Fukunishi (2003), Global sprite occurrence locations and rates derived from triangulation of transient Schumann resonance events, *Geophys. Res. Lett.*, *30*(16), 1859, doi:10.1029/2003GL017291.

Sátori, G. (1996), Monitoring Schumann resonances–II. Daily and seasonal frequency variations, *J. Atmos. Terr. Phys.*, *58*(13), 1483.

Sátori, G., and B. Zieger (1999), El Niño related meridional oscillation of global lightning activity, *Geophys. Res. Lett.*, *29*(10), 1365.

Sátori, G., J. Szendröi, and J. Verö (1996), Monitoring Schumann resonances - I. Methodology, *J. Atmos. Terr. Phys.*, *58*(13), 1475.

Sátori, G., E. R. Williams, and D. J. Boccippio (1999), On the dynamics of the north-south seasonal migration of global lightning, *AGU, Fall Meeting 2003.*, *AE32A-0167*.

Sátori, G., M. Neska, E. Williams, and J. Szendröi (2007), Signatures of the day-night asymmetry of the Earth-ionosphere cavity in high time resolution Schumann resonance records, *Radio Sci.*, *42*, RS2S10, doi:10.1029/2006RS003483.

Schlegel, K., and M. Fullekrug (1999), Schumann resonance parameter changes during high-energy particle precipitation, *J. Geophys. Res.*, *104*(A5), 10,111.

Schumann, W. O. (1952), Uber die strahlungslosen einer leitenden kugel die von einer luftschicht und einer ionospharenhulle umgeben ist, *Z. Naturforsch.*, *7a*, 149.

Schumann, W. O., and H. König (1954), Über die beobachtung von atmospherics bei geringsten frequenzen, *Naturwissenschaften*, *41*, 182.

Sentman, D. D. (1983), Schumann resonance effects of electrical conductivity perturbations in an exponential atmospheric/ionospheric profile, *J. Atmos. Terr. Phys.*, *45*, 55.

Sentman, D. D. (1987), Magnetic elliptical polarization of Schumann resonances, *Radio Sci.*, *22*, 595.

Sentman, D. D. (1990a), Approximate Schumann resonance parameters for a 2-scale-height ionosphere, *J. Atmos. Terr. Phys.*, *52*(1), 35.

Sentman, D. D. (1990b), Electrical conductivity of Jupiters shallow interior and the formation of a resonant planetary-ionospheric cavity, *Icarus*, *88*, 73.

Sentman, D. D. (1995), Schumann Resonance, in *Handbook of Atomospheric Electrodynamics*, vol. 1, edited by H. Volland, p. 276, CRC Press, London.

Sentman, D. D. (1996a), Schumann resonance spectra in a two-scale-height Earth-ionosphere cavity, *J. Geophys. Res.*, *101*(D5), 9479.

Sentman, D. D., and B. J. Fraser (1991), Simultaneous observations of Schumann resonances in California and Australia - evidence for intensity modulation by the local height of the D-region, *J. Geophys. Res.*, *96*(A9), 15,973.

Sentman, D. D., E. M. Wescott, D. L. Osborne, D. L. Hampton, and M. J. Heavner (1995), Preliminary results from the Sprites94 campaign: Red sprites, *Geophys. Res. Lett.*, *22*, 1205–1208.

Shvets, A. V. (2001), A technique for reconstruction of global lightning distance profile from background Schumann resonance signal, *J. Atmos. Solar-Terr. Phys.*, *64*(18), 1061.

Simpson, J. J., and A. Taflove (2002), Two-dimensional FDTD model of antipodal ELF propagation and Schumann resonance of the Earth, *Antennas and Wireless Propagation Lett.*, *1*(2), 53.

Simpson, J. J., and A. Taflove (2004), Three-dimensional FDTD modeling of impulsive ELF propagation about the earth-sphere, *IEEE Trans. on Antennas Propagat.*, *52*(2), 443.

Simpson, J. J., and A. Taflove (2006a), A novel ELF radar for major oil deposits, *IEEE Geoscience and Remote Sensing Lett..*, *3*(1), 36.

Simpson, J. J., and A. Taflove (2006b), FDTD modeling of a novel ELF radar for major oil deposits using a three-dimensional geodesic grid of the Earth-ionosphere waveguide, *IEEE Trans. on Antennas Propagat.*, *54*(6), 1734.

Simpson, J. J., and A. Taflove (2007), A review of progress in FDTD maxwell's equations modeling of impulsive subionospheric propagation below 300 kHz, *IEEE Trans. on Antennas Propagat.*, *55*(6), 1582.

Sukhorukov, A. I. (1991), On the Schumann resonances on Mars, *Planet. Space Sci.*, *39*(12), 1673.

Taflove, A., and S. C. Hagness (2000), *Computational Electrodynamics: The Finite-Difference Time-Domain Method*, Artech House, Norwood Mass.

Thevenot, M., J. P. Berenger, T. Monediere, and F. Jecko (1999), A FDTD scheme for the computation of VLF-LF propagation in the anisotropic Earth-ionosphere waveguide, *Ann. Telecommun.*, *54*(5), 297.

Thomson, J. J. (1893), *Notes on Recent Researches in Electricity and Magnetism, Intended as a Sequel to Professor Clerk-Maxwells Treatise on Electricity and Magnetism*, 578 pp., Clarendon, Oxford.

Tokano, T., G. J. Molina-Cuberos, H. Lammer, and W. Stumptner (2005), Modeling of thunderclouds and lightning generation on Titan, *Planet. Spac. Sci.*, *49*(6), 539.

Uman, M. A. (1987), *The lightning discharge*, Academic Press, Orlando.

Velikhov, E., A. Zhamaletdinov, A. Shevtsov, A. Tokarev, Y. Kononov, L. Pesin, G. Kadyshevich, M. Pertel, and A. Veshchev (1998), Deep electromagnetic studies with the use of powerful ELF radio installations, *Izvestiya. Physics of the Solid Earth*, *34*(8), 615.

Wait, J. (1972), *Electromagnetic waves in stratified media*, Pergamon Press, Oxford.

Walt, M. (1994), *Introduction to Geomagnetically Trapped Radiation*, Cambridge University Press, Cambridge.

Williams, E. R. (1992), The Schumann resonance - a global tropical thermometer, *Science*, *256*(5060), 1184.

Williams, E. R., and G. Sátori (2004), Lightning, thermodynamic and hydrological comparison of the two tropical continental chimneys, *J. Atmos. Sol. Terr. Phys.*, *66*, 1213.

Withers, P., and M. Mendillo (2005), Response of peak electron densities in the Martian ionosphere to day-to-day changes in solar flux due to solar rotation, *Planet. Spac. Sci.*, *53*, 1401.

Withers, P., M. Mendillo, H. Rishbeth, D. P. Hinson, and J. Arkani-Hamed (2005), Ionospheric characteristics above Martian crustal magnetic anomalies, *Geophys. Res. Lett.*, *32*(16), L16204, doi:10.1029/2005GL023483,2005.

Yang, H., and V. P. Pasko (2005), Three-dimensional finite-difference time-domain modeling of the Earth-ionosphere cavity resonances, *Geophys. Res. Lett.*, *32*, L03114, doi:10.1029/2004GL021343.

Yang, H., and V. P. Pasko (2006), Three-dimensional finite-difference time-domain modeling of the diurnal and seasonal variations in Schumann resonance parameters, *Radio Science*, *41*, RS2S03, doi:10.1029/2005RS003431.

Yang, H., and V. P. Pasko (2007), Power variations of Schumann resonances related to El Niño and La Niña phenomena, *Geophys. Res. Lett.*, *34*(11), L11102, doi: 10.1029/2007GL030092.

Yang, H., V. P. Pasko, and Y. Yair (2006), Three-dimensional finite-difference time-domain modeling of Schumann resonance parameters on Titan, Venus, and Mars, *Radio Science*, *41*, RS2S14, doi:10.1029/2005RS003402.

Yee, K. S. (1966), Numerical solution of initial boundary value problem involving Maxwell's equations in isotropic media, *IEEE Trans. on Antennas Propagat.*, *14*(3), 802.

Zhai, Y., S. Cummer, and W. Farrell (2006), Quasi-electrostatic field analysis and simulation of Martian and terrestrial dust devils, *J. Geophys. Res.*, *111*, E06016, doi:10.1029/2005JE002618.

Zhang, M. H. G., J. G. Luhmann, A. J. Kliore, and J. Kim (1990), A post-Pioneer Venus reassessment of the Martian dayside ionosphere as observed by radio occultation methods, *J. Geophys. Res.*, *95*, 14,829.

Zou, H., J.-S. Wang, and E. Nielsen (2005), Effect of the seasonal variations in the lower atmosphere on the altitude of the ionospheric main peak at Mars, *J. Geophys. Res.*, *101*, A09311, doi:10.1029/2004JA010963.

Vita

Heng Yang

July 23, 1975
Born in Nanjing, China

1994-1998, Southeast University, Nanjing, Jiangsu, China
B.S., Radio Engineering

1998-2001, Southeast University, Nanjing, Jiangsu, China
M.S., Radio Engineering
Thesis title: *FDTD modeling of coupling coefficients of irises/slots in combline filters*
Advisor: Aosheng Rong

2001-2002, Huawei Technology Inc., Shanghai, China
RF Test engineer

2002-2007, The Pennsylvania State University, University Park, Pennsylvania, USA
Ph.D., Electrical Engineering
Thesis Title: *Three Dimensional Finite Difference Time Domain Modeling of Schumann Resonances in Earth-Ionosphere Cavity and Other Celestial Bodies of the Solar System*
Advisor: Victor P. Pasko